



**Australian Government**

**Geoscience Australia**

Geoscience Australia Marine Survey 266, Post-cruise Report

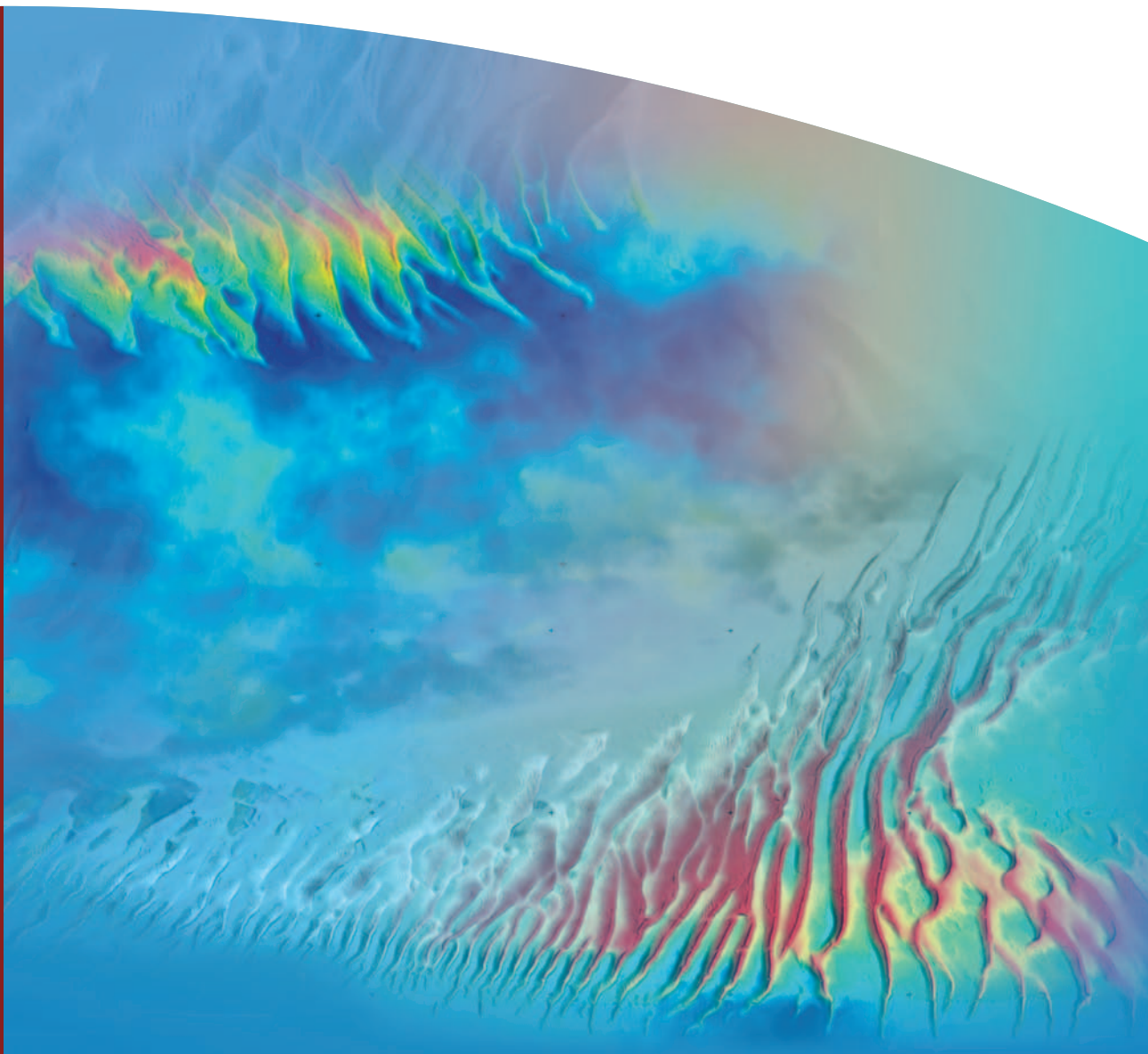
# **Biophysical Processes in the Torres Strait Marine Ecosystem**

*RV James Kirby, March–April 2004*

*Andrew Heap, Mark Hemer, James Daniell, Emma Mathews, Peter Harris,  
Simon Kerville & Lyndon O'Grady*

**Record**

**2005/11**



**Geoscience Australia Marine Survey 266**

**Post-cruise Report**

**Biophysical Processes in the Torres Strait  
Marine Ecosystem**

(Torres Strait CRC Task T2.2)

***RV James Kirby***

**March – April 2004**

Andrew Heap<sup>1</sup>, Mark Hemer<sup>1</sup>, James Daniell<sup>1</sup>, Emma Mathews<sup>1</sup>,  
Peter Harris<sup>1</sup>, Simon Kerville<sup>2</sup> & Lyndon O'Grady

<sup>1</sup> *Geoscience Australia, GPO Box 378, Canberra, ACT 2601*

<sup>2</sup> *Department of Primary Industries & Fisheries, GPO Box 46, Brisbane, QLD 4001*



**Australian Government**

**Geoscience Australia**

## Department of Industry, Tourism & Resources

Minister for Industry, Tourism & Resources: Senator The Hon. Ian Macfarlane, MP

Parliamentary Secretary: The Hon. Warren Entsch, MP

Secretary: Mark Paterson

## Geoscience Australia

Chief Executive Officer: Dr Neil Williams

© Commonwealth of Australia 2005

This work is copyright. Apart from any fair dealings for the purposes of study, research, criticism or review, as permitted under the *Copyright Act 1968*, no part may be reproduced by any process without written permission. Copyright is the responsibility of the Chief Executive Officer, Geoscience Australia. Requests and enquiries should be directed to the **Chief Executive Officer, Geoscience Australia, GPO Box 378, Canberra City, ACT 2601, Australia.**

ISSN: 1448 2177

ISBN: 1 920871 45 4

GeoCat No. 61843

Bibliographic reference: Heap, A.D., Hemer, M., Daniell, J., Mathews, E., Harris, P.T., Kerville, S. & O'Grady, L. (2005). <i>Biophysical Processes in the Torres Strait Marine Ecosystem – post cruise report</i> . Geoscience Australia, Record 2005/11, 112pp.
---

Correspondence for feedback:

### **Sales Centre**

Geoscience Australia

GPO Box 378

Canberra

ACT 2601

Sales@ga.gov.au

Geoscience Australia has tried to make the information in this product as accurate as possible. However, it does not guarantee that the information is totally accurate or complete. **Therefore, you should not rely solely on this information when making a commercial decision.**

# Contents

	Page
<b>List of Figures .....</b>	<b>v</b>
<b>List of Tables .....</b>	<b>vii</b>
<b>Executive Summary .....</b>	<b>viii</b>
<b>1. Introduction .....</b>	<b>1</b>
1.1. Background .....	1
1.1.1. <i>Regional Setting – Torres Strait</i> .....	1
1.1.2. <i>Study Area – Turnagain Island</i> .....	3
1.1.3. <i>Survey Objectives</i> .....	3
1.2. Survey Participants .....	5
1.2.1. <i>Scientific Personnel</i> .....	5
1.2.2. <i>Ship’s Crew</i> .....	6
<b>2. Geophysics .....</b>	<b>7</b>
2.1. Data Acquisition .....	7
2.1.1. <i>Swath (Multi-beam) Sonar</i> .....	7
2.1.2. <i>Shallow Seismic Reflection</i> .....	8
2.2. Data Processing and Analysis .....	10
2.2.1. <i>Swath (Multi-beam) Sonar Data</i> .....	10
2.2.2. <i>Shallow Seismic Reflection Data</i> .....	11
2.3. Results .....	12
2.3.1. <i>Swath (Multi-beam) Sonar</i> .....	12
2.3.2. <i>Shallow Seismic Reflection</i> .....	14
2.4. Sediment and Sandwave Movement .....	19
2.4.1. <i>Sandwave Migration</i> .....	10
<b>3. Oceanography .....</b>	<b>24</b>
3.1. Data Acquisition .....	24
3.1.1. <i>Geoscience Australia Oceanographic Mooring (BRUCE)</i> .....	24
3.1.2. <i>CSIRO Oceanographic Moorings</i> .....	26
3.2. Data Processing and Analysis .....	27
3.2.1. <i>Geoscience Australia Oceanographic Mooring (BRUCE)</i> .....	27
3.2.2. <i>CSIRO Oceanographic Moorings</i> .....	27
3.3. Results .....	29
3.3.1. <i>SBE-19 Multi-sensor Data</i> .....	20
3.3.2. <i>Tidal Statistics</i> .....	25
3.3.3. <i>Bedload Transport Estimates</i> .....	58
3.3.4. <i>Estimates of Sandwave Migration</i> .....	61



	Page
<b>4. Sedimentology .....</b>	<b>63</b>
4.1. Sample Acquisition .....	63
4.1.1. <i>Water Samples</i> .....	64
4.1.2. <i>Digital Video Footage</i> .....	64
4.1.3. <i>Surface Sediment Sampling</i> .....	67
4.1.4. <i>Subsurface Sediment Sampling</i> .....	67
4.2. Sample Processing and Analysis.....	68
4.2.1. <i>Water Samples</i> .....	68
4.2.2. <i>Digital Video Footage</i> .....	68
4.2.3. <i>Surface Sediments</i> .....	68
4.2.4. <i>Subsurface Sediments</i> .....	69
4.3. Results.....	70
4.3.1. <i>Water Samples</i> .....	70
4.3.2. <i>Digital Video Footage</i> .....	73
4.3.3. <i>Surface Sediments</i> .....	75
4.3.4. <i>Seagrass Types and Distributions</i> .....	83
4.3.5. <i>Subsurface Sediments</i> .....	85
<b>5. Discussion and Summary .....</b>	<b>90</b>
5.1. Sediment Transport.....	90
5.2. Seabed Environments and Habitats.....	91
5.3. Implications for Seagrasses and Fisheries Management .....	92
<b>6. Acknowledgements .....</b>	<b>94</b>
<b>7. References.....</b>	<b>95</b>
<b>8. Appendices.....</b>	<b>98</b>
8.1. Appendix A – Survey Leaders Log.....	98
8.2. Appendix B – Shallow Seismic Profiles.....	101
8.3. Appendix C – Photos of the BRUCE Mooring .....	101
8.4. Appendix D – Photos of the CSIRO Moorings.....	101
8.5. Appendix E – Problems with the BRUCE Mooring .....	101
8.6. Appendix F – Digital Video Footage .....	101
8.7. Appendix G – Textural Characteristics of Surface Sediments .....	101
8.8. Appendix H – Core Logs.....	104
8.9. Appendix I – Textural Characteristics of Subsurface Sediments.....	110

# List of Figures

	Page
<b>1. Introduction .....</b>	<b>1</b>
Figure 1.1. Regional map of Torres Strait.....	2
Figure 1.2. Satellite image of sandwaves in Torres Strait. ....	4
Figure 1.3. Map showing regions of significant seagrass dieback.....	4
Figure 1.4. Photograph of the RV <i>James Kirby</i> .....	5
<b>2. Geophysics.....</b>	<b>7</b>
Figure 2.1. Photographs of: a) sandwaves, and b) sandwaves and seagrass/algal beds next to Turnagain Island.....	7
Figure 2.2. Photograph of the Reson 8101 swath sonar transducer/receiver. ....	8
Figure 2.3. Maps showing survey track lines (regional, Area A, Area B). ....	9
Figure 2.4. Photograph of the Chirp tow-fish.....	9
Figure 2.5. Maps showing bathymetry of Area A for a) survey 1 & b) survey 2.....	13
Figure 2.6. Maps showing bathymetry of Area B for a) survey 1 & b) survey 2. ....	15
Figure 2.7. High-resolution bathymetry map of secondary dunes in Area B. ....	16
Figure 2.8. High-resolution bathymetry map of ladder ripples in Area B. ....	16
Figure 2.9. Chirp shallow seismic profiles of a) seabed and b) sub-bottom reflectors and c-d) sand ridges over acoustic basement in Area A. ....	17
Figure 2.10. Chirp shallow seismic profiles of a) seabed and b) sub-bottom reflectors in Area B. ....	18
Figure 2.11. Maps showing echo-types for Area A and Area B.....	19
Figure 2.12. Maps showing position of crests for: a) survey 1, b) survey 2 and c) combined .....	21
Figure 2.13. Maps showing the total distance of sandwave crest movement in: a) Area A and b) Area B.....	22
Figure 2.14. Maps showing the total volume of sediment moved in: a) Area A and b) Area B.....	23
<b>3. Oceanography .....</b>	<b>24</b>
Figure 3.1. Map showing location of oceanographic moorings.....	24
Figure 3.2. Time series plots of SBE-19 data at CSIRO-1.....	32
Figure 3.3. Time series plots of 30-hr low pass data from SBE-19 at CSIRO-1. ....	33
Figure 3.4. Time series plots of SBE-19 data at CSIRO-2.....	34
Figure 3.5. Time series plots of 30-hr low pass data from SBE-19 at CSIRO-2. ....	35
Figure 3.6. Time series plots of SBE-19 data at CSIRO-3.....	36
Figure 3.7. Time series plots of 30-hr low pass data from SBE-19 at CSIRO-3. ....	37
Figure 3.8. Classical harmonic analysis of pressure data at CSIRO-1.....	39
Figure 3.9. Classical harmonic analysis of pressure data at CSIRO-2. ....	40
Figure 3.10. Classical harmonic analysis of pressure data at CSIRO-3.....	42
Figure 3.11. Progressive tidal vector plot from ADCP at CSIRO-2. ....	45
Figure 3.12. Progressive tidal vector plot from ADCP at CSIRO-3. ....	45
Figure 3.13. Time series of near-bed tidal current speeds at CSIRO-2.....	47
Figure 3.14. Time series of surface tidal current speeds at CSIRO-2.....	48

	Page
Figure 3.15. ADCP 30-hr low-pass near-bed tidal current speeds at CSIRO-2. ....	49
Figure 3.16. ADCP 30-hr low-pass surface tidal current speeds at CSIRO-2. ....	50
Figure 3.17. Time series of near-bed tidal current speeds at CSIRO-3. ....	51
Figure 3.18. Time series of surface tidal current speeds at CSIRO-3. ....	52
Figure 3.19. ADCP 30-hr low-pass near-bed tidal current speeds at CSIRO-3. ....	53
Figure 3.20. ADCP 30-hr low-pass surface tidal current speeds at CSIRO-3. ....	54
Figure 3.21. Scatter plots of tidal currents with principal axes from CSIRO-2. ....	55
Figure 3.22. Scatter plots of tidal currents with principal axes from CSIRO-3. ....	55
Figure 3.23. Tidal ellipses for M2, S2, K1 and O1 constituents from CSIRO-2.....	57
Figure 3.24. Tidal ellipses for M2, S2, K1 and O1 constituents from CSIRO-3.....	57
Figure 3.25. Vector stick plots of bedload transport at CSIRO-2.....	60
Figure 3.26. Vector stick plots of bedload transport at CSIRO-3.....	61
 <b>4. Sedimentology.....</b>	 <b>63</b>
Figure 4.1. Map showing location of sampling stations for a) regional, b) Area A and c) Area B.....	63
Figure 4.2. Photographs of a) Niskin bottle, b) Van-veen grab, c) vibrocorer and d) water filtering system. ....	66
Figure 4.3. Photograph of underwater digital video camera and housing.....	67
Figure 4.4. Graphs of SSC's for stations: a) 58, b) 62, c) 80, and d) 81. ....	72
Figure 4.5. Map showing location of camera stations. ....	74
Figure 4.6. Map showing location of grab samples.....	76
Figure 4.7. Maps showing: a) %Gravel, b) %Sand and c) %Mud for Area A.....	78
Figure 4.8. Maps showing: a) %CaCO <sub>3</sub> (bulk), b) %CaCO <sub>3</sub> (sand), and c) %CaCO <sub>3</sub> (sand) for Area A. ....	79
Figure 4.9. Maps showing: a) %Gravel, b) %Sand and c) %Mud for Area B.....	81
Figure 4.10. Maps showing: a) %CaCO <sub>3</sub> (bulk) and b) %CaCO <sub>3</sub> (sand) for Area B....	82
Figure 4.11. Map showing location of seagrass. ....	83
Figure 4.12. Map showing location of vibrocores. ....	86
 <b>8. Appendices.....</b>	 <b>98</b>
Figure 8.1. Core log for VC01. ....	105
Figure 8.2. Core log for VC02 .....	106
Figure 8.3. Core log for VC03 .....	107
Figure 8.4. Core log for VC04 .....	108
Figure 8.5. Core log for VC05 .....	109

# List of Tables

	Page
<b>2. Geophysics .....</b>	<b>7</b>
Table 2.1. Details of swath (multi-beam) sonar surveys.....	12
Table 2.2. Descriptions of echo-types observed in Area A and B.....	18
<b>3. Oceanography .....</b>	<b>24</b>
Table 3.1. Basic statistics for SBE-19 Multi-sensors. ....	31
Table 3.2. Classical harmonic tidal analysis for CSIRO-1.....	38
Table 3.3. Regression statistics for pressure records on CSIRO-2. ....	38
Table 3.4. Classical harmonic tidal analysis for CSIRO-2.....	38
Table 3.5. Regression statistics for pressure records on CSIRO-3. ....	41
Table 3.6. Classical harmonic tidal analysis for CSIRO-3.....	41
Table 3.7. Significant third and fourth tidal constituents from CSIRO Moorings. ....	43
Table 3.8. Basic statistics from ADCP on CSIRO-2 and CSIRO-3.....	44
Table 3.9. Principal axes for tidal currents recorded by CSIRO-2 and CSIRO-3.....	46
Table 3.10. Tidal ellipse parameters for CSIRO-2 and CSIRO-3.....	56
Table 3.11. Bedload transport estimates in the vicinity of CSIRO-2. ....	59
Table 3.12. Bedload transport estimates in the vicinity of CSIRO-3. ....	61
Table 3.13. Sandwave migration rates in the vicinity of CSIRO-2 and CSIRO-3. ....	62
<b>4. Sedimentology .....</b>	<b>63</b>
Table 4.1. Station operations.....	65
Table 4.2. Distribution and types of seagrasses in Areas A and B. ....	84
Table 4.3. Details of vibrocores collected during the survey. ....	86
<b>8. Appendices .....</b>	<b>98</b>
Table 8.1. Textural characteristics of surface sediments in Area A.....	102
Table 8.2. Textural characteristics of surface sediments in Area B. ....	103
Table 8.3. Textural characteristics of sediment in the vibrocores.....	110

## Executive Summary

This report contains the preliminary results of Geoscience Australia survey 266 to central Torres Strait. The present survey is the first of two by Geoscience Australia to be carried out in 2004 and is part of a larger field-based program managed by the Torres Strait CRC aimed at identifying and quantifying the principal physical and biological processes operating in Torres Strait. The impetus for the program is the threat of widespread seagrass dieback and its effects on local dugong and turtle populations and the implications for indigenous islander communities. The principal aim of the survey was to investigate the seabed geomorphology and sedimentary processes in the vicinity of Turnagain Island and to infer the possible effects (if any) on the distribution, abundance and survival of seagrasses. The Turnagain Island region was chosen because it is a known site of recent widespread seagrass dieback.

The survey consisted of a detailed geophysical survey using swath (multi-beam) sonar and shallow seismic equipment that was supplemented with a detailed sampling program consisting of 301 near-bed water samples, 54 seabed grabs, 5 vibrocores and 69 camera stations. Four oceanographic moorings were also deployed for the duration of the survey to measure the local tide, wave and wind-driven currents. A regional survey was initially undertaken, followed by a detailed study of two areas: Area A – located approximately 2.5 km SW of Turnagain Island which contained sand ridges and seagrass beds, and Area B – located approximately 2.0 km SE of Turnagain Island which contained sandwaves and no seagrass beds.

The geophysical surveys indicate that the seabed in the study area is irregular, consisting of undulating hard-grounds, reefal platforms, and extensive mobile bedforms. The bedforms consist of sandwaves that form an elongate v-shaped sand body that conforms with the Kenyon et al. (1981) definition of a type “D” sand ribbon. The sandwaves, which are most extensive in Area B, are up to 3.5 m in high and spaced 20-200 m apart. The largest of these attain more than half of the water depth in height. Repeat surveys of the sandwaves indicate that the crests moved up to 19.3 m to the west during the survey. This westward movement coincided with a change in wind direction from northerly monsoon to southeast trade winds. We infer from this that the sandwaves are extremely mobile and their morphology and orientation are probably related to residual water movements forced by seasonal winds. In a new application of the swath (multi-beam) data, the total volume of sediment transported during the survey was estimated from changes in the high-resolution seabed bathymetry collected during the repeat surveys. Total volumes transported during the 20 day survey attained  $>3 \text{ m}^3$  on the crests of the sandwaves located in Area B.

The sampling program revealed that the seabed sediments are comprised of poorly-sorted calcareous medium sands and gravels that form a relatively thin veneer ( $<4 \text{ m}$ ) over a harder, indurated surface of probable fluvial, coastal and marine deposits laid down when Torres Strait was emergent during the last interglacial. Only minor quantities of terrigenous fragments were recovered, probably reworked from the underlying surface. Samples recovered from the reefal platforms contained coral and other limestone fragments, indicating that they form weakly-cemented reefs. Shallow vibrocores through the sandwaves and sand ridges indicate no significant changes in sediment composition and revealed no obvious internal structures. The camera stations confirmed that the boundaries between the sedimentary environments were very distinct and occurred over only a few meters.

Tides in both Area A and Area B have a strong mixed, semi-diurnal signature, with ebb and flood near-bed current speeds of up to  $75 \text{ cm s}^{-1}$  eastward and westward, respectively. The current meter records show a relatively strong wind-driven residual flow to the west-south-west, with a net displacement during the deployment of 210 km in Area A and 120 km in Area B. The residual flow corresponds in direction to the recorded orientation of the sandwaves in Area B. Non-linear interaction of the semi-diurnal tides in the shallow regions leads to an intensification of the shallow water tidal constituents. Water samples indicate that near-bed suspended sediment concentrations attain  $30 \text{ mg l}^{-1}$  during neap tides, but are generally low. Bed sediment is mostly suspended by waves and moves along the seabed in distinct pulses. During neap tides, peak concentrations occur approximately 12 hours apart in response to tidal motions.

The preliminary findings detailed above imply that the sedimentary processes in the vicinity of Turnagain Island are very dynamic which is reflected by the diverse geomorphology, habitats and biota. Seagrasses in the region are thus subject to frequent and significant changes in environmental conditions, with implications for limited dispersal and survival. In the study areas, seagrasses are not abundant with few contiguous meadows. Seagrass beds are mostly interspersed with algal beds. The most abundant types of seagrass found in the study areas are those that can colonise the seabed easily and are generally less susceptible to environmental perturbations. It is possible that widespread movement of the sandwaves, possibly associated with perturbations in the regional wind patterns (e.g., a weak monsoon), could adversely effect extensive regions of seagrass and be partly responsible for the dieback events observed. A follow-up survey will be undertaken in October 2004 to examine some of these hypotheses.



# 1. Introduction

This record contains the results of Geoscience Australia marine survey 266. The survey, the first of two in 2004, was completed between 28 March to 18 April 2004 in north-central Torres Strait, near Turnagain Island using James Cook University's research vessel *James Kirby*. The survey included Geoscience Australia and Queensland Department of Primary Industry and Fisheries scientists.

Geoscience Australia is a partner in the Torres Strait CRC which is a 3-year supplementary program of the Reef CRC based in Townsville. The present survey is part of a larger field-based program managed by the Reef CRC aimed at identifying and quantifying the principal physical and biological processes operating in Torres Strait. Geoscience Australia's research focus is to investigate the key physical processes associated with the distribution, dieback and recovery of seagrass. This includes documentation of seabed sediments and associated habitats, sediment transport pathways and fluxes, seabed stability and late Quaternary history in the region.

A follow-up survey will occur at the end of the trade wind season in October 2004. Data collected from both surveys will assist in characterising seabed ecosystems in Torres Strait, provide crucial information on the nature of the seabed for developing models of physical and biological processes, and also provide inputs into management strategies.

## 1.1. BACKGROUND

As recently as 1991, 1999 and 2001, widespread seagrass dieback events have been recorded by local fishers and CSIRO scientists in Torres Strait (e.g., Long et al., 1997). While the timing, location and extent of the dieback events are relatively well established, the reasons for the dieback events are not entirely understood.

The Torres Strait Island community is concerned that the dieback events are triggering a reduction in the populations of dugong and sea turtles, which they have traditionally hunted for food. Local communities are concerned that increased sediment load from the Fly River (Papua New Guinea) produced by the Ok Tedi gold mine has significantly raised turbidity levels in Torres Strait to a point where the reduction in light to the seabed has resulted in seagrass dieback. However, hydrodynamic modelling of the ocean currents indicates that very little water and sediment probably enters Torres Strait from the Gulf of Papua (Hemer et al., 2004). Several other hypotheses may be possible, including: 1) widespread movement of sandwaves smothering the seagrass beds; and 2) changes in temperature and salinity from changes to wave and wind-driven current conditions. Testing these (and other) hypotheses requires a deeper understanding of the sedimentary and oceanographic processes operating in Torres Strait.

The present survey has been designed to ascertain the role of sediment transport, sandwave movement and associated turbidity and their potential effects (if any) on the survival, dieback and recovery of seagrass in Torres Strait.

### 1.1.1. Regional Setting – Torres Strait

Torres Strait is located at the northern end of the Cape York Peninsula and separates Australia from Papua New Guinea (Fig. 1.1). It is a major shipping seaway connecting the northern ports of Australia with Southeast Asia and the Pacific. Due to its significant



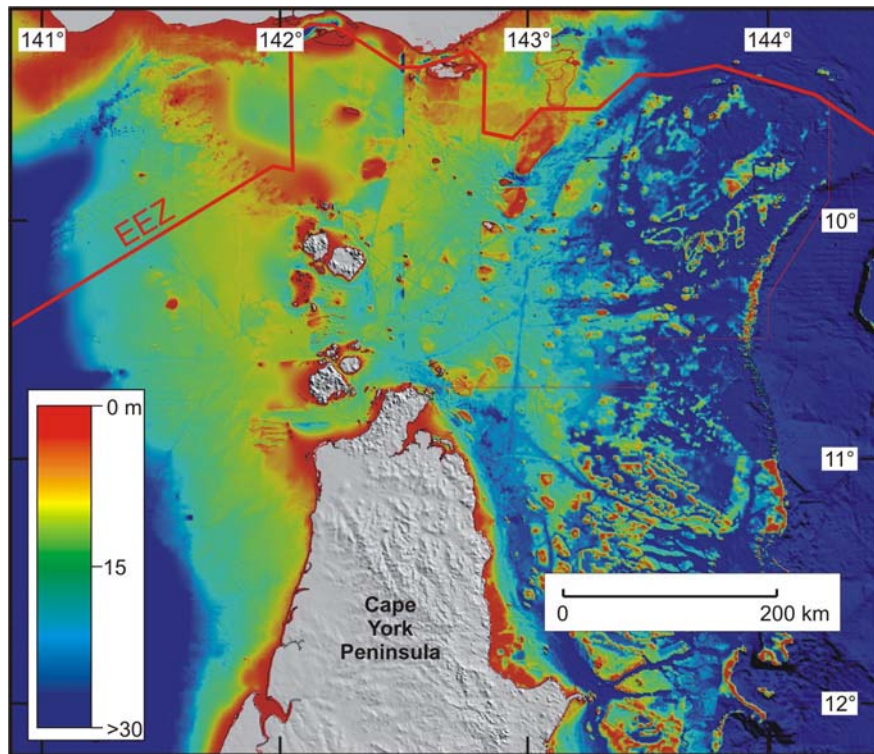


Figure 1.1. Regional map of Torres Strait. Torres Strait is a shallow (<15 m) seaway separating Australia in the south from Papua New Guinea in the north. The strait is a geomorphologically complex region containing a discontinuous chain of largely granitic islands and numerous sandwaves in the west, isolated volcanic islands and well-developed coral reefs in the east, and numerous well-developed coral reefs and high-islands in the centre. During the Last Glacial (~18,000 years ago) Torres Strait formed a land bridge that connected Australia to Papua New Guinea.

biological diversity it contains valuable fisheries resources (Williams and Staples, 1990) and sensitive seagrass habitats that also support dugong and green turtle populations. Torres Strait is the oceanographic boundary between the Gulf of Carpentaria and Coral Sea. It is a biological barrier corresponding to the northern limit of the Great Barrier Reef (GBR) and a political boundary between Australia, Papua New Guinea and Indonesia. It is also a principal geological mixing zone, sandwiched between the largest modern tropical carbonate province on Earth—the GBR—and a margin supplying vast amounts of terrigenous sediment to the ocean (Papua New Guinea).

Water depths in Torres Strait are 15-25 m and the seabed forms a low-relief plain that was a land bridge connecting Australia with Papua New Guinea throughout most of the Quaternary (Harris, 1988). A discontinuous chain of largely granitic islands occurs in the western regions, isolated volcanic islands occur in the eastern regions, and scattered high islands are abundant in the central regions (Fig. 1.1; Woodroffe et al., 2000). Abundant coral reefs occur throughout Torres Strait, with approximately 600 individual fringing and patch reefs; almost all islands contain well-developed reef flats, some up to several kilometres wide (Woodroffe et al., 2000; Heap et al., 2004). The reefs have morphologies similar to those of the northern GBR province but are distinctly elongated in an east-west direction due to local tidal current forcing. Large banks, also elongated east-west, comprised of the coralline algae *Halimeda* are abundant in the east.

Surface sediments in Torres Strait are a mixture of locally-derived carbonate and terrigenous material. Sands and gravels dominate the carbonate fraction and reflect the high

energy conditions. The carbonate fraction is made up of the skeletal remains of benthic foraminifers, mollusc, ostracods, *Halimeda*, and corals. The terrigenous fraction is made up of relict quartz sands and silts and clays.

The surface sediments are regularly mobilised by strong tide and wave currents. Tides are mixed with one high-high water (HHW) and low-high water (LHW) per day (Harris, 1989). The numerous reefs and islands form an impermeable barrier to tides and greatly attenuate the tidal ranges. Tidal currents are directed east-west and locally attain  $2.5 \text{ m s}^{-1}$  due to the constricted coastal geometry. Superimposed on this energetic tidal regime are wave-induced currents, wind-driven circulation, ocean currents and storm surges. Wave heights attain 3.5 m during the trade wind season and less than 1.5 m during the NW monsoon (McMillan, 1982; Hemer et al., 2004). Shallow water depths in Torres Strait mean that tropical cyclones and their associated storm surges generate very strong near-bed currents capable of eroding and transporting vast amounts of bed sediment to a depth of several tens of centimetres (cf., Gagan et al., 1988; Larcombe and Carter, 2004).

### 1.1.2. Study Area – Turnagain Island

Widespread areas of the seabed in Torres Strait are covered with mobile sandy bedforms (Fig. 1.2). These sandwaves are numerous, principally located in the west between the islands, and exhibit a variety of forms that are related to the availability of bed sediment and tidal current velocities. In the vicinity of Turnagain Island, the sandwaves are also located in regions of significant seagrass dieback (Fig. 1.3). The sandwaves in the vicinity of Turnagain Island attain 4-6 m in height and wave lengths of several hundred metres (Harris, 1988). The larger bedforms can reach heights that are more than half the water depth. Sand is actively moving through Torres Strait so that smaller, rapidly migrating bedforms are superimposed on the surfaces of the larger sandwaves. The sandwaves may display opposite migration directions in winter and summer under the forcing of the seasonal wind directions (Harris, 1991). Interspersed between the sandwaves are hard-grounds, represented by the underlying land surface, and seagrass and algal reef habitats. The transition between these habitats occurs over only a few metres.

### 1.1.3. Survey Objectives

The principal survey objective was to document the seabed habitats, Late Quaternary history, and hydrodynamic and sedimentary processes associated with sandwave and seagrass habitats in the vicinity of Turnagain Island. This principal objective was designed to gain a better understanding of the possible causes for widespread seagrass dieback observed in Torres Strait, focussing on whether the dieback events are in some way related to either movement of sandwaves and/or increased turbidity. The Turnagain Island region was selected because it contains extensive areas of sandwaves and seagrass/algal habitats in close proximity to each other and was one of the worst affected sites during the 1999 and 2001 seagrass dieback events.

Several specific tasks were implemented to fulfil the overall survey objective, as follows:

1. Construction of a high-resolution bathymetric map of two contrasting sites; one containing sandwaves and no seagrass, and one containing sandwaves and seagrasses;

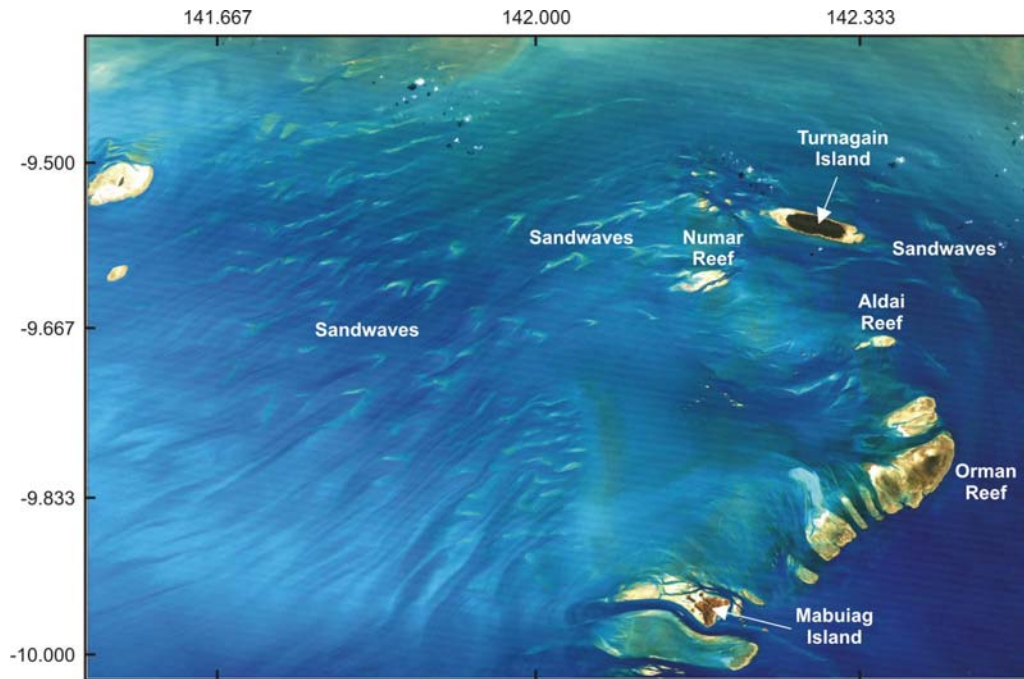


Figure 1.2. Satellite image of sandwaves in central and western Torres Strait. The extensive sandwave fields are formed by the strong tidal currents in the strait. Sandwaves in the western regions are barchan dunes and occur as distinct bedforms. Sandwaves in central regions next to islands are connected to islands and reefs and form ribbons migrating over the seabed.

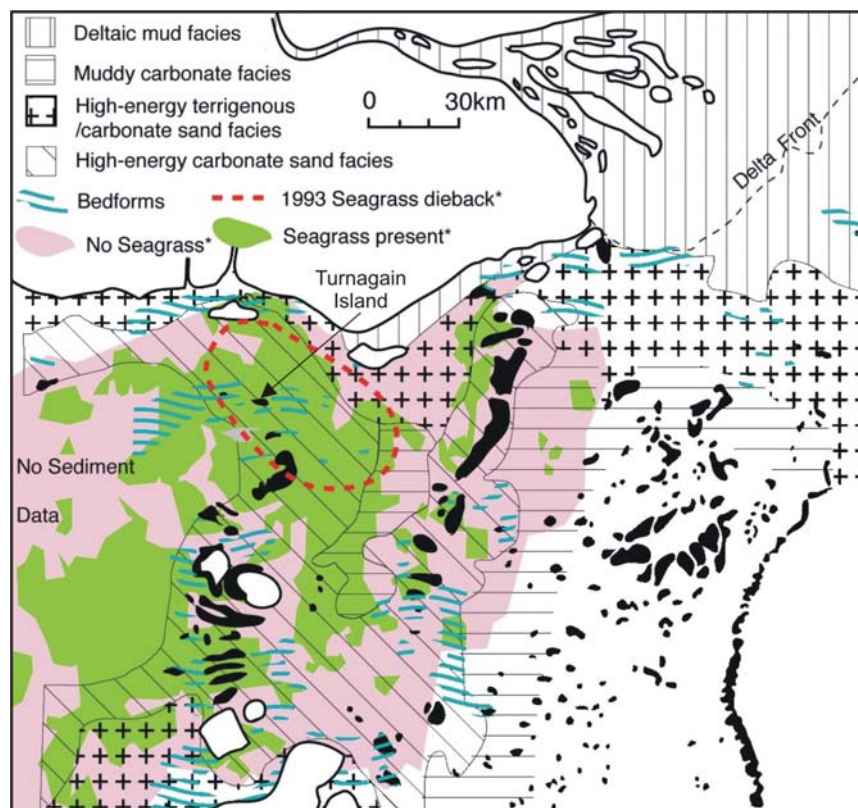


Figure 1.3. Map showing regions of significant seagrass dieback. Areas where widespread seagrass dieback has been documented occur in the vicinity of Turnagain Island. Regions southwest and southeast of Turnagain Island are the focus of this study.



2. Mapping of the distribution and abundance of seabed sediments and benthic habitats at the two sites (focussing on seagrass beds and sandwaves);
3. Classification of seabed sediments and benthic habitats at the two sites;
4. Measurement of the tide and wave currents to determine sediment transport rates over seagrass and sandwaves; and
5. Documentation of the Late Quaternary history of the seagrass and sandwave habitats as an assessment of habitat stability.

A variety of geoscience techniques were applied to realise the scientific objective of the study, including: intensive swath sonar and high-resolution shallow seismic reflection surveys; the capture of high-resolution digital video footage of the seabed; and a detailed program of seabed sampling and shallow coring. All of the data collected on this survey are contained in Geoscience Australia's marine sediment database (MARS) which can be interrogated over the web at <http://www.ga.gov.au/oracle/mars>.

## 1.2. SURVEY PARTICIPANTS

The vessel used for the survey was James Cook University's research vessel *James Kirby* (Fig. 1.4). The RV *James Kirby* is a 20 m converted trawler, with accommodation for 8 participants (including 2 crew), and contains a central winch and A-frame for deployments of up to 1 ton. The A-frame and winch can be used to conduct vibrocoring operations. The multi-disciplinary nature of the research required the efforts of a group of people with a wide variety of complimentary skills to make it successful. The cruise personnel with their substantive expertise are listed below.



Figure 1.4. Photograph of the RV *James Kirby*. The vessel is a 20 m long converted fishing trawler owned and managed by James Cook University in Townsville.

### 1.2.1. Scientific Personnel

Dr Peter Harris (GA) – co-cruise leader 28/03/04 – 05/04/04; sedimentology  
 Dr Andrew Heap (GA) – co-cruise leader 28/03/04 – 18/04/04; sedimentology  
 Dr Mark Hemer (GA) – oceanographer 28/03/04 – 18/04/04; current modelling  
 Mr James Daniell (GA) – computer support 28/03/04 – 18/04/04; swath sonar  
 Mr Simon Kerville (QDPI) – fisheries biologist 28/03/04 – 11/04/04; seagrass  
 Mr Lyndon O'Grady (GA) – marine technician 28/03/04 – 18/04/04

### **1.2.2. Ship's Crew**

Mr Don Battersby (JCU) – skipper

Mr Kevin Hooper (JCU) – deck-hand/electronic technician/swath mapping

## 2. Geophysics

A comprehensive geophysical survey was conducted to determine seabed morphology and the composition of the seabed features. The survey consisted of a regional reconnaissance survey to determine the location(s) of the sandwaves and seagrasses followed by intensive swath mapping of the study areas: Area A and Area B. In each of the study areas, both swath sonar and shallow seismic reflection data were collected. The geophysical surveys were used as the basis for determining the location of the oceanographic moorings ([Section 3](#)) and to design a sediment sampling strategy ([Section 4](#)).

### 2.1. DATA ACQUISITION

Initially, an aerial survey was undertaken to determine the locations of seagrass and sandwaves in the vicinity of Turnagain Island. Digital photographs of the different sedimentary environments taken during the aerial survey were used to define a smaller region for reconnaissance using the swath sonar on the vessel (Figs. 2.1a-b). The aerial survey confirmed that seagrass/algal beds were located next to well-developed sandwaves SW of Turnagain Island and that well-developed sandwaves were located SE of Turnagain Island.

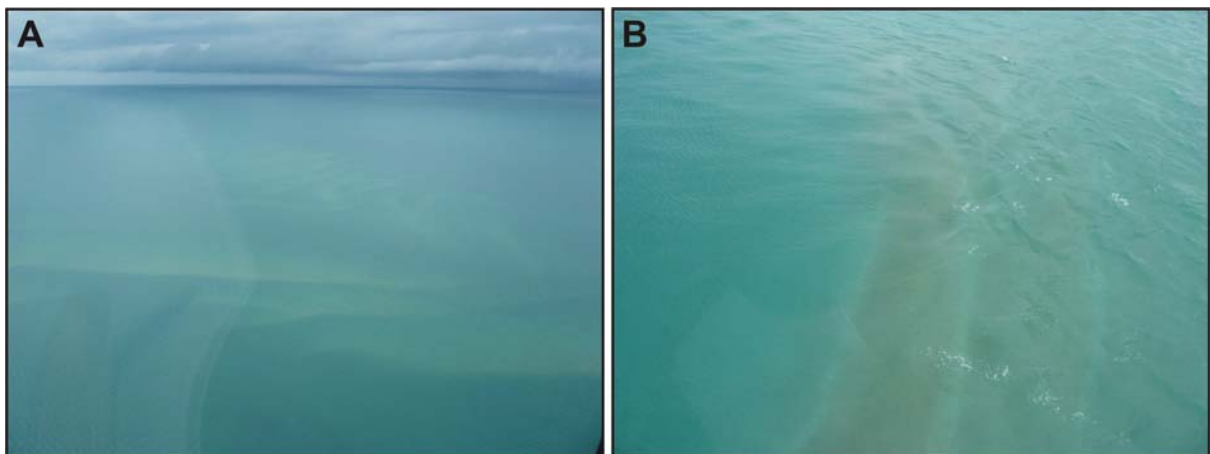


Figure 2.1. Photographs of: a) sandwaves and b) sandwaves and seagrass/algal beds next to Turnagain Island. The photographs were taken during a helicopter reconnaissance survey of the region in conjunction with Queensland Department of Primary Industries and Fisheries scientists. The sandwaves form ribbon-shaped bedforms that are migrating over the seabed. The sandwave crests are white while the seagrass and algal beds form dark/black patches in between the crests.

#### 2.1.1. Swath (Multi-beam) Sonar

A Reson<sup>TM</sup> Seabat 240 kHz swath sonar system (model no. 8101; [Fig. 2.2](#)) was hired from the School of Earth Sciences at James Cook University for the purposes of gathering high-resolution bathymetry and backscatter images of the study area. The swath transducer head was fixed to a pole attached to the starboard side of the vessel's hull. This configuration ensured that the transducer head projected approximately 0.5 m below the hull. The 8101 transducer emits 101 acoustic beams of 1.5° x 1.5° to produce a 150° wide swath of the seabed. Typically, this gives a swath width of approximately 7 times the water depth. The motion sensor was mounted on the centre line and given reference coordinates of  $x = 0$  m,  $y =$



Figure 2.2. Photograph of the Reson 8101(240 kHz)multi-beam sonar transducer/receiver. The unit is attached to a vertical pole on the starboard side and projects approximately 1.5 m below the hull of the vessel. The unit emits and receives 101 beams to obtain bathymetry and acoustic backscatter.

0 m, and  $z = 0$  m, where  $x$  is starboard positive,  $y$  is bow positive, and  $z$  is elevation positive. Relative to the motion sensor, the transducer head was at co-ordinates of  $x = 0.9$  m,  $y = 0.0$  m, and  $z = -3.0$  m, and the DGPS antenna at co-ordinates of  $x = -0.9$  m,  $y = -0.7$  m, and  $z = 9.1$  m. As the survey plan included repeat seabed surveys to monitor changes in topography a high degree of positional accuracy was needed. An Ashtech® G12 differential global positioning system (DGPS) receiver was considered adequate for our survey needs with a quoted accuracy of 0.4 m in the  $x$  and  $y$  plane.

The swath sonar system was operated at 9-11 km hr<sup>-1</sup> (5-6 knots) in smooth to moderate seas. Data from all the peripheral sensors were recorded using 6042 Ver. 7.2 format software. Initially, a regional survey of the seabed near Turnagain Island was undertaken before conducting detailed surveys of two smaller study sites (Fig. 2.3). The reconnaissance survey consisted of several straight intersecting lines that outlined the study sites. The seabed between the study areas was swath mapped along the transit lines. Swath mapping of the study sites was conducted in water depths of 4-12 m, allowing for a maximum ping rate of 20 times per second. To ensure 100% coverage, each site was swathed with a constant line spacing of between 20 and 25 m depending on water depth (closer spacing for shallower water). Despite this, due to significant changes in the shallow bathymetry, this line spacing did not always provide 100% coverage and additional lines were inserted to fill the gaps. Each study site was mapped twice; once at the start of the survey and then again at the end of the survey. The repeat surveys were undertaken 14 days apart to ensure that a full spring-neap tide cycle was captured. Due to time constraints, the second survey did not cover all of the area mapped at the beginning of the survey.

### 2.1.2. Shallow Seismic Reflection

A Datasonics™ 3.5 kHz Chirp sub-bottom profiler (recorder model no. DSP661/66; tow fish model TTV170S) was towed at 9-11 km hr<sup>-1</sup> (5-6 knots) in smooth to slight seas (Fig. 2.4). The

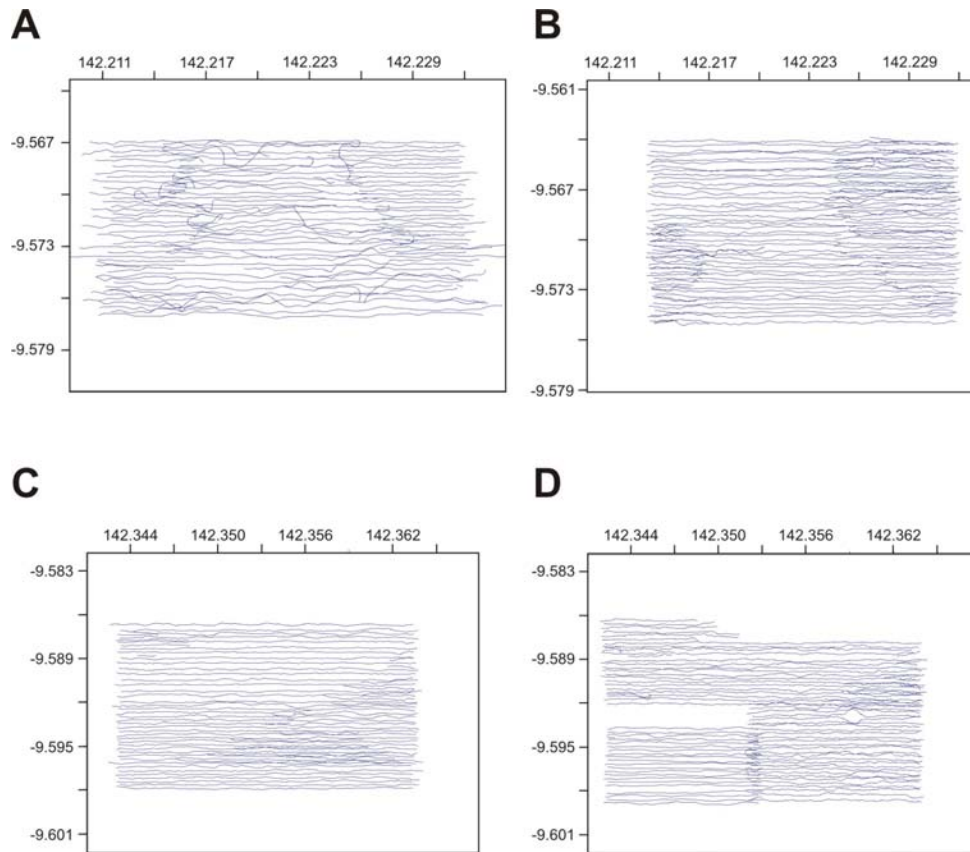


Figure 2.3. Maps showing the survey track lines for: a) Area A survey 1, b) Area A survey 2, c) Area B survey 1, and d) Area B survey 2. Area A is located SW of Turnagain Island and Area B is located SE of Turnagain Island.



Figure 2.4. Photograph of the Chirp (3.5kHz) seismic reflection tow-fish. The tow-fish was towed behind the vessel approximately 3 m below the water surface at 9-11 km hr<sup>-1</sup> in smooth to slight seas.

tow-fish was located approximately 3 m below the sea surface on the port side of the vessel. The trigger interval was set at 0.25 seconds. The sub-bottom profiler was operated in unison with the swath sonar system on the first survey of each study site.



## 2.2. DATA PROCESSING AND ANALYSIS

Processing of the multi-beam sonar data was a priority. This is because it was necessary to monitor the data to assist with site selection and in improving the survey plan (line spacings, line lengths etc). All of the post-processing of the swath sonar data, including data editing, tide corrections and sound velocity profile corrections were undertaken using the Caris™ HIPS/SIPS v5.3 processing software. Data from the sub-bottom profiler was not processed or interpreted during the survey.

### 2.2.1. Swath (Multi-beam) Sonar Data

The swath sonar data were initially acquired in the proprietary Reson™ \*.db format. Each line consisted of a separate file to keep the file sizes manageable. The data for each line were converted to Extended Triton-Elics (XTF) format using the *ExportXTF* module supplied with the Reson™ 6024v7 software. This conversion allowed the data to be imported into the Caris™ HIPS/SIPS processing software.

#### 2.2.1.1. General Processing Procedure

The acoustic signals were corrected for temperature and salinity of the seawater using an Applied Microsystems Ltd SV PLUS™ acoustic velocity profiler. As expected, the sound velocity profiles showed very little variation through the water column, which is well mixed. The acoustic velocity of seawater was measured at 1,541-1,543 m s<sup>-1</sup>.

Pressure sensors on the current meters in Areas A and B recorded tidal heights during the survey. These heights were used to correct the swath data to mean sea level. Finally, individual soundings were visually inspected using the Caris™ HIPS/SIPS processing software and bad data were removed to create a level and clean dataset relative to mean sea level.

#### 2.2.1.2. Data Analysis and Presentation

Data were then gridded at 1 m cell size. This spatial resolution was considered appropriate for the size of the survey areas, and given the quality and density of the data. Data density was estimated by calculating the number of soundings per hour, then calculating the area covered per hour and the average number of pings per m<sup>2</sup>. The number of soundings per hour (S) is calculated as follows:

$$S = r * n \quad (1)$$

where  $r$  is the ping rate per hour and  $n$  is the number of beams (101). Then the area covered by the sonar per hour (A) is calculated:

$$A = v * (h * \tan(w/2))^2 \quad (2)$$

where  $v$  is average ship speed (m s<sup>-1</sup>),  $h$  is the average water depth (m) and  $w$  is the swath width (m). Finally, the number of pings per square meter (P), which is an estimate of the data density, is calculated from Equations 1 and 2, as follows:

$$P = \text{Eq 1} / \text{Eq 2}. \quad (3)$$

Initial estimates with a ping rate of 20 sec<sup>-1</sup>, velocity of 10 km hr<sup>-1</sup> (~5 knots), and an average water depth of 7 m yielded approximately 14 pings per m<sup>2</sup>. This value is only an estimate of the data density because the calculations assume a flat seabed, and the actual ping density varies with distance from the central beam (due to the angular offsets of the beams) and the true water depth at each location.

Attempts to grid the data at higher resolutions (e.g., 0.5 m cell size) did not significantly improve the quality of the bathymetry grid. In fact, gridding the data at higher than 1 m<sup>2</sup> highlighted artefacts caused by vibrations of the swath head, which were resolved as ~10 times per second at <0.5 degree. Smaller grid sizes also resulted in data gaps between pings of the outermost beams.

### **2.2.1.3. Data Quality and Errors**

The shallow water depths in the study area allowed for a high rate of data acquisition, and a ping rate of 20 times per second was used. The shallow water depths also produced accurate bathymetric soundings over the entire 150° of the swath (i.e., the quality of the soundings was relatively consistent across all 101 beams). Data quality varied during the survey, although the overall quality was adequate for the purpose of the study. The quality of the data was degraded to variable degrees by waves, strong tidal currents, and a gyrocompass bias.

During ideal conditions, the swath sonar survey was able to delineate small sandwaves (0.2 m high). However, these subtle features were not discernible when waves up to 1.5 m were present. Strong tidal currents also affected the ability of the boat to maintain a constant heading along each of the survey lines. In effect, this caused roll artefacts at a lower frequency than could be measured with the motion sensor. A model is being developed to remove these low-frequency motions. Problems with the gyrocompass during the survey caused errors of between -10° to +7°. Corrections have been estimated using the Caris HIPS/SIPS processing software and applied to the raw data. The cause of the gyrocompass bias could not be determined.

### **2.2.2. Shallow Seismic Reflection Data**

Data from the Datasonics™ 3.5 kHz Chirp sub-bottom profiler was processed using the following standard procedure:

1. data from the two recorded channels were stacked to reduce the signal to noise ratio,
2. the signal was then de-biased, and
3. the data were then converted to standard 32 bit Seg-Y format.

The data were then viewed in the seismic processing software package SeisVU ([www.phoenixdatasolutions.co.uk](http://www.phoenixdatasolutions.co.uk)) where salient features were resolved. The profiles were saved as bitmaps (.bmp) and a hard-copy printed for interpretation.

The acoustic character of the reflections in the Chirp profiles was then interpreted based on a classification devised by Damuth (1980). This scheme classifies the reflections based on their clarity, continuity and morphology into three major echo-types:

Echo-type I: distinct;

Echo-type II: indistinct – prolonged; and

Echo-type III: indistinct – hyperbolae.

These echo-types are then further sub-divided based on presence or absence of sub-bottom reflectors, degree of prolongation, and relationship of hyperbolae to the seabed. Polygons

were drawn by eye around the interpreted echo-types along each line with reference to bathymetry. The acoustic facies maps are available to ground-truth against data collected in the area.

## 2.3. RESULTS

### 2.3.1. Swath (Multi-beam) Sonar

In total, including the transit lines, the swath mapping survey comprised 467 lines which amounted to 548 line-km of data. Data were acquired over 13 days with a total volume of 25 gigabytes. The regional reconnaissance survey consisted of 71 line-km and the detailed mapping surveys of Area A and B consisted of 245 and 232 line-km, respectively (Table 2.1). This equated to a surveyed area of seabed of 3.0 km<sup>2</sup> and 2.4 km<sup>2</sup> for Area A and B, respectively. Due to time constraints and shallow water depths not all of the survey in Area A could be repeated. The second surveys covered 1.9 km<sup>2</sup> and 2.5 km<sup>2</sup> of the seabed for Area A and B, respectively.

Table 2.1. Details of swath (multi-beam) sonar surveys.

Site	Survey	Length (km)	Width (km)	Area (km <sup>2</sup> )	Number of Lines	Total Line-km
Regional	Reconn.	n/a	n/a	n/a	23	71
Area A	Survey 1	2.0	1.5	3.0	120	146
	Survey 2	1.8	1.1	1.9	110	99
Area B	Survey 1	2.0	1.2	2.4	145	129
	Survey 2	2.1	1.2	2.5	88	103

The results of the regional reconnaissance survey revealed that there were well-developed sand ridges in the vicinity of seagrass beds to the SW of Turnagain Island and that there were well-developed sandwaves without seagrass beds to the SE of the island. These two areas were selected for detailed study and represent the major sedimentary environments in Torres Strait that could be used to examine how sandwave movement might affect the survival, burial and possible death of seagrasses. The regional reconnaissance survey also determined that the water depths throughout the region were between 3 m to 12 m.

#### 2.3.1.1. Area A

Area A represents a region of the seabed where sand ridges occur in close proximity to abundant seagrass and algal beds. The area is characterised by two flat-topped platforms along the west and east margins, separated by a deeper region of gently undulating hard seabed in the north and a NW-SE trending ridge in the south (Fig. 2.5). The shallow seismic sections indicate that this region of relatively shallow water is most probably a (mobile?) body of unconsolidated sand. Water depths over the platforms range from 4.5 m to 6 m and the surfaces are relatively flat, with most of the surface occurring between 5 to 5.5 m water depth (Fig. 2.5). The edges of the platforms are very irregular, with what appear to be dissolution features. Several irregularly-shaped depressions of up to 2 m deep and 6,000 m<sup>2</sup> occur locally and the platform surfaces have a karst-like appearance. In the east, sinuous crested discontinuous sand ridges occur on the surface of the platform. The sand ridges are

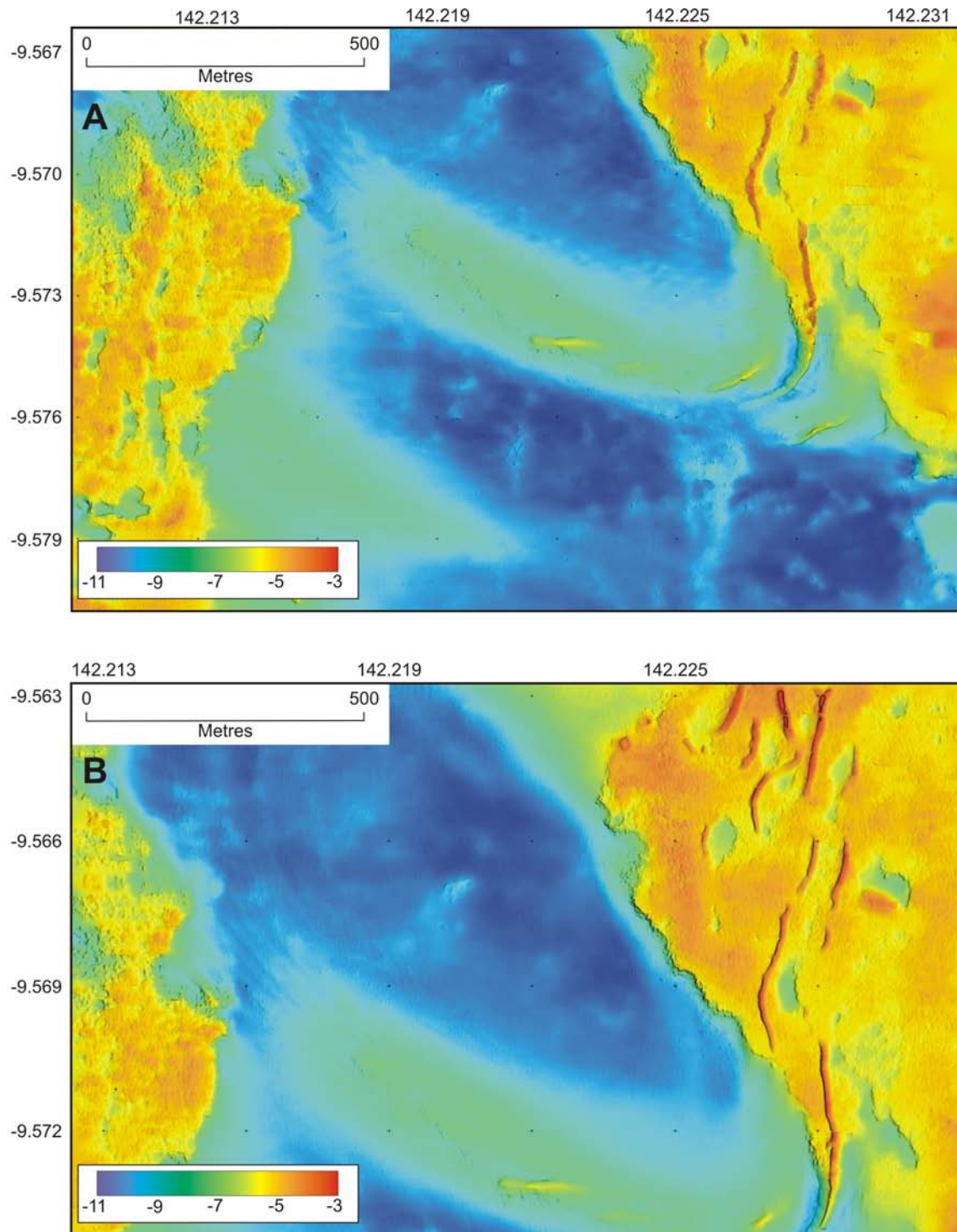


Figure 2.5. Maps showing bathymetry for Area A for a) survey 1 and b) survey 2. Area A consists of two relatively shallow marginal platforms and a deeper central region comprised of hard-grounds and sand ridge. The eastern platform contains a series of SSW-trending sinuous- to straight-crested sand ridges. Smaller sand waves occur on the southern flank of the sand ridge in the central region. Comparison of the bathymetry between survey 1 and 2 revealed that the crests of the sand ridges had moved up to 19.3 m to the west (see Fig. 2.13a).

up to 1 m high and up to 40 m wide, trend NNE-SSW and as a group extend from north to south in the study area. In the south, a sand ridge extends off the platform and curves around towards the NW and connects to the sand body located between the platforms. In the south, sandwaves <0.2 m high and 15 m wide occur on the western flanks of the sand body.

Based on their morphology the platforms are interpreted to be reefs. The hard-ground in the north appears to be the old land surface that was exposed when Torres Strait was emergent. The sand body in the south is possibly a sand ridge that may be migrating between the reef platforms. The second survey in this region indicated that the crests of the sand ridges had moved up to 19 m towards the west (see [Section 2.4.1](#)).

### **2.3.1.2 Area B**

Area B represents a region of the seabed where sandwaves occur but not seagrasses. The area is characterised by an impressive group of mobile sandwaves that form part of a triangular-shaped bedform that trends east-west across the study area ([Fig. 2.6](#)). The bedform widens from 250 m in the west to >1200 m in the east, after bifurcating into two arms consisting of well-developed sandwaves. The sandwaves have NNE-SSW trending sinuous crests, except for those located in the far SE on the southern arm where the crests trend NNW-SSE. Sandwaves on this bedform are up to 3.5 m high with crests generally spaced between 20-100 m apart. The sandwaves get bigger and more pronounced towards the east. Some of the larger sandwaves are more than half the water depth, and are double-crested in places, indicating that waves have a significant influence on their formation and morphology. Another group of sandwaves, presumably forming part of another larger bedform to the north, occurs in the NW corner of the study area. The crests of these sandwaves are also sinuous and trend NNW-SSE. Super-imposed on the stoss slopes of many of the largest sandwaves are smaller dunes ([Fig. 2.7](#)). These secondary dunes are up to 0.5 m high and 0.5 m wide. They have straight, sinuous and arcuate crests that locally bifurcate. Smaller dunes also form “ladder-structures” in the troughs of the larger sandwaves ([Fig. 2.8](#)). The wide variety of sandwave types and orientations indicates that water movements around the sandwaves are highly complex. Surrounding the sandwaves is a region of relatively shallow water, where water depths are mostly 9-10 m ([Fig. 2.6](#)). This region is probably a sheet of mobile sand. Underlying the sandwaves and mobile sand sheet is a gently undulating surface that occurs in water depths of 11-12 m ([Fig. 2.6](#)). From its morphology and elevation this surface is probably the old land surface that was exposed when Torres Strait was emergent. The second survey indicated that the crests of the sandwaves had moved towards the west as much as 16 m (see [Section 2.4.1](#)).

## **2.3.2. Shallow Seismic Reflection**

A total of 275 line-km of digital shallow seismic reflection data (30 GB) were collected. Very little penetration of the subsurface sediments was achieved due to the coarse and cemented nature of the seabed. The Chirp system was not powerful enough to penetrate the seabed and the resulting profiles were all limited to less than 10 ms penetration. The profiles thus really only defined the seabed and occasionally some prominent sub-bottom reflections. Bitmaps (.bmp) of the profiles are contained in [Appendix B](#) on the attached CD.

### **2.3.2.1. Area A**

A total of 67 shallow seismic profiles were collected in Area A. All of the profiles contain a very distinct reflector (up to 3 ms) that traces an irregular surface over the entire study area ([Fig. 2.9](#)). The amplitude of this reflector attains 11,000 dB per 1  $\mu$ pa and varies considerably along each profile. This upper reflector is interpreted to be the present seabed based on it



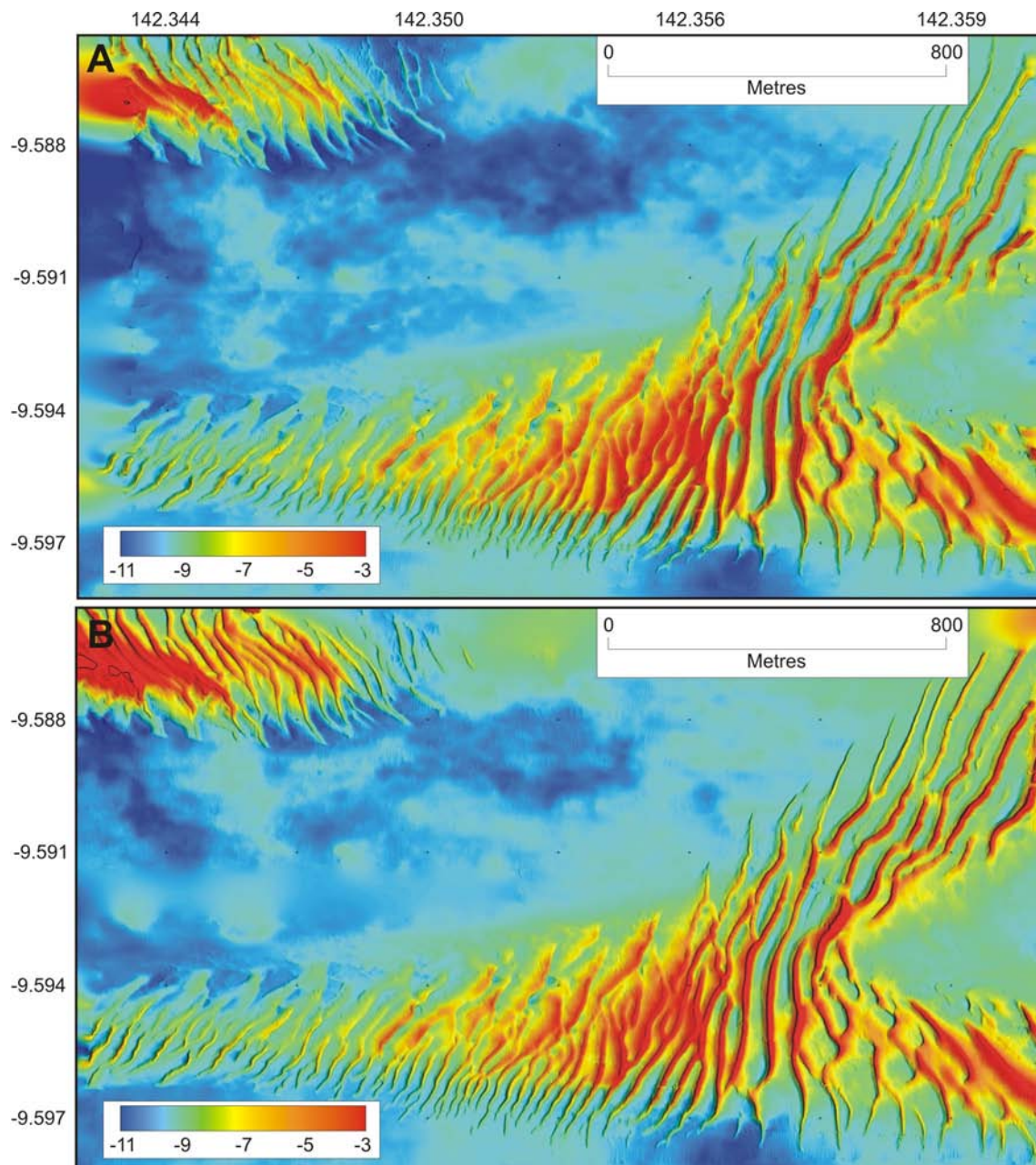


Figure 2.6. Map showing bathymetry for Area B for a) survey 1 and b) survey 2. Area B consist of two fields of SE-trending sinuous- to straight-crested sandwaves separated by hard-grounds. The sandwaves attain 3.5 m in height and are spaced 20-200 m apart. Comparisons of the bathymetry between survey 1 and 2 revealed that the crests of the sandwaves had moved up to 16 m to the west (see Fig. 2.12b).

being the first distinct reflector below the sea surface. It traces the morphology of the seabed which consists of two relatively shallow regions with very irregular surfaces characterised by prolonged reflections (up to 2 ms) on the margins, separated by a relatively deep undulating and flat region characterised by distinct reflections (Fig. 2.9a). Sub-bottom reflections also occur locally. They are faint to indistinct, prolonged and of variable amplitude (Fig. 2.9b). These subsurface reflections trace an irregular surface, especially in the south, which is interpreted to be the old land surface of Torres Strait when it was emergent. Regions where this surface is characterised by high amplitudes probably represent harder (cemented?) grounds. Adjacent to the western platform, sediments between the seabed and subsurface

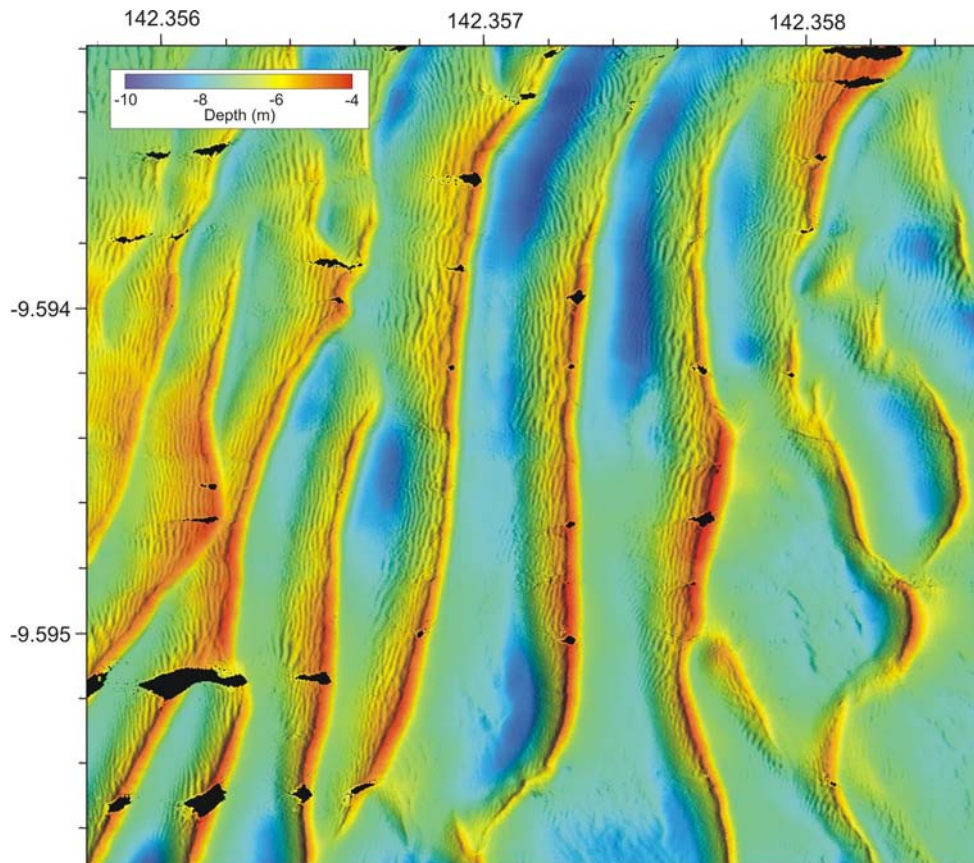


Figure 2.7. Map showing smaller secondary dunes super-imposed on the stoss slopes of the larger sandwaves. These smaller dunes are attain 0.5 m in height and 0.5 m wide. They are migrating up the slopes of the larger bedforms.

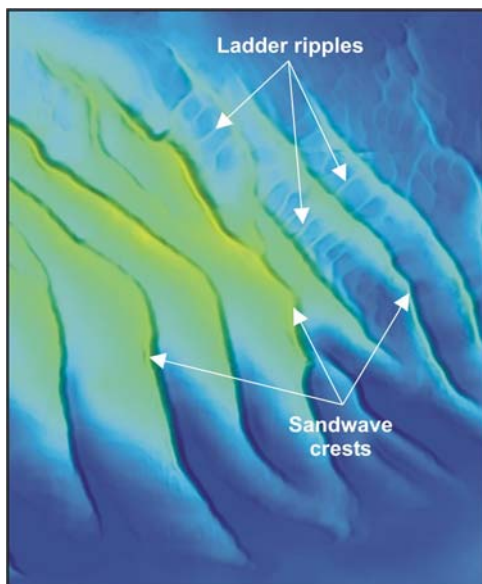


Figure 2.8. High-resolution bathymetry map showing “ladder ripples” in between the sandwave crests in Area B. These dunes form from currents running between the sandwave crests. These secondary structures indicate complex tidal motions in the vicinity of the sandwaves.

reflector are acoustically opaque and attain a thickness of 5 ms (Fig. 2.9b). This depositional feature is interpreted to be a talus slope connected to the platform. The subsurface reflections can be traced underneath the sand ridge between the two platforms and the sand ridges on the eastern platform. The profiles thus reveal that the sand ridges have



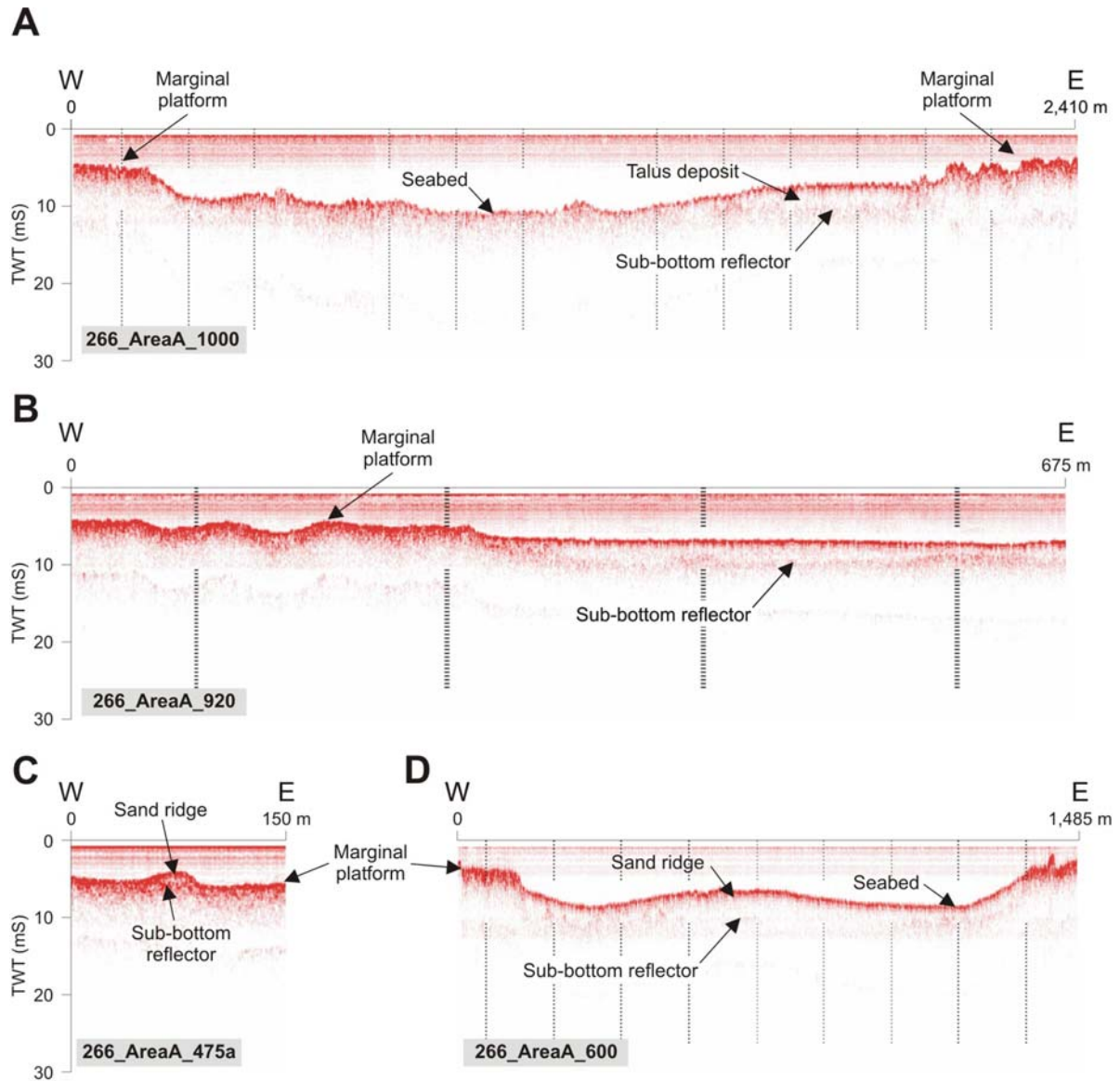


Figure 2.9. Chirp shallow seismic reflection profiles for Area A showing: a) the morphology of the seabed, b) sub-bottom reflectors, and c-d) sand ridges over acoustic basement. The seabed is interpreted at the first strong continuous reflection of regional extent below the sea surface. Sub-bottom reflections depict an irregular surface that is interpreted to be the old land surface when Torres Strait was emergent. The sand ridges occur over this surface. All the profiles for Area A are located in Appendix B.

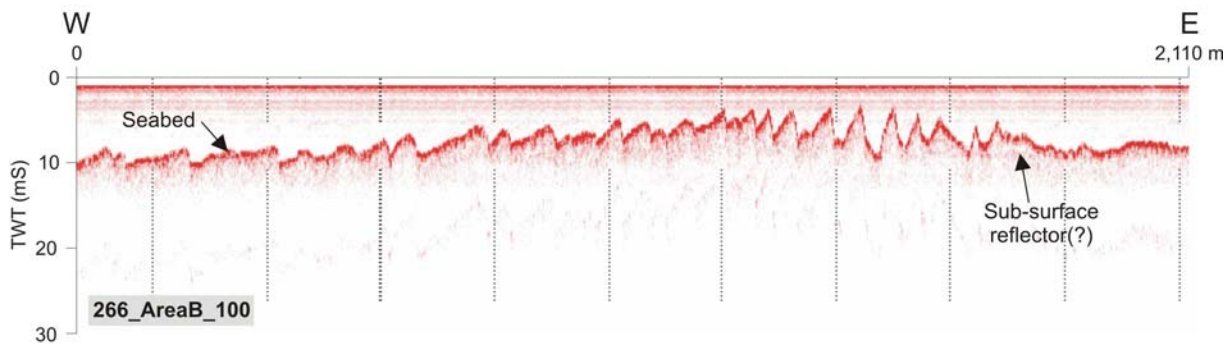
accumulated over the underlying surfaces (Figs. 2.9c-d). The sand ridge between the platforms attains a thickness of 4.5 ms and the sand ridges on the eastern platform attain a thickness of ~2 ms. In both cases the sediments that make up the sand ridges are acoustically opaque suggesting that they could be comprised of similar material.

#### 2.3.2.2. Area B

A total of 46 shallow seismic profiles were collected in Area B. All of the profiles contain a very distinct reflector (up to 2 ms) that traces an irregular surface (Fig. 2.10). The amplitude of the seabed reflector attains 4,000 dB per 1  $\mu$ pa and is uniform throughout the study area. This upper reflector is interpreted to be the present seabed based on it being the first distinct



**A**



**B**

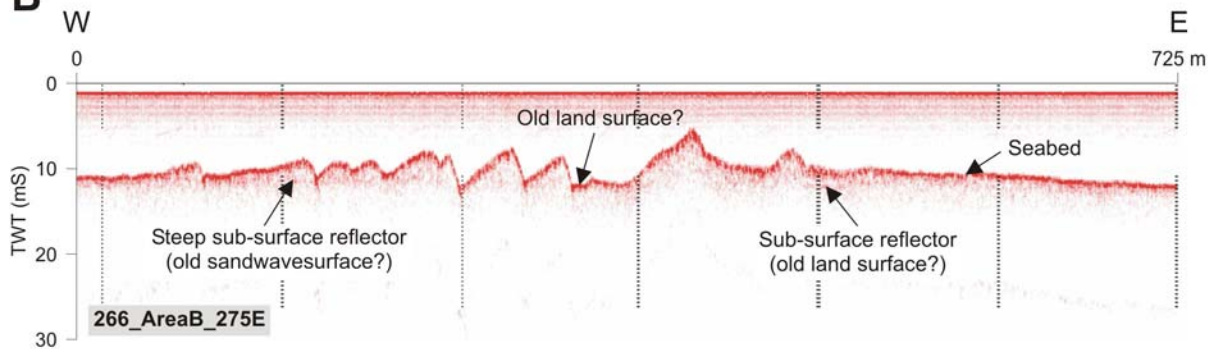


Figure 2.10. Chirp shallow seismic reflection profiles for Area B showing: a) the morphology of the seabed and b) sub-bottom reflectors. The seabed is interpreted to be the first strong continuous reflection of regional extent below the sea surface. The sandwaves occur and are possibly migrating over an underlying surface that is interpreted to be the old land surface when Torres Strait was emergent. All the profiles for Area A are located in Appendix B.

reflector below the sea surface. It traces the morphology of the seabed which is dominated by the numerous and distinctive sandwaves. In some places, sub-bottom reflectors occur within the sandwaves (Fig. 2.10b). These internal reflectors are very faint, indistinct and sub-parallel to the seabed reflector. Where they are at relatively high angles to the seabed, they are interpreted to be older (cemented?) bedding planes tracing previous sandwave surfaces (Fig. 2.10b). Where they are relatively horizontal to the seabed, they are interpreted to be the old land surface that was exposed when Torres Strait was emergent (Fig. 2.10b). Otherwise the sandwaves and surrounding seabed regions are acoustically opaque.

### 2.3.2.3. Acoustic Facies

A total of four major echo-types were observed in the study areas (Table 2.2).

Table 2.2. Descriptions of echo-types observed in Area A and B.

Echo-type*	Classification	Description
IA	Distinct	Sharp, continuous echo with no sub-bottom reflectors
IC	Distinct	Sharp, continuous with non-conformable sub-bottom reflectors
IIB	Indistinct – prolonged	No sub-bottom reflectors
IIIC	Indistinct – hyperbolae	Hyperbolae with varying vertex elevations

\* After Damuth, 1980.

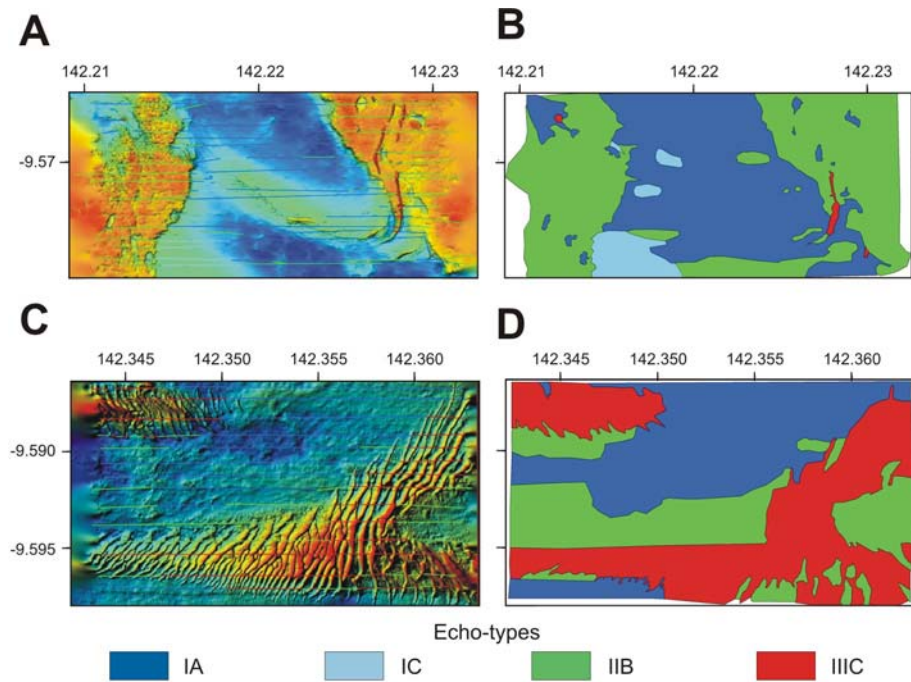


Figure 2.11. Maps showing acoustic facies interpreted from the Chirp shallow seismic profiles for: a) Area A and c) Area B. The echo characters were converted to polygons between the lines for: b) Area A and d) Area B.

In Area A, echo-types IA and IIB are dominant (Figs. 2.11a-b). Echo-type IA occurs in the centre of the area and locally associated with small seabed depressions. This echo-type is associated with deep regions and smooth seabed morphology. Echo-type IIB occurs in the east, west and south. This echo-type is associated with shallower regions and rough seabed morphology. Echo-type IC occurs in the centre of the area and to the south. This echo-type displayed one non-conformable sub-bottom reflector. Echo-type IIIC occurs locally associated with shallower regions and rough topography in the southeast and northwest, associated with ridges and small peaks.

In Area B, echo-types IA, IIB and IIIC were observed (Figs. 2.11c-d). Echo-type IA occurs in the north and south, associated with deep regions and smooth seabed morphology. Echo-type IIB generally occurs adjacent to echo-type IIIC. Where these echo-types occurred, the profiles display a greater degree of substrate penetration than Type IA. However, no sub-bottom reflectors occur in each case. Echo-type IIIC occurs in the northwest and south, southeast, associated with the undulating seabed forming the sandwaves. Single, non-overlapping hyperbolae occur in the seabed reflector associated with the steep slopes of the sandwaves.

## 2.4. SEDIMENT AND SANDWAVE MOVEMENT

The repeat swath surveys present an opportunity to quantitatively ascertain sediment and sandwave movement in Areas A and B over the period of the survey. By comparing the bathymetry at the beginning of the survey with that at the end of the survey enables changes in the seabed morphology to be calculated. Due to the very high resolution swath data (1 m<sup>2</sup>), very small changes in the position and form of the seabed can be determined in unprecedented detail. This extends to measuring the movement of the entire form of a seabed feature rather than inferring the movement from a single measurement location (e.g.,

from an oceanographic mooring). A comparison of sediment transport and sandwave movement as determined by the repeat swath sonar surveys and well-established sediment transport equations (see [Section 3.3.3](#)) has been undertaken. A discussion of this comparison is presented in [Section 5](#).

### 2.4.1. Sandwave Migration

Determining the distance and direction the sandwaves had migrated during the survey was undertaken using the swath sonar data.

#### 2.4.1.1. Data Analysis

In order to provide a rigorous method for determining the precise locations of these crests an aspect algorithm was applied to the digital elevation model (DEM) using the ERMMapper software package. The aspect algorithm calculated the azimuth of the slope for each pixel in the digital elevation model. For the purposes of this study the sandwave crests were defined as the boundary between the lee and stoss sides of the sandwave. The boundary between both sides of the sandwave is represented by a change in aspect of approximately 180 degrees. The aspect algorithm provided a rigorous definition of the sandwave crests.

The position of the sandwave crests was then digitised every 2 m along the crest-line for Survey 1 and Survey 2. Once the crests were digitised, the ERMMapper vector files were further processed using Perl and FORTRAN code to calculate the migration distances, as follows ([Figs. 2.12-2.13](#)):

1. The ERMMapper vector files for the surveys were broken down into pairs of sequential eastings and northings corresponding to the crest locations at survey 1 (e1, n1) and survey 2 (e2, n2);
2. Nodes every 2 m along the crest line were then assigned locations between the pairs of eastings and northings;
3. Profiles were created for each node in a direction perpendicular to the easting and northing pairs; and
4. A script was run to determine where each profile intersected the crest lines of the second survey.

In both Area A and B, the distance between the beginning and end locations of the crests was then used as an estimate of the net movement of the sandwaves. The shortest distance and its azimuth were recorded as being the migration distance and direction for the sandwaves.

#### 2.4.1.2. Patterns of Migration

The results of the analysis indicate that generally the crests of the sand ridges and sandwaves were displaced towards the west over the period of the survey ([Figs 2.13a-b](#)). The maximum displacement occurred on the crests of the sand ridges in Area A. In Area A, the crests were displaced from 5.1 m up to a maximum of 19.3 m ([Fig. 2.13a](#)). Interestingly, the amount of displacement was consistently higher for sand ridges located on the platforms. In Area B, the crests were displaced from <1 m up to a maximum of 16.0 m ([Fig. 2.13b](#)).

In both Area A and B, the amount of displacement was not constant along the length of the crest, with greatest displacement occurring in the centre of the crests. Generally, the amount of displacement increased with the height of the sandwave and the total displacement was least on the extremities of the sandwave crests, where the sandwaves had

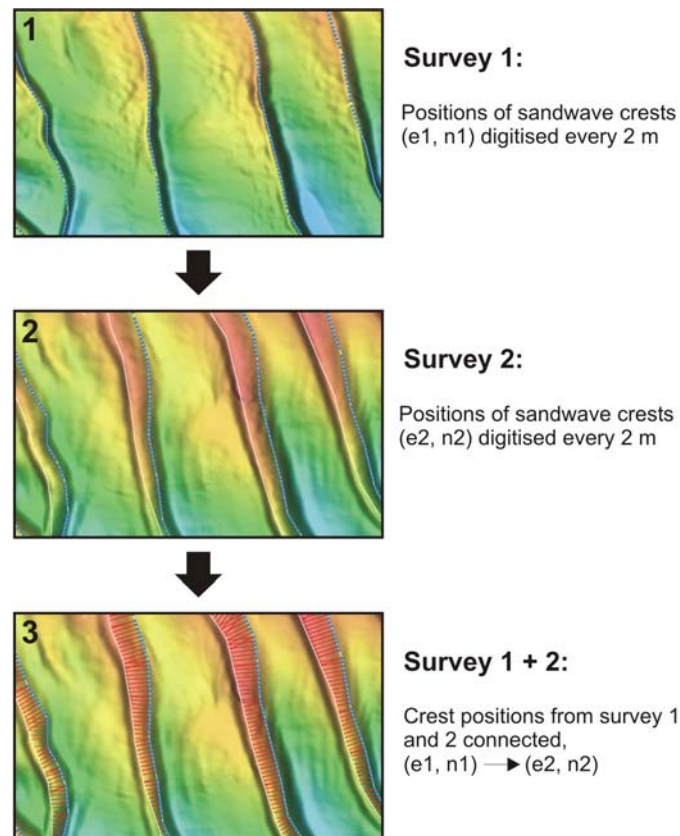


Figure 2.12. Maps showing the method used for computing the distance the sand ridge and sandwave crests moved between the repeat surveys. The location of the crest for survey 1 was digitised every 2 m (a) and then the location of the crest for that sandwave for survey 2 was digitised every 2 m (b) and the points connected (c). The separation between the points was then used to calculate the distance moved.

least elevation. In Area B, the crests of sandwaves in the east of the main bedform showed the greatest amount of displacement, with many sections of the crest moving >10 m to the west. The crests of sandwaves in the west of the main bedform were generally displaced <6 m.

Using the repeat swath sonar surveys, which provide 100% coverage of the seabed bathymetry, it is possible to calculate the volume of sand that was displaced over the period of the survey (Figs. 2.14a-b). Maximum volumes of sand transported over the period the survey reached 3 m<sup>3</sup>. The volume of sand transported was not constant along the crests of the sandwaves. A complex pattern is evident with no direct correlation between where the largest volumes of sand were deposited and regions where the largest volumes of sand were removed. This complex pattern is partly attributed to the fact that up 0.5 m<sup>3</sup> of sand was deposited in regions between the sandwaves (see especially Fig. 2.14b). Regions where sand accumulated between the sandwaves generally also coincide with regions where greatest sand volumes accumulated on the sandwave crests. Some of this westward moving sand may have also accumulated on the eastern flanks of the sandwaves and reduced the apparent volume of sand removed from the crests.



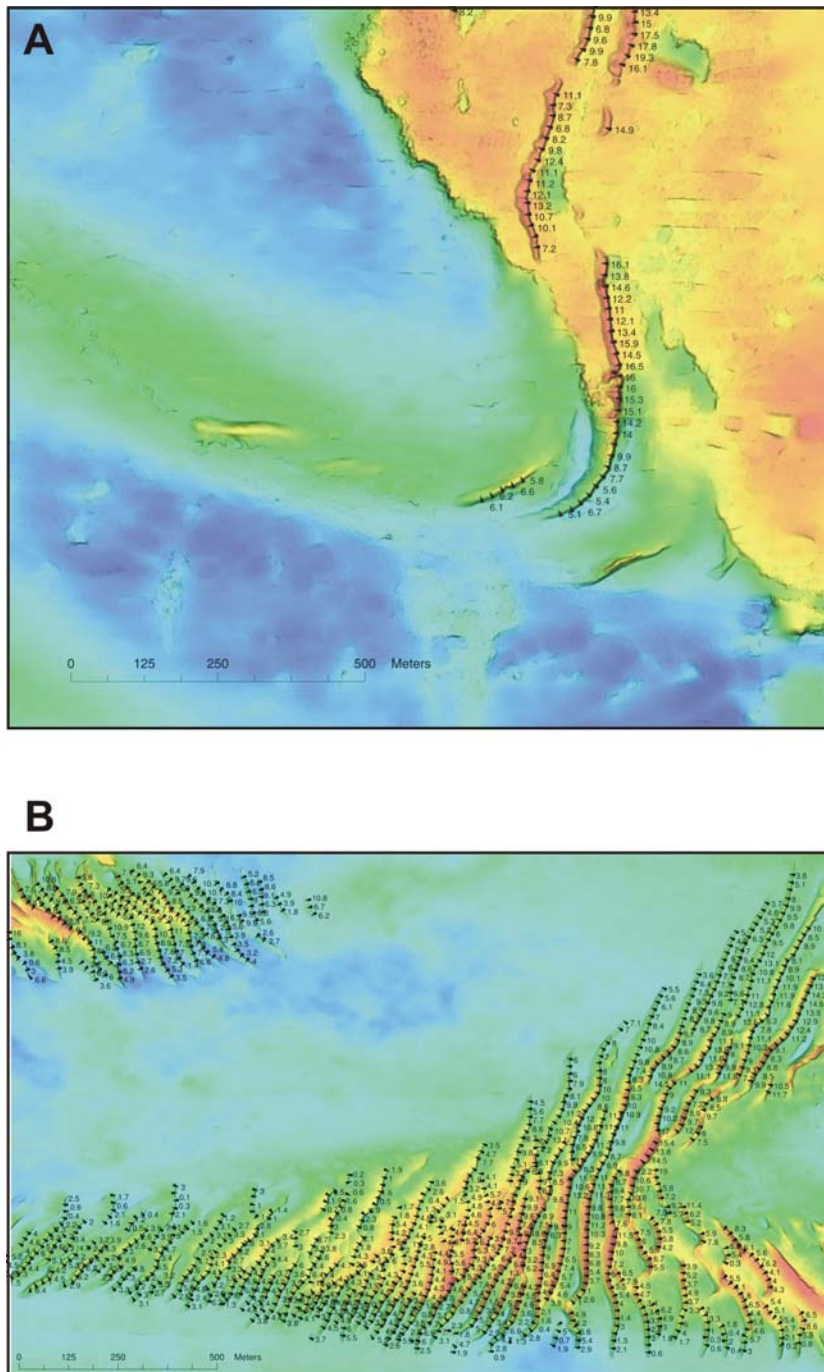


Figure 2.13. Maps showing the total distance moved by the crests between survey 1 and survey 2 for a) the sand ridges in Area A, and b) the sandwaves in Area B. The positions depicted in the figure are those digitised in Figure 2.12.

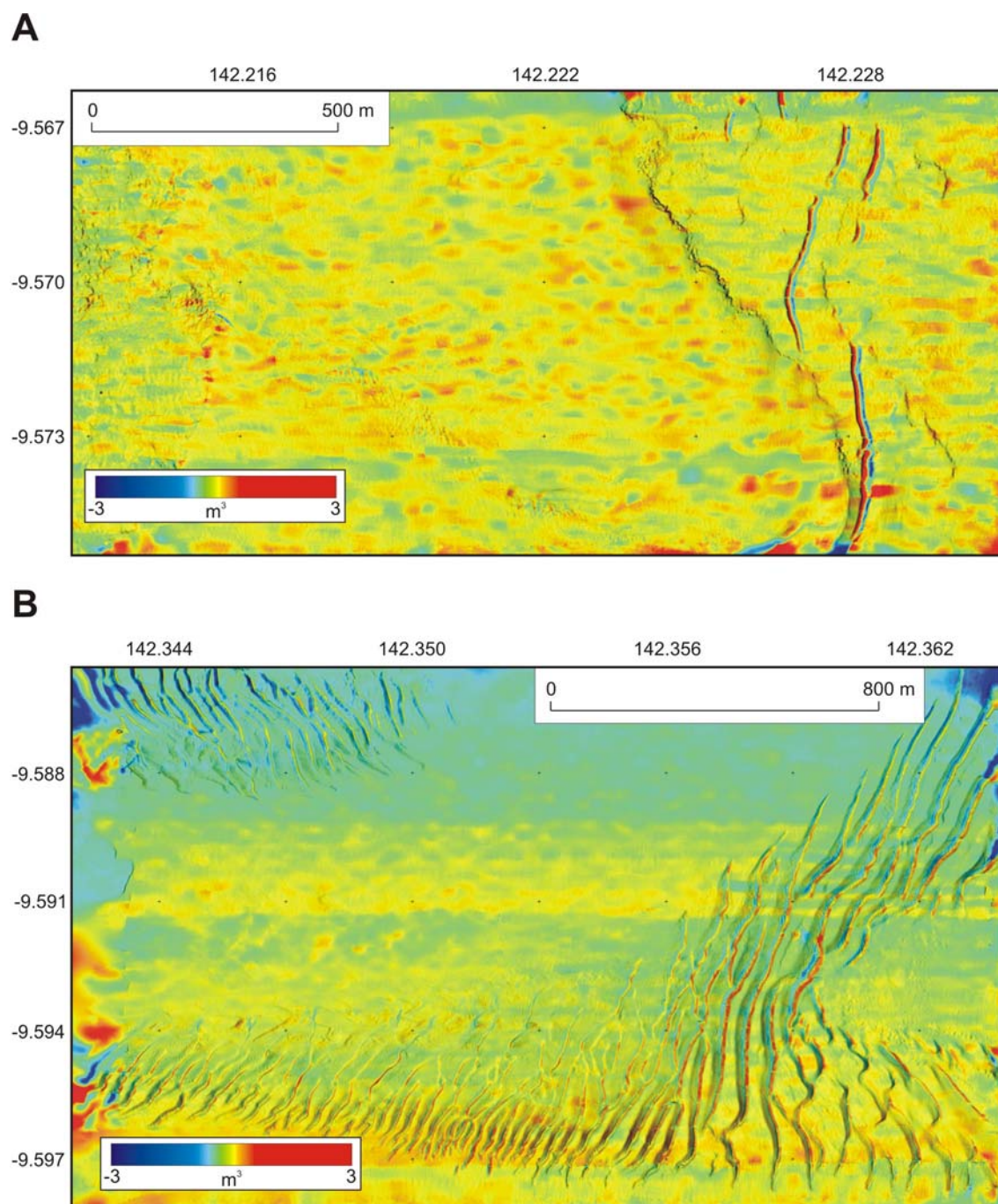


Figure 2.14. Map showing the total volume of sediment moved between survey 1 and survey 2 for a) Area A and b) Area B. Red areas show regions that gained sediment and blue regions show regions that lost sediment. The maximum volume of sediment moved between the two surveys attained  $3 \text{ m}^3$  in Area B. The volume of sediment moved increased with sandwave height.



### 3. Oceanography

#### 3.1. DATA ACQUISITION

The hydrodynamic conditions of the study areas were recorded with an array of instruments designed to measure the hydrodynamics, water temperature, salinity, light, water depth and turbidity. Four oceanographic moorings were deployed, including Geoscience Australia's oceanographic mooring (BRUCE) and three moorings deployed by CSIRO Marine Research (CSIRO-1, CSIRO-2, CSIRO-3, Fig. 3.1).

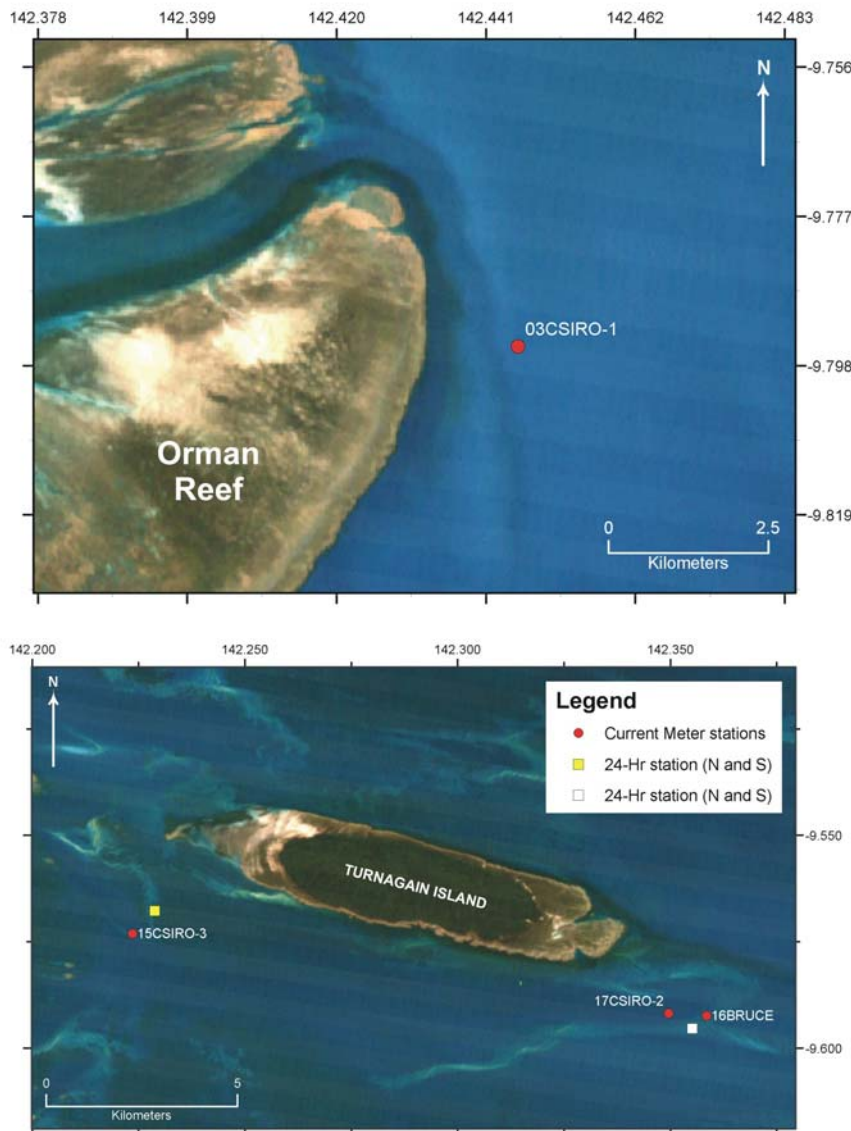


Figure 3.1. Maps showing the location of the oceanographic moorings and 24-hr stations next to a) Orman Reef and b) Turnagain Island. Yellow square = 24-hr station in Area A; while square = 24-hr station in Area B.

##### 3.1.1. Geoscience Australia Oceanographic Mooring (BRUCE)

The Geoscience Australia *Benthic Research frame for Underwater sediment Concentration Experiments* (BRUCE) was deployed on top of a large sandwave south-east of Turnagain

Island in Area B at location -9° 35.547' S, 142° 21.514' E in 9.5 m water depth. Calibration of the optical instruments were carried out between 23:47 28/03/04 UTC and 00:17 29/03/04 UTC. The mooring was deployed at 02:31 29/03/04 UTC, and recovered at 03:25 16/04/04 UTC, resulting in a total deployment length of 18.1 days. The aim of the deployment was to quantify sediment transport rates as a result of waves and currents in Area B, where no seagrass is observed.

BRUCE comprises a 300 kg weighted stainless-steel frame equipped with:

1. A Nortek™ Vector Acoustic Doppler Velocimeter (ADV #N4103). This instrument was positioned to sample at 1.0 m above the bed. The vector uses acoustic sampling techniques to measure flow in a remote sampling volume (Nortek, 2000). The instrument was programmed to burst sample every 20 minutes for 90 s at 8 Hz to measure turbulence from waves. This instrument logs vector components of velocity (east, north and up), pressure and temperature internally to be downloaded on recovery. The Nortek vector (ADV #N4103) contains 82 MB of internal memory (or ~2,000,000 samples).
2. A type-B Sequoia™ Laser In-Situ Scattering and Transmissiometry – 100 (LISST-100) transmissometer laser particle sizer (LISST #104579). This instrument was positioned to sample at 0.3 m above the bed. The LISST measures the scatter of a laser light source to infer the size distribution of suspended matter (Agrawal & Pottsmith, 2000). The LISST was programmed to burst sample for 90 s at 2 Hz at the commencement of the ADV burst (i.e., every 20 minutes). The instrument internally logs the scattering at 32 angles; size distribution as concentration ( $\mu\text{l l}^{-1}$ ) in 32 log-spaced size bins ranging from 1.25-250  $\mu\text{m}$ ; optical transmission; water depth and temperature, to be downloaded on recovery. The LISST (#104579) contains 2 MB of internal memory. The LISST-100 requires calibration before each deployment. For the calibration, a bucket sample was taken from the side of the vessel, and the LISST placed vertically in the bucket to sample during one burst before mooring deployment (i.e., for 20 minutes). After the LISST was removed from the sample, a 1-litre water sample from the bucket was filtered, and the filter paper weighed on return to the lab to establish the suspended sediment concentration of the bucket sample for calibration of the LISST recorded value. On recovery of the instrument, the same procedure was carried out to recalibrate the instrument to determine the effects of biofouling on the instruments optics.
3. Two Benthos™ optical backscatter sensors (OBS), positioned to sample at 1.0 m (OBS #897) and 0.3 m (OBS #2167) above the bed. The OBS instruments measure suspended sediment concentration in the water column. These instruments were controlled by, and sampled at the same rate as, the Nortek Vector. The OBS instruments also require calibration before each deployment. The calibration was carried out using the same procedure as that specified for the LISST-100. Once again, the same procedure was carried out on recovery of the instruments for recalibration so that the effects of biofouling can be quantified.
4. A Seabird Electronics (SBE™) Conductivity, Temperature and Depth sensor (CTD #1620) positioned to sample at 0.3 m above the bed. The CTD was programmed to be powered by and sample at the same rate as the LISST-100. Temperature and conductivity were logged to the LISST internal memory to be downloaded on recovery.



Photographs of the BRUCE mooring and associated instrumentation are presented in [Appendix C](#).

### 3.1.2. CSIRO Oceanographic Moorings

CSIRO mooring 1 (CSIRO-1) was deployed in 10.5 m water depth on the seabed adjacent to Orman Reefs at location  $-9^{\circ} 47.722' \text{ S}$ ,  $142^{\circ} 26.732' \text{ E}$ . Bottom sediment at the site was composed of poorly-sorted calcareous muddy medium sand, with a mean grain size of  $325 \mu\text{m}$  (3GR01). The mooring was deployed at 05:36 28/03/2004 UTC. The aim of the deployment was to determine the hydrography of water near to a site of high seagrass abundance. CSIRO-1 contained a Seabird Electronics SBE<sup>TM</sup> 19 Multi-sensor (#19P34180-4533) and fluorometer that measured conductivity, temperature, dissolved oxygen, light (Photosynthetically Active Radiation - PAR), pressure, fluorescence and turbidity. The instrument was programmed to pump water through the dissolved oxygen sensor for 20 s for each sample, and each parameter was sampled every 10 minutes. The wiper on the fluorometer could not be programmed to clean the sensor and the mooring was deployed with the wiper remaining permanently open so that the sensor was open to the influence of biofouling.

CSIRO Mooring 2 (CSIRO-2) and CSIRO Mooring 3 (CSIRO-3) also contained SBE-19 multi-sensors (serial numbers 4535 and 4537, respectively). Additionally, CSIRO-2 and CSIRO-3 each contained an RD Instruments Workhorse Sentinel<sup>TM</sup> 600kHz Acoustic Doppler Current Profiler (ADCP; #2424 and #2388, respectively). The ADCP's were both programmed to sample in "High Resolution Mode 8" to obtain a profile of the current ranging from 1.2 m above the seabed to near the water surface. Each measurement was spaced at 0.25 m intervals in the water column and recorded 10 minute averages of the currents. CSIRO-3 also contained an RBR<sup>TM</sup> XR-240-TG Pressure sensor (#010096) which recorded pressure every 5 minutes.

CSIRO mooring 2 (CSIRO-2) was deployed in Area B. The mooring was located on an area of hard-ground north of the sandwaves in 10.8 m water depth at location  $-9^{\circ} 35.513' \text{ S}$ ,  $142^{\circ} 20.975' \text{ E}$ . The mooring was deployed at 02:52 29/03/2004 UTC. The aim of the deployment was to determine the hydrography and ocean currents and sediment transport rates in a region of no seagrass cover.

CSIRO mooring 3 (CSIRO-3) was deployed in Area A. The mooring was located on an area of mobile sand separating two algal reefs in 9.1 m water depth at location  $-9^{\circ} 34.385' \text{ S}$ ,  $142^{\circ} 13.410' \text{ E}$ . Sediment collected at the deployment site comprised a poorly-sorted calcareous muddy, coarse sand and gravel with a mean grain size of  $774 \mu\text{m}$  (15GR14). The mooring was deployed at 01:32 30/03/2004 UTC. The aim of the deployment was to determine the hydrography and ocean currents and sediment transport rates in a region containing seagrasses. This mooring was recovered at 21:23 15/04/2004 UTC and some data were retrieved. Data were not downloaded from the SBE-19 Multi-sensor as no external power supply was aboard the RV *James Kirby*, and we did not wish to drain battery power. The mooring was then redeployed at 23:17 15/04/2004 UTC in 7.3 m water depth at location  $-9^{\circ} 34.385' \text{ S}$ ,  $142^{\circ} 13.429' \text{ E}$ .

Photographs of the CSIRO moorings and associated instrumentation are presented in [Appendix D](#).

## 3.2. DATA PROCESSING AND ANALYSIS

Data were downloaded from the instruments and converted to a readable format. The data were then carefully checked for indications of instrument malfunctions, which were edited out. Also, the beginning and end of each data series were truncated and outliers deleted. Short data gaps were filled with standard “NaN” values, where applicable. The data were carefully checked at each stage of processing. After editing, the data file includes observations recorded at the sampling interval for each instrument (10 minutes), and a low-pass filtered data file created from these which contains data that has had all fluctuations of periods less than 33 hours removed. The low-pass filtered data were then sub-sampled every 6 hours.

### 3.2.1. Geoscience Australia Oceanographic Mooring (BRUCE)

On recovery of the BRUCE mooring, it was found that salt-water had penetrated the housing of the current meter, and no data from the BRUCE mooring was recorded. Additional details of the problems encountered on communication and data download from BRUCE are presented in [Appendix E](#).

### 3.2.2. CSIRO Oceanographic Moorings

#### 3.2.2.1. SBE-19 Multi-sensors

For data stored on the SBE-19 Multi-sensors, proprietary SEASOFT™ software (Sea-Bird Electronics, Inc. [www.seabird.com](http://www.seabird.com)) was used to read the data into a file on a PC, convert the data to calibrated oceanographic units, and write the data to ASCII files. All editing, and filtering of the data was undertaken using MATLAB®. Time-series records of the variables recorded by the Multi-sensors, including the 10 minute averaged and low-pass filtered data, are presented to obtain an overview of the background oceanographic conditions at each site. Parameters recorded by the SBE-19 Multi-sensors include: Time; Temperature (°C); Conductivity (mS cm<sup>-1</sup>); Oxygen (mg l<sup>-1</sup>); Pressure (db); Photosynthetically Active Radiation (PAR,  $\mu\text{E m}^{-2} \text{s}^{-1}$ ); Fluorescence (mg m<sup>-3</sup>); and Turbidity (FTU).

#### 3.2.2.2. Pressure Sensors

A water depth record was recorded as pressure (in decibars) by the SBE-19 Multi-sensor on CSIRO-1, CSIRO-2 and CSIRO-3, as depth (in metres) on the RD Instruments ADCP on CSIRO-2 and CSIRO-3, and as pressure (in absolute decibars) on the RBR pressure sensor on CSIRO-3. In each case, the measurements have been converted to be relative to the seabed by adding the height of the sensor above the seabed (0.5 m for SBE-19 Multi-sensor data, 0.5 m for ADCP data and 0.8 for RBR data). Also, because the RBR pressure sensor measures absolute decibars, a surface value of 10.2 decibars was first subtracted from the records on CSIRO-3 to obtain the true water depth. In addition, the clock on the RBR Pressure Sensor was set to Australian Eastern Daylight Savings Time (UTC+1100 hrs). In processing the data, the time was corrected to UTC.

Minimum, maximum, mean and standard deviations were calculated for each of the parameters recorded by the instruments on the three CSIRO moorings. Where appropriate, correlation statistics between pressure records were determined and where an offset in timing occurs between pressure records, one record (time-series 2) has been linearly interpolated in time to match that of the other time series (time-series 1).

A classical harmonic tidal analysis was then carried out using the T\_TIDE package in MATLAB® (Pawlowicz et al., 2002). To determine the nature of the tides at each mooring, the form ratio (F) was determined as follows:

$$F = (K1 + O1) / (M2 + S2) \quad (4)$$

where K1 is the lunisolar diurnal tidal constituent, O1 is the principal lunar diurnal constituent, M2 is the principal lunar semidiurnal constituent, and S2 is the principal solar semidiurnal constituent. F is a measure of the tidal signature based on the relative magnitudes of their main diurnal and semi-diurnal constituents (Pond & Pickard, 2000) such that:

- F = 0 to 0.25 = semi-diurnal tides;
- F = 0.25 to 1.5 = mixed, mainly semi-diurnal tides;
- F = 1.5 to 3.0 = mixed, mainly diurnal tides; and
- F > 3.0 = diurnal tides.

### 3.2.2.3. Acoustic Doppler Current Profilers

ADCP's were located on CSIRO-2 and CSIRO-3. The ADCP's were configured to record data in Earth coordinates. On recovery, the data were transferred to a PC using the RD Instruments ([www.rdinstruments.com](http://www.rdinstruments.com)) proprietary WinADCP software. Observations recorded as East, North, Up, Error and Depth were exported to MATLAB® format and software routines were used to check for data quality, flag bad values, and discard data in bins that were always beyond the water surface. Data were also eliminated where correlation (SNR) was <90%. Additionally, data was removed where errors in the observations were >10 cm s<sup>-1</sup> and if the bin depth was higher than the water level. At times of low tide, the side-beam reflection renders data collected in some of the near-surface bins invalid and these data must be interpreted with care. On occasion, the ADCP skips an ensemble record because the data is poor. Data have blank placeholders for the missing ensemble records.

The ADCP on CSIRO-3 was programmed to sample at different times between the first and second deployments. On the first deployment, the ADCP was set to record at 06, 16, 26, 36, 46, 56 minutes every hour. On the second deployment, the ADCP was set to record at 0, 10, 20, 30, 40, 50 minutes every hour. For consistency in processing, data from the second deployment were linearly interpolated to 06, 16, 26, 36, 46, 56 minutes every hour.

Because this study is mostly a study of seabed processes, processing and analysis of current meter data from the ADCP's has been limited to data obtained from the "bin" closest to the seabed. The first bin is 1.14 m above the sensor or 1.6 m above the seabed. To provide details of the vertical current profile through the water column, data from the bin just below the lowest tide (i.e., the highest bin with a continuous record) was also processed and analysed.

For both CSIRO-2 and CSIRO-3 the following analyses of the bottom and 'surface' currents were undertaken:

1. Progressive vector plots were created and the mean residual currents during the deployments were computed.
2. Time series plots were created, to provide an overview of the observations. The mean absolute current speeds were also determined.

3. Principal axes for both the 10 minute averaged processed data and the low-pass filtered data were computed. Major and minor axes, orientation, and ellipticity were computed from the east (u) and north (v) current components as follows:

$$\text{major axis} = [0.5 (UU + VV) + R] / n^{(1/2)} \quad (5)$$

$$\text{minor axis} = [0.5 (UU + VV) - R] / n^{(1/2)} \quad (6)$$

$$\text{orientation} = 90^\circ - 0.5 \tan^{-1} [2 UV / (UU - VV)] \quad (7)$$

$$\text{ellipticity} = 1 - (\text{minor axis} / \text{major axis}) \quad (8)$$

where  $UV = \sum(u * v) - n * U * V$ ,  $UU = \sum(u * u) - n * U * U$ ,  $VV = \sum(v * v) - n * V * V$ ,  $R = [(0.5 (UU - VV))^2 + (UV)^2]^{(1/2)}$  and  $U$  and  $V$  are the means of the east and north velocity components, respectively.  $\sum$  is the sum of the entire data set of  $n$  values. The orientation is measured clockwise from true north.  $0^\circ$  is true north and  $90^\circ$  is east.

4. Scatter plots of the 10 minute averaged processed data and the low-pass filtered data sub-sampled every 6 hours were also created to show the distribution of the current speed and direction for the period of deployment. Superimposed on the scatter plots are the mean vector current over the entire deployment, and the principal current axes, shown as an ellipse.

As well as these analyses a tidal analysis was undertaken on the current data to determine the tidal ellipses. First the mean values for the horizontal velocity time series (u, v) were removed from the time series of these components and then the amplitude and phase of each tidal constituent was computed for the u and v components separately using the T\_TIDE software in MATLAB® (Pawlowicz et al., 2000). For each tidal constituent, the fit amplitudes were then used to compute the tidal ellipse parameters using the 'Tidal\_Ellipse' software in MATLAB® (Xu, 2002). This analysis provides estimates of (1) the semi-major axis (or maximum current velocity); (2) the ellipse eccentricity (i.e., the ratio of semi-minor to semi-major axis) where a negative value indicates that the ellipse is traversed in a clockwise direction; (3) the ellipse inclination, or the angle between east (x-) and the semi-major axis; and (4) the phase, or the angle that the oppositely rotating circular components must traverse from their initial positions for them to meet.

### 3.3. RESULTS

Unfortunately, due to seawater penetrating the housing of the Nortek Vector Acoustic Doppler Velocimeter, no results are available from the BRUCE deployment ([Appendix E](#)).

CSIRO-1 commenced logging on the SBE-19 Multi-sensor at 07:20 28/03/2004 UTC (Julian Day 88.3058) and was recovered by CSIRO scientists at the end of their survey aboard the RV *James Kirby* immediately following the present survey, and no details of the recovery were supplied to Geoscience Australia. The data indicate that the Multi-sensor continued to log until a CSIRO technician interrogated the instrument in Townsville so that the last recording on the instrument occurs at 05:00 31/05/2004 GMT. However, the pressure sensor record indicates that the final reading before the mooring was recovered occurred at 06:30 28/04/2004 UTC (Julian Day 119.2711), and so we have assumed that the instrument was recovered at 06:31 28/04/2004 UTC. The total record length is 30.97 days. An ASCII file containing data from the SBE-19 as downloaded directly from the instrument was transferred to Geoscience Australia from CSIRO Marine Research via FTP on 12/08/2004.

CSIRO-2 commenced logging of data on the SBE-19 Multi-sensor at 04:10 29/03/2004 UTC (Julian Day 89.1808) and on the ADCP at 01:57 29/03/2004 UTC. The mooring was deployed at 02:52 29/03/2004 UTC (Julian Day 89.1194). The first hour of the ADCP record has thus been removed. The mooring was recovered by CSIRO scientists at the end of their survey aboard the RV *James Kirby* immediately following the present survey, and no details of the recovery were supplied to Geoscience Australia. Both instruments continued to log until a CSIRO technician interrogated them in Townsville so that the last recording on the instrument occurs at 04:57 31/05/2004 UTC on the ADCP. However, the pressure sensor record on the ADCP indicates that the final reading before the mooring was recovered occurred at 04:27 29/04/2004 UTC. We have assumed that the instrument was recovered at 04:28 28/04/2004 UTC (Julian Day 119.1861). The total record length is 31.06 days. An ASCII file containing the SBE-19 Multi-sensor data and a Binary file containing the ADCP data as downloaded directly from the instruments were transferred to Geoscience Australia from CSIRO Marine Research via FTP on 12/08/2004.

Despite CSIRO-3 having been recovered and re-deployed during the survey, the position of the instrument has been assumed to be the same, and the time-series files from each instrument have been concatenated. CSIRO-3 commenced logging data on the SBE-19 Multi-sensor at 08:10 29/03/2004 UTC and on the ADCP at 03:56 29/03/2004 UTC. The mooring was deployed at 01:32 30/03/2004 UTC (Julian Day 90.0639). The first 2.5 hours of observations collected while the mooring was on the deck were removed. Also, the pressure record on the SBE-19 Multi-sensor indicates that CSIRO-3 was out of the water (while data was downloaded) from 21:30:23–23:20:23 15/04/2004 UTC (JD 106.8961–106.9725). All records from all instruments recorded during this period have been removed. The mooring was finally recovered by CSIRO scientists at the end of their survey aboard the RV *James Kirby* immediately following the present survey, and no details of the recovery were supplied to Geoscience Australia. The instruments continued to log until a CSIRO technician interrogated them in Townsville so that the last recording on the instrument occurs at 04:00 31/05/2004 UTC on the ADCP. However, the pressure sensor record indicates that the final reading before the mooring was recovered occurred at 03:30 29/04/2004 UTC. From this, we have assumed that the instrument was recovered at 04:31 29/04/2004 UTC (Julian Day 120.1889). The total record length is 31.08 days. An ASCII file containing SBE-19 Multi-sensor data, an ASCII file containing the RBR-pressure data, and a Binary file containing the ADCP data, as downloaded directly from the instruments were transferred to Geoscience Australia from CSIRO via FTP on 12/08/04.

### 3.3.1. SBE-19 Multi-sensor Data

Data collected by the SBE-19 Multi-sensors provide information about the background oceanographic conditions and valuable supporting information for sediment transport studies. For example, the light (PAR) readings could be inversely correlated with suspended sediment concentrations. As such, basic statistics for each parameter collected by the SBE-19 Multi-sensors were calculated for each of the CSIRO moorings (Table 3.1a-c).

CSIRO-1 is the deepest of the three moorings, deployed to the east of the Orman Reefs. This is evident by the largest mean pressure of 11.2663 db (Table 3.1a), and also by the lowest light levels being recorded at this site (Mean PAR of  $17.9828 \mu\text{E m}^{-2} \text{ s}^{-1}$ ). Mean Salinity at CSIRO-1 (32.4 psu) is more than 0.5 psu greater than that at CSIRO-2 and CSIRO-3, and experienced a noticeable increase of approximately 3 psu between JD 102 and JD 108 (Figs.

3.2d, 3.3d). Additionally, fluorescence and turbidity levels are noticeably lower at CSIRO-1 than the other mooring sites. All properties indicate relatively strong semi-diurnal variation in response to the tides in the region (Fig. 3.2).

Table 3.1. Basic statistics for parameters recorded by the SBE-19 Multi-sensor on the CSIRO oceanographic moorings.

a) SBE-19 Multi-sensor on CSIRO-1				
Parameter	Minimum	Mean	Maximum	Std Dev.
Temperature (°C)	27.7914	28.7045	29.8322	0.4491
PAR ( $\mu\text{E m}^{-2} \text{s}^{-1}$ )	0.5030	17.9828	219.9700	30.7836
Pressure (db)	9.6690	11.2663	12.9900	0.7711
Salinity (PSU)	30.7699	32.4001	34.2268	1.3584
Oxygen ( $\text{mg l}^{-1}$ )	5.4758	6.1318	6.7031	0.1546
Fluorescence ( $\text{mg m}^{-3}$ )	0	0.3178	0.8407	0.1508
Turbidity (FTU)	0.4461	3.7140	17.7477	2.0625
b) SBE-19 Multi-sensor on CSIRO-2				
Parameter	Minimum	Mean	Maximum	Std Dev.
Temp (°C)	27.8260	28.7814	30.1483	0.4710
PAR ( $\mu\text{E m}^{-2} \text{s}^{-1}$ )	0.5290	9.1725	248.6700	24.8509
Pressure (db)	7.7660	9.3677	10.8350	0.6875
Salinity (PSU)	30.1783	31.8353	33.7407	1.2206
Oxygen ( $\text{mg l}^{-1}$ )	5.6754	6.0442	7.1036	0.1420
Fluorescence ( $\text{mg m}^{-3}$ )	0	0.7617	3.6052	0.4982
Turbidity (FTU)	1.0376	8.5808	31.3411	6.1115
c) SBE-19 Multi-sensor on CSIRO-3				
Parameter	Minimum	Mean	Maximum	Std Dev.
Temp (°C)	27.5931	28.6833	29.9064	0.5049
PAR ( $\mu\text{E m}^{-2} \text{s}^{-1}$ )	0.3000	136.7	3198.8	372.6
Pressure (db)	5.6460	7.3561	8.8920	0.6528
Salinity (PSU)	30.3096	31.8119	33.7536	1.1834
Oxygen ( $\text{mg l}^{-1}$ )	5.6594	6.1269	6.7112	0.1910
Fluorescence ( $\text{mg m}^{-3}$ )	0	0.8778	3.2862	0.6317
Turbidity (FTU)	0	5.7305	34.9178	6.5191

CSIRO-2, positioned between two large sand-ribbons in area B, experienced the most turbid conditions of the three moorings. Interestingly, turbidity peaks, reaching a maximum value of 31.3411 FTU, are experienced during periods when the tidal range is near to its smallest, around Julian Days 97 and 109 (Fig. 3.4c, g), not when the tidal range is largest during JD 92 and 104. During the period of smallest tidal range, no diurnal inequality is observed in the tidal record, and the daily vertical tidal water-level variation during this



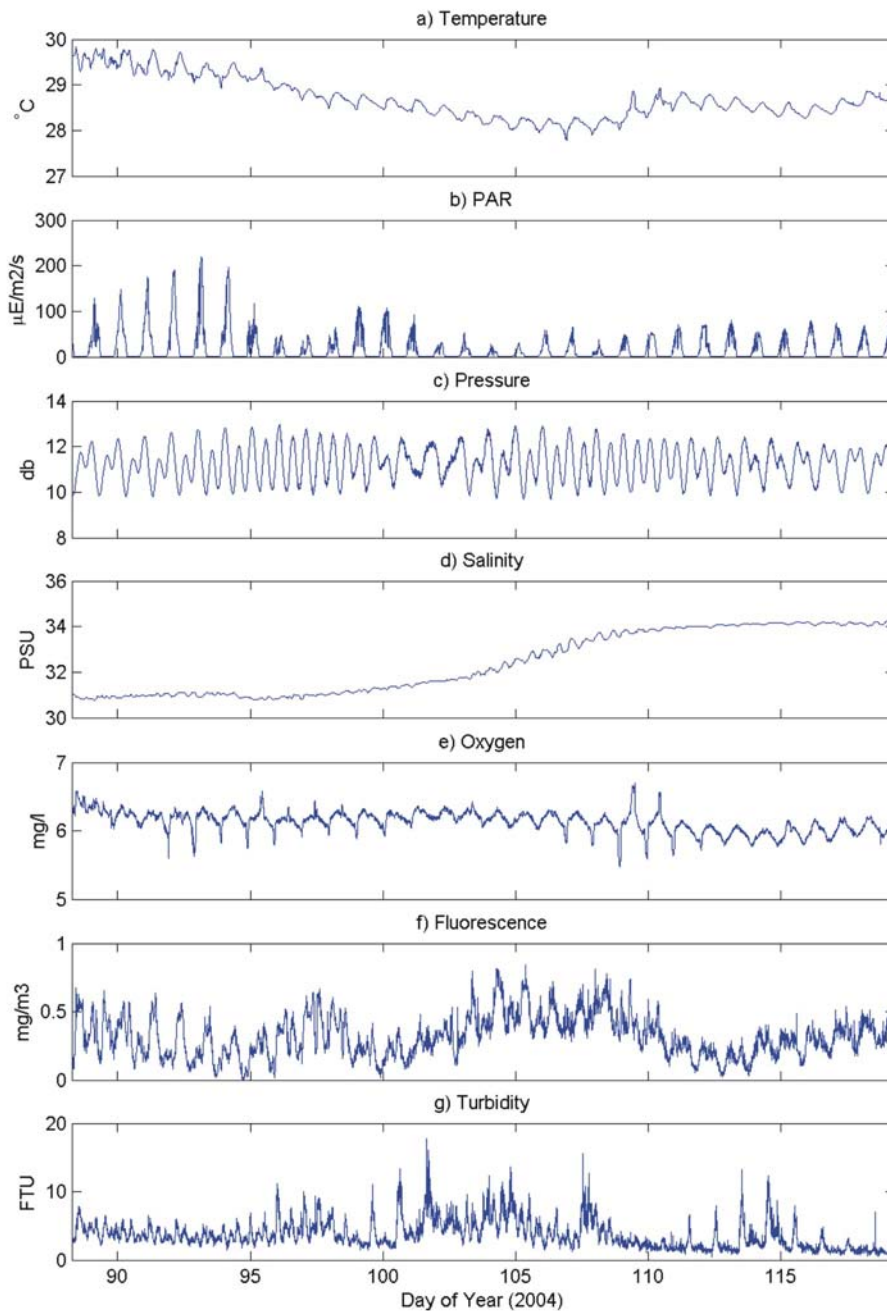


Figure 3.2. CSIRO-1. Time-series plots of variables recorded every 10 minutes by SBE-19. a) Temperature; b) Photosynthetically Active Radiation; c) Pressure; d) Salinity; e) Oxygen; f) Fluorescence; g) Turbidity.

period is larger (Fig. 3.4c). The turbidity peaks are associated with peaks in Fluorescence (Fig. 3.4f), and decreased light levels reaching to PAR sensor (Fig. 3.4b). These low frequency events are more clearly seen in the low-pass filtered data (Fig. 3.5b, f, g). During the period of increased turbidity around Julian Day 97, no light is recorded near to the sea-bed less than 8 m from the sea surface (Fig. 3.4b). All properties indicate relatively strong semi-diurnal variation in response to the tides in the region (Fig. 3.4).

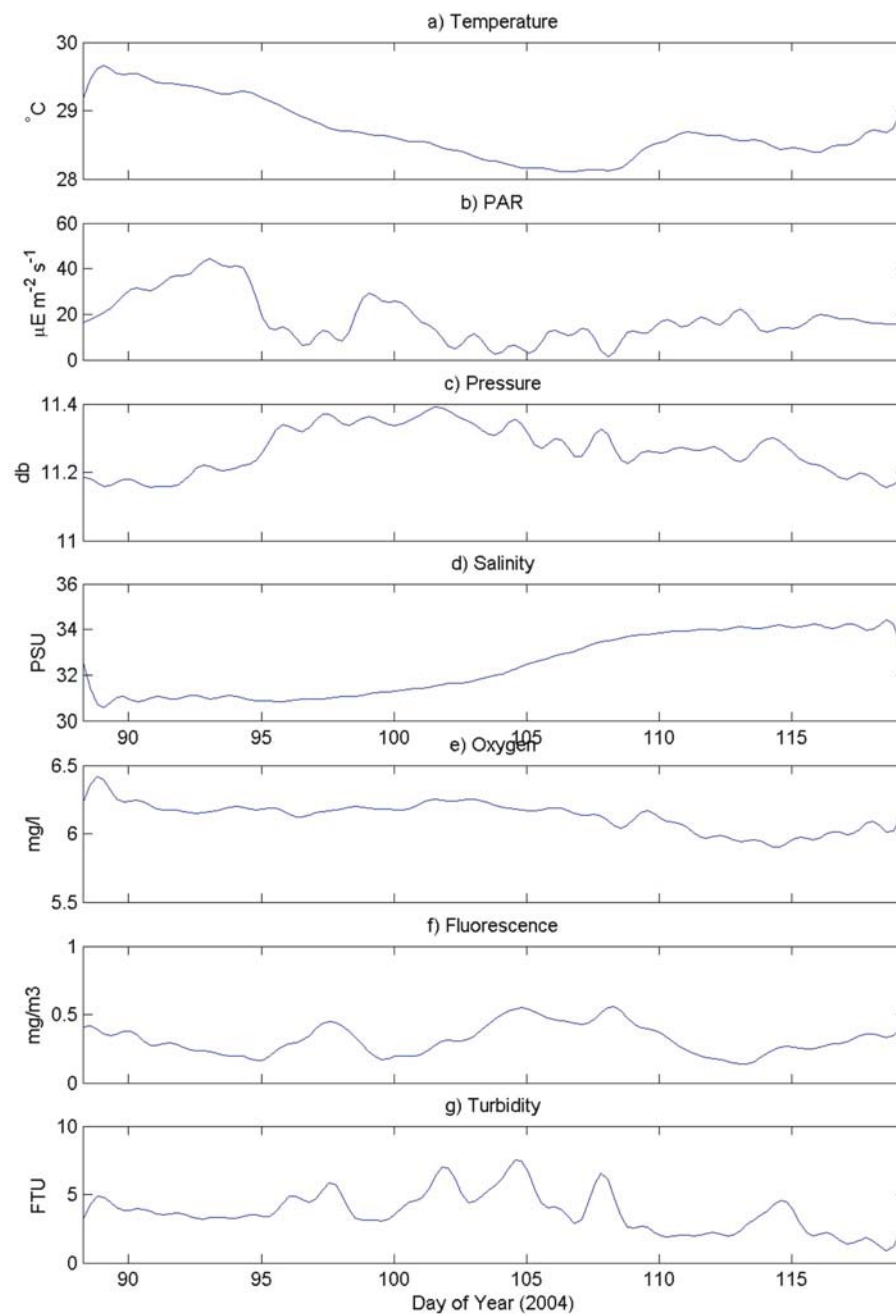


Figure 3.3. CSIRO-1. 30-hour low pass filtered time-series plots of variables recorded by SBE-19. a) Temperature; b) Photosynthetically Active Radiation, c) Pressure; d) Salinity; e) Oxygen; f) Fluorescence; g) Turbidity.

CSIRO-3, located in Area A where seagrass is observed, recorded the highest mean fluorescence level ( $0.8778 \text{ mg m}^{-3}$ ; Table 3.1-c). This mooring is the shallowest of the three moorings (mean pressure is  $7.3561 \text{ db}$ ), and consequently experiences the highest PAR levels (mean PAR is  $136.7 \mu\text{E m}^{-2} \text{s}^{-1}$  – an order of magnitude larger than mean PAR levels at CSIRO-1 and CSIRO-2). However, peaks in turbidity are experienced around Julian Days 97 and 107, during which time PAR levels at the sensor are significantly reduced (PAR is  $0 \mu\text{E}$



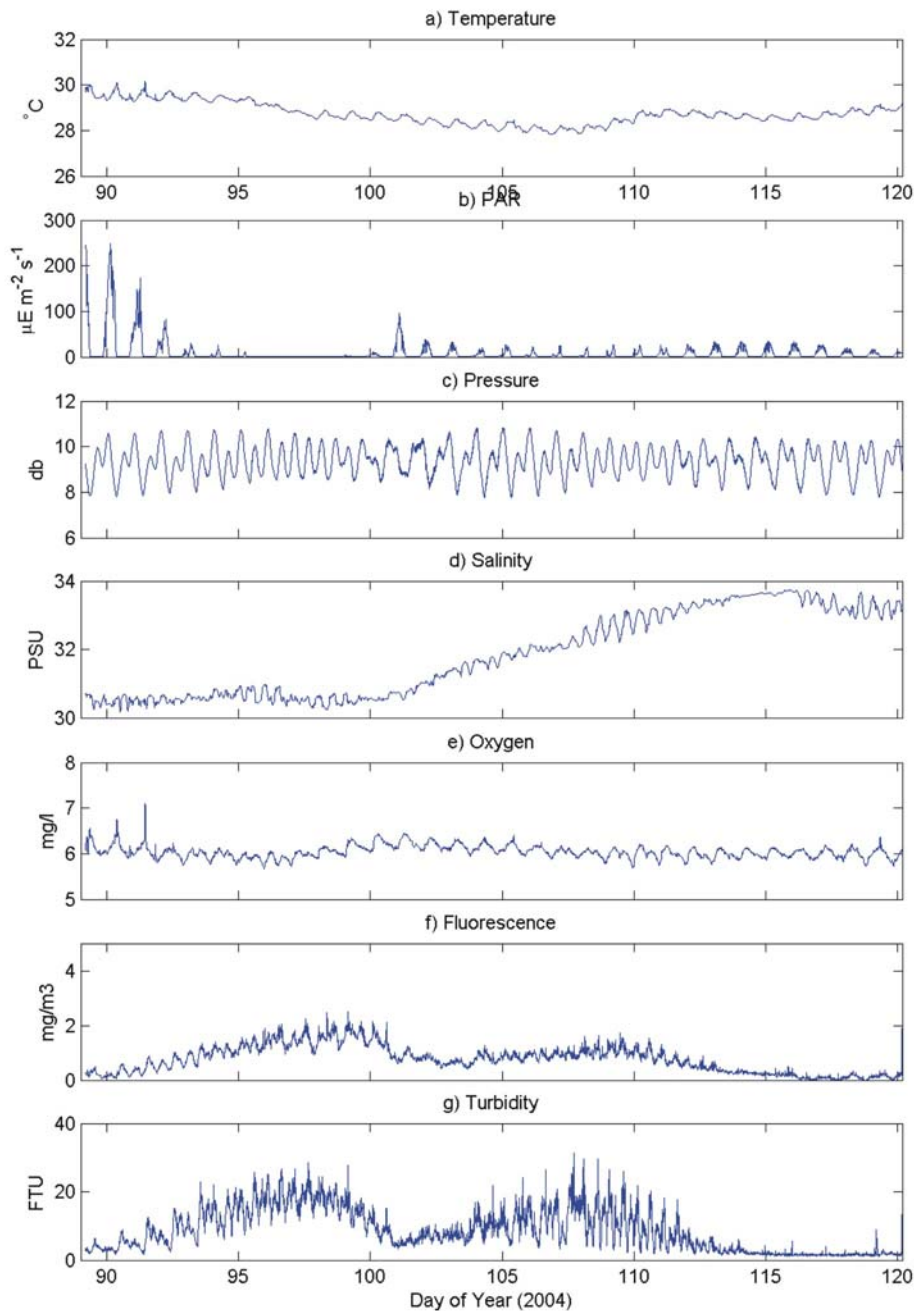


Figure 3.4. CSIRO-2. Time-series plots of variables recorded every 10 minutes by SBE-19. a) Temperature; b) Photosynthetically Active Radiation; c) Pressure; d) Salinity; e) Oxygen; f) Fluorescence; g) Turbidity.

$\text{m}^{-2} \text{s}^{-1}$  during Julian Day 97 in less 7 m depth below the sea-surface; Fig. 3.7b). During these periods, tidal range is almost at its minimum with low water of  $\sim 6.8$  m recorded, and high water of  $\sim 8.0$  m being recorded (Fig. 3.7c). During periods of maximum tidal range, a strong diurnal inequality is observed, and daily water levels range from  $\sim 5.8$  m to  $\sim 9.0$  m. All properties indicate relatively strong semi-diurnal variation in response to the tides in the region (Fig. 3.6).

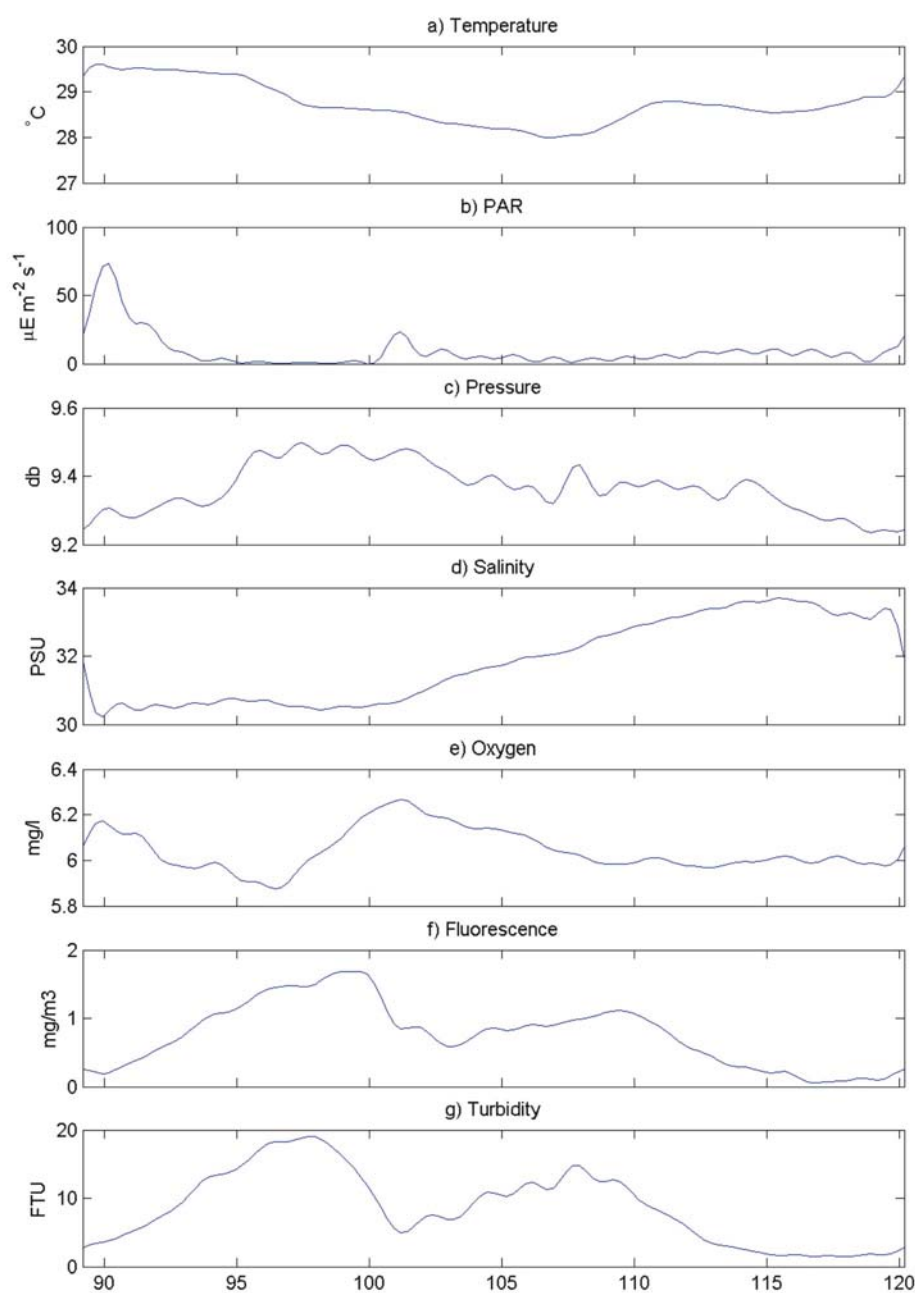


Figure 3.5. CSIRO-2. 30-hour low pass filtered time-series plots of variables recorded by SBE-19. a) Temperature; b) Photosynthetically Active Radiation; c) Pressure; d) Salinity; e) Oxygen; f) Fluorescence; g) Turbidity.

### 3.3.2. Tidal Statistics

#### 3.3.2.1. Sea level

A harmonic analysis of the pressure record taken from the SBE-19 multi-sensor on CSIRO-1 was carried out. The amplitude and phase of the four main constituents are presented in [Table 3.2](#).

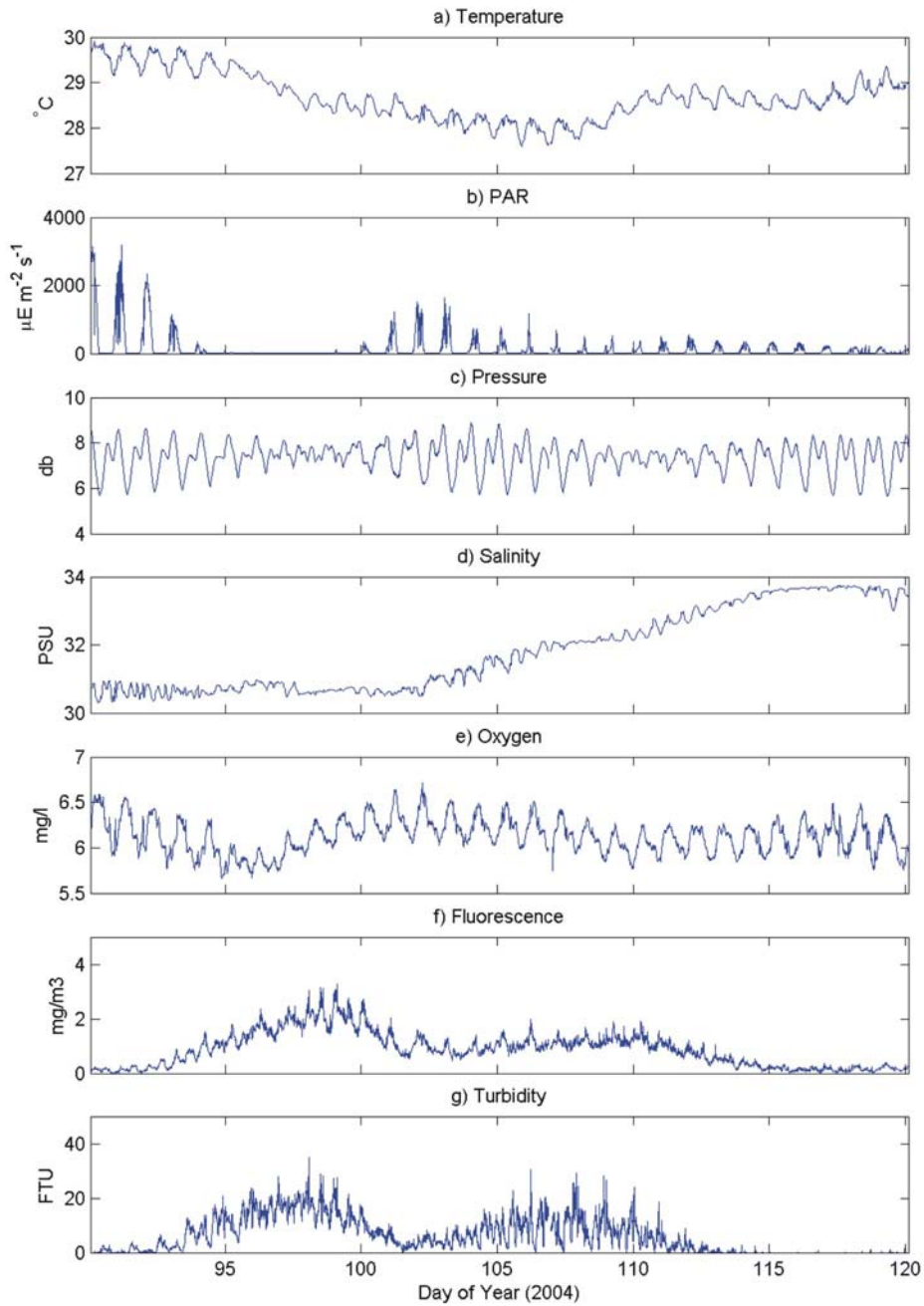


Figure 3.6. CSIRO-3. Time-series plots of variables recorded every 10 minutes by SBE-19. a) Temperature; b) Photosynthetically Active Radiation, c) Pressure; d) Salinity; e) Oxygen; f) Fluorescence; g) Turbidity.

The form ratio (F) calculated at CSIRO-1 is 0.54, indicating that the tides are mixed, semi-diurnal. Significant tidal constituents calculated within the analysis, where the amplitude of a tidal constituent is greater than the error in amplitude for that constituent, are principally in the diurnal and semi-diurnal bands ( $\sim 0.04$  and  $\sim 0.08$  cycles per hour, respectively; Fig. 3.8b). Some higher frequency constituents are also significant (Fig. 3.8b). The tidal phase

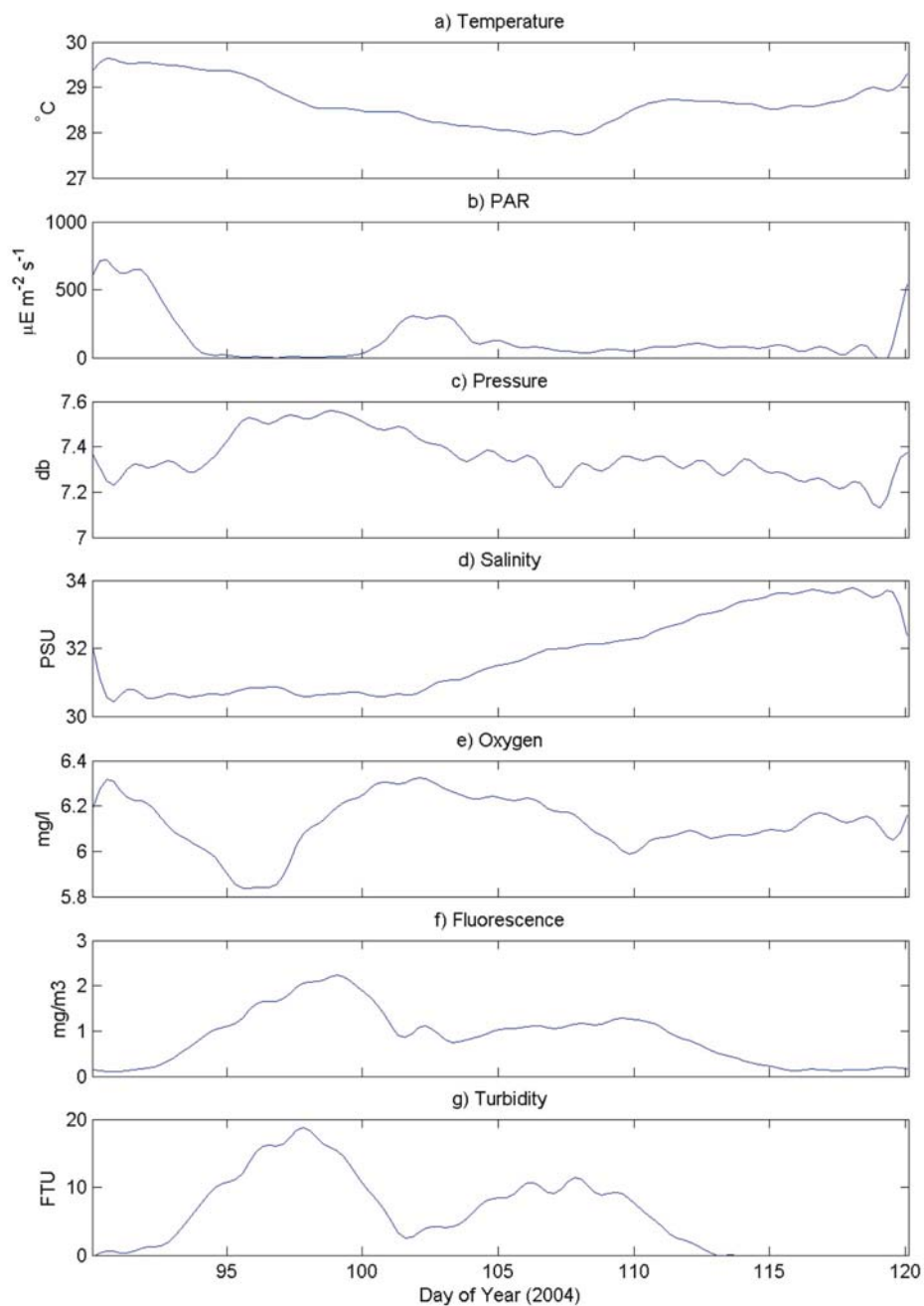


Figure 3.7. CSIRO-3. 30-hour low pass filtered time-series plots of variables recorded by SBE-19. a) Temperature; b) Photosynthetically Active Radiation; c) Pressure; d) Salinity; e) Oxygen; f) Fluorescence; g) Turbidity.

record shows that the significant constituents generally have small phase errors (Fig. 3.8c). The residual time-series after removal of the tidal signal has low amplitudes, indicating that the sea surface signal is almost entirely tidal (Fig. 3.8a), and this is also represented by the energy (Fig. 3.8d), where non-tidal energy (red-line) is relatively low in relation to the tidal energy (blue-line).

Table 3.2. Classical harmonic analysis of tidal constituents for data collected by the SBE-19 Multi-sensor on CSIRO-1. Phase is with respect to Universal Time Constant (UTC).

Tide	Frequency (cycles per hour)	Amplitude (m)	Amplitude Error (m)	Phase (degrees)	Phase Error (degrees)
O1	0.0387	0.2583	0.018	15.47	3.13
K1	0.0417	0.4275	0.018	56.07	2.25
M2	0.0805	0.5084	0.068	87.60	8.39
S2	0.0833	0.7528	0.075	49.56	6.18

Sea-level records are available from both the SBE-19 Multi-sensor and the ADCP on CSIRO-2. A linear regression analysis was carried out between the Multi-sensor data and the ADCP data (Table 3.3). A slope of <1 indicates that the ADCP data overestimates the Multi-sensor data. Table 3.3 shows correlation slope of 1.0548, indicating good agreement of tidal range between the two records, however the relatively low correlation coefficient ( $R^2$ ) of 0.8077 indicates that there may be some phase shift between the two sea-level records.

Table 3.3. Regression statistics between pressure records at CSIRO-2.

Time-series 1 (Y)	Time-series 2 (X)	$R^2$	Slope
SBE-19 Multi-sensor	ADCP	0.8077	1.0548

Classical harmonic tidal analyses were then undertaken on both of the sea-level records from CSIRO-2 (Table 3.4a, b). The amplitude and phase of the four main constituents for each record are presented in Table 3.4a-b respectively.

Table 3.4. Classical harmonic analysis of tidal constituents for data collected by a) the SBE-19 Multi-sensor and b) the ADCP Current Meter on CSIRO-2. Phase is with respect to Universal Time Constant (UTC).

a) SBE-19 Multi-sensor					
Tide	Frequency (cycles per hour)	Amplitude (m)	Amplitude Error (m)	Phase (degrees)	Phase Error (degrees)
O1	0.0387	0.2940	0.017	16.35	3.49
K1	0.0417	0.4648	0.020	63.70	2.25
M2	0.0805	0.2782	0.088	127.05	16.70
S2	0.0833	0.6348	0.076	69.31	7.49
b) ADCP Current Meter					
Tide	Frequency (cycles per hour)	Amplitude (m)	Amplitude Error (m)	Phase (degrees)	Phase Error (degrees)
O1	0.0387	0.3647	0.015	55.46	2.49
K1	0.0417	0.5278	0.013	86.77	1.51
M2	0.0805	0.2240	0.053	196.03	13.22
S2	0.0833	0.4875	0.060	95.90	6.15

The form ratio (F) is 0.8311 from the SBE-19 Multi-sensor data and 1.25 from the ADCP data. The results of the analyses indicate that the diurnal constituents are smaller for the SBE-19

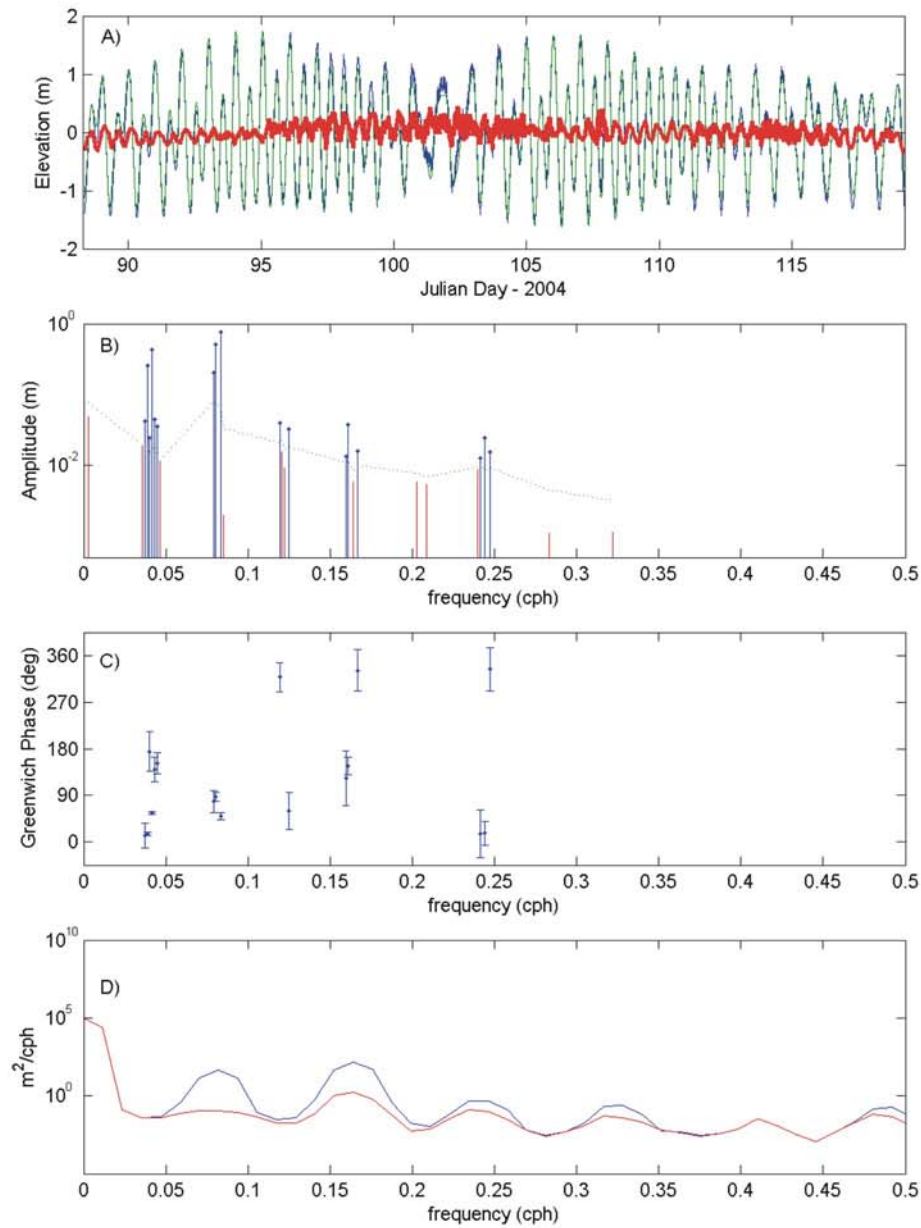


Figure 3.8. Results of classical harmonic analysis of pressure data from CSIRO-1. a) Blue line is Raw Time Series referenced to the mean level in the record, Green line is Tidal prediction from analysis referenced to the mean, Red line is residual time series after removal of the tidal signal; b) Amplitude of all analysed components with 95% significance level (green dashed line). Note frequency dependence. Significant constituents (amp > amp\_err) are marked with a solid circle; c) Phase of significant constituents with 95% confidence interval; d) Spectral Estimates before and after removal of tidal energy. Blue-line is energy of original time-series, red-line is non-tidal energy.

Multi-sensor data than the ADCP data. However, despite these differences, both records indicate the tides are mixed, semi-diurnal. The significant constituents are principally in the diurnal and semi-diurnal bands ( $\sim 0.04$  and  $\sim 0.08$  cycles per hour, respectively; Fig. 3.9b).



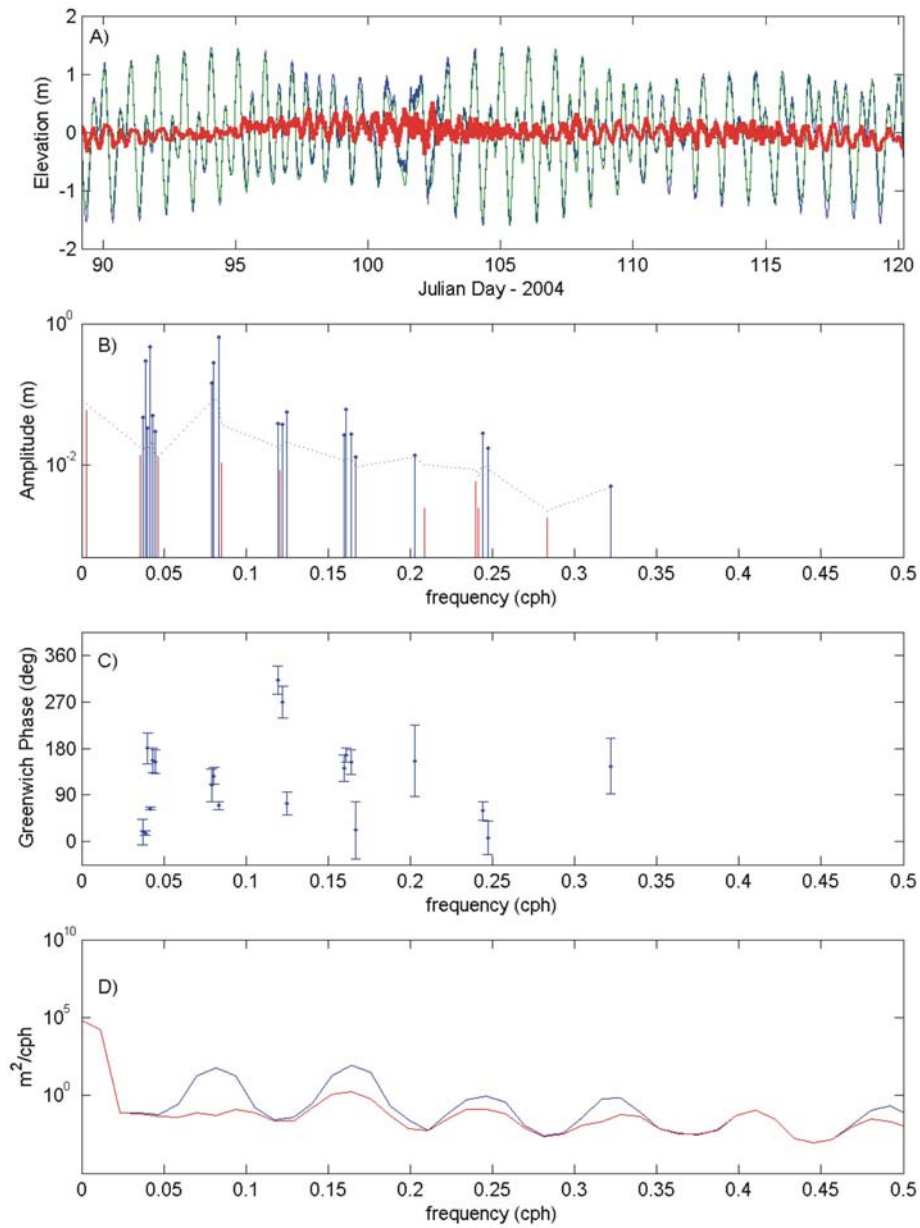


Figure 3.9. As for Figure 3.8, but for CSIRO-3.

Some higher frequency constituents are also significant (Fig. 3.9b). The tidal phase record shows that the significant constituents generally have small phase errors (Fig. 3.9c). The residual time-series after removal of the tidal signal has low amplitudes, indicating that the sea surface signal is mostly tidal (Fig. 3.9a). This is also represented by the energy (Fig. 3.9d), where non-tidal energy (red-line) is relatively low in relation to the tidal energy (blue-line).

Sea-level records are available from the RBR pressure sensor, the SBE-19 Multi-sensor and the ADCP on CSIRO-3. A linear regression analysis was carried out between the RBR data and the ADCP data, and the RBR data and the SBE-19 Multi-sensor data (Table 3.5). A slope of <1 indicates that time-series 2 overestimates time-series 1 in both cases. Good agreement is observed between the 3 sea-level records.

Table 3.5. Regression statistics between pressure records at CSIRO-3.

Time-series 1 (Y)	Time-series 2 (X)	R <sup>2</sup>	Slope
RBR	ADCP	0.9960	0.988
RBR	SBE-19 Multi-sensor	0.9982	0.999

Classical harmonic tidal analyses were then undertaken on all three of the sea-level records from CSIRO-3 (Table 3.6a-c). The amplitude and phase of the four main constituents for each record are presented in Table 3.6a-c, respectively.

Table 3.6. Classical harmonic analysis of tidal constituents for data collected by a) the RBR pressure sensor, b) SBE-19 Multi-sensor, and c) ADCP Current Meter on CSIRO-3. Phase is with respect to Universal Time Constant (UTC).

a) RBR Pressure Sensor					
Tide	Frequency (cycles per hour)	Amplitude (m)	Amplitude Error (m)	Phase (degrees)	Phase Error (degrees)
O1	0.0387	0.3362	0.022	9.80	4.05
K1	0.0417	0.5125	0.026	64.51	2.71
M2	0.0805	0.3288	0.068	208.48	12.57
S2	0.0833	0.4161	0.073	79.30	10.34
b) SBE-19 Multi-sensor					
Tide	Frequency (cycles per hour)	Amplitude (m)	Amplitude Error (m)	Phase (degrees)	Phase Error (degrees)
O1	0.0387	0.3359	0.020	10.25	3.84
K1	0.0417	0.5112	0.025	64.94	2.60
M2	0.0805	0.3304	0.078	209.41	12.30
S2	0.0833	0.4140	0.069	80.13	10.83
c) ADCP Current Meter					
Tide	Frequency (cycles per hour)	Amplitude (m)	Amplitude Error (m)	Phase (degrees)	Phase Error (degrees)
O1	0.0387	0.4666	0.032	37.41	4.16
K1	0.0417	0.6269	0.031	73.68	2.63
M2	0.0805	0.3150	0.085	252.47	14.78
S2	0.0833	0.4171	0.075	79.57	9.99

The form ratio (F) is 1.14 from the RBR Pressure Sensor data, 1.14 from the SBE-19 Multi-sensor data, and 1.49 from ADCP Current Meter data. The ADCP record indicates the diurnal constituents are greater than that from the other two sea-level records (and suggests the record could almost be classified mixed, mainly diurnal). However, all three sea-level records indicate the tides are mixed, semi-diurnal. The analyses indicate that the significant constituents are principally in the diurnal and semi-diurnal bands (~0.04 and ~0.08 cycles per hour, respectively; Fig. 3.10b). Some higher frequency constituents are also significant (Fig. 3.10b). The tidal phase shows that the significant constituents generally have small phase

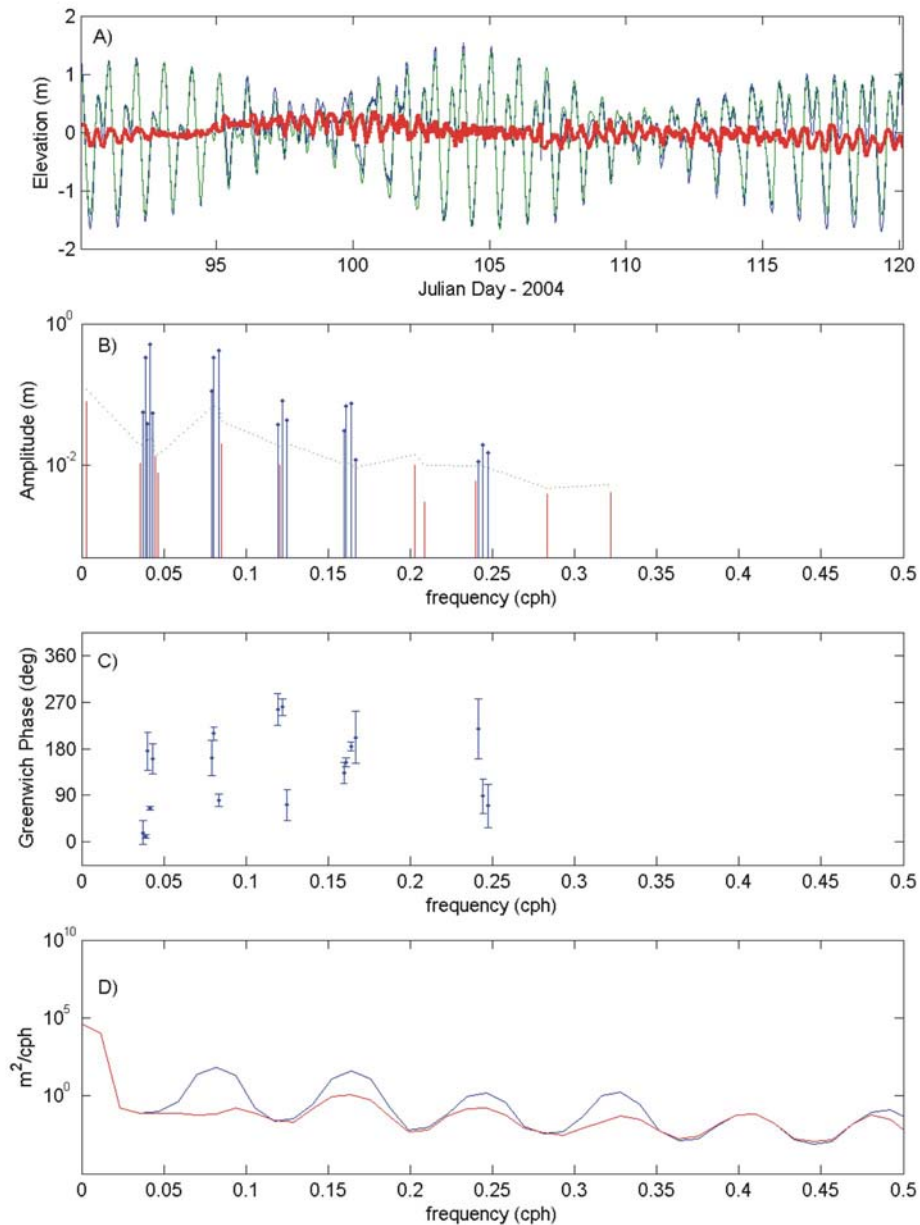


Figure 3.10. As for Figure 3.8, but for CSIRO-3.

errors (Fig. 3.10c). The residual time-series after removal of the tidal signal has low amplitudes, indicating that the sea surface signal is almost entirely tidal (Fig. 3.10a). This is also represented by the energy (Fig. 3.10d), where non-tidal energy (red-line) is relatively low in relation to the tidal energy (blue-line).

### 3.3.2.2. Shallow-water Tides

The sea-level record taken from CSIRO-3 indicates higher harmonic tides may be important. During the period JD 95-101, and JD 109-115, the sea-level record taken in Area A displays up to four high and low waters per day (Fig. 3.10), suggesting that the third and fourth diurnal tidal constituents are important in Area A. The tidal analysis carried out using the

T\_TIDE software (Pawlowicz et al., 2000) extracts the constituents of these higher level harmonics. Table 3.7 lists the significant (amplitude > amplitude error) third and fourth diurnal constituents recorded at each current meter mooring.

Table 3.7. Significant third and fourth diurnal tidal constituents as obtained from tidal analysis of pressure record at the CSIRO current meter moorings. A constituent is considered significant if the amplitude exceeds the amplitude error. Phase is with respect to Universal Time Constant (UTC).

a) CSIRO-1				
Tide	Amplitude (m)	Amplitude Error (m)	Phase (degrees)	Phase Error (degrees)
MO3	0.0448	0.019	314.31	29.51
MK3			Not Significant	
SK3	0.0355	0.023	65.42	36.40
MN4			Not Significant	
M4	0.0353	0.011	149.00	18.57
MS4			Not Significant	
S4	0.0161	0.010	331.10	36.25
b) CSIRO-2				
Tide	Amplitude (m)	Amplitude Error (m)	Phase (degrees)	Phase Error (degrees)
MO3	0.0434	0.022	308.18	28.63
MK3	0.0395	0.021	275.77	28.78
SK3	0.0607	0.023	78.82	22.30
MN4	0.0255	0.012	144.17	25.33
M4	0.0571	0.013	170.36	12.24
MS4	0.0264	0.012	154.56	24.48
S4			Not Significant	
c) CSIRO-3				
Tide	Amplitude (m)	Amplitude Error (m)	Phase (degrees)	Phase Error (degrees)
MO3	0.0424	0.023	251.24	32.26
MK3	0.0862	0.021	267.15	14.78
SK3	0.0473	0.022	76.39	29.94
MN4	0.0286	0.009	135.70	19.58
M4	0.0646	0.011	156.46	10.08
MS4	0.0722	0.009	185.21	7.61
S4			Not Significant	

Table 3.7 indicates that with progression westwards, from CSIRO-1 (Orman Reefs), to CSIRO-2 (Area B) to CSIRO-3 (Area A), the shallow water tides become increasingly important, supporting the higher frequency signal observed in the pressure record in Area A. Studies of higher order tidal constituents around the British Isles have concluded that the interaction of the M2 and M4 tides largely determine the direction of sand transport there

(Pingree and Griffiths, 1979). Similarly, these shallow water tides may be important in relation to sediment transport in Torres Strait, and these processes will be investigated in further detail

### 3.3.2.3. Currents

Tidal currents speeds measured at both the seabed and water surface were generally greater in vicinity of CSIRO-3 than CSIRO-2 over the deployment period (Table 3.8). At CSIRO-3, fastest currents near the bed attain  $>80 \text{ cm s}^{-1}$  and near the surface current speeds attain  $>130 \text{ cm s}^{-1}$ . At both moorings, the East component was slightly more dominant than the north component. At CSIRO-2, the minimum and maximum East currents are approximately twice as fast as the equivalent North currents near the bed. At the water surface, the maximum East current is  $>2.5$  times that of the equivalent North current. At CSIRO-3, the difference between the East and North components is not as pronounced. However, the mean North current is relative weak, being  $<1 \text{ cm s}^{-1}$ .

Table 3.8. Basic statistics from ADCP Current Meters on a) CSIRO-2 and b) CSIRO-3 in  $\text{cm s}^{-1}$ .

Bin Number	a) ADCP CSIRO-2		b) ADCP CSIRO-3	
	1 (1.6 m)	23 (7.4 m)	1 (1.6 m)	18 (6.1 m)
East (min.)	-76.200	-90.600	-71.3000	-121.4448
East (mean)	-3.981	-4.163	-8.2113	-10.6213
East (max.)	71.100	113.000	52.4973	91.0348
East (std dev.)	37.593	52.096	33.8399	38.8250
North (min.)	-31.700	-41.600	-49.7000	-92.2918
North (mean)	-2.666	-2.962	-0.0241	0.8588
North (max.)	33.300	43.000	47.5425	99.1710
North (std dev.)	11.362	15.686	22.4560	24.6702
Speed (min.)	16.329	23.960	15.8982	19.0177
Speed (mean)	36.032	49.107	38.2591	43.2136
Speed (max.)	76.578	116.005	80.4210	131.1863

At CSIRO-2, progressive vector plots of the tidal currents measured near the bed show that the net water displacement over the entire deployment was directed towards the SW and the total displacement was approximately 120 km (Fig. 3.11a). Progressive vector plots of the tidal currents measured at the surface also show that the net water displacement was directed towards the SW and that the total displacement was  $>136 \text{ km}$  (Fig. 3.11b).

At CSIRO-3, progressive vector plots of the tidal currents measured near the bed show that the net water displacement over the entire deployment was directed towards the west and the total displacement was approximately 210 km (Fig. 3.12a). Progressive vector plots of the tidal currents measured at the surface also show that the net water displacement was directed towards the west and that the total displacement was approximately 250 km (Fig. 3.12b).

At both CSIRO-2 and CSIRO-3 the magnitude of net displacement during the deployment period was not constant, with relatively larger displacements roughly occurring during Julian Days 99-104. This period also corresponds with the period of greater wind speeds recorded at Horn and Coconut Islands.



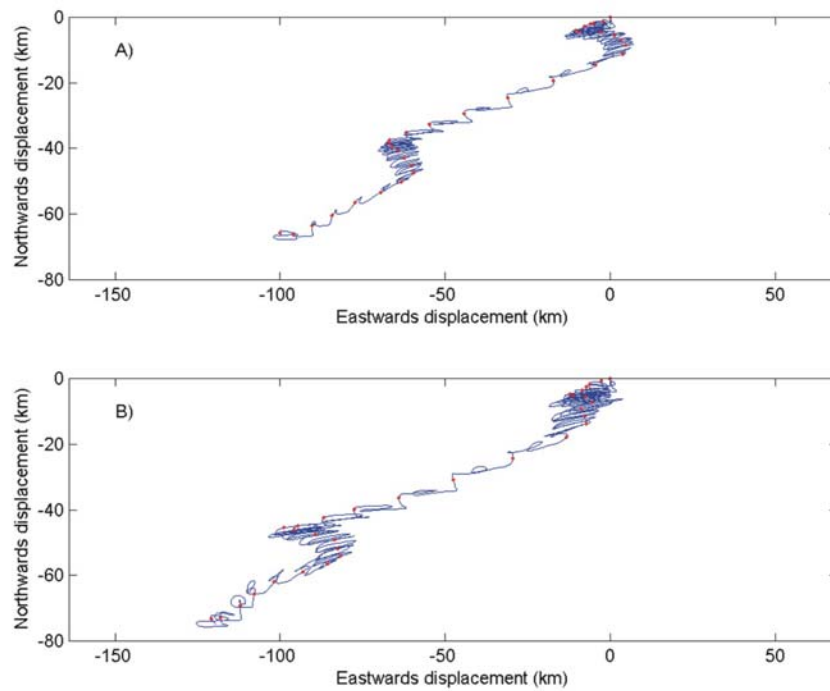


Figure 3.11. CSIRO-2 current meter progressive vector plot obtained from data recorded in a) bin 1 (1.6 m above seabed), and b) bin 23 (7.4 m above seabed). The origin of each plot corresponds to the location of the CSIRO-2 mooring. Dots indicate the beginning of each 24 hour period.

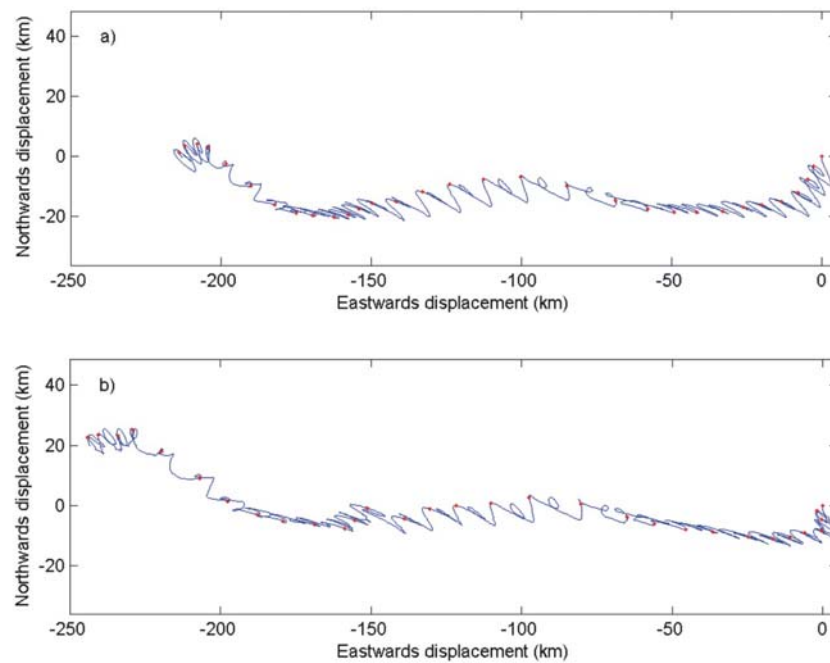


Figure 3.12. CSIRO-3 current meter progressive vector plot obtained from data recorded in a) bin 1 (1.6 m above seabed), and b) bin 18 (6.1 m above seabed). The origin of each plot corresponds to the location of the CSIRO-3 mooring. Dots indicate the beginning of each 24 hour period.

For CSIRO-2, time series from the 10 minute averaged data indicate that both near the bed (Fig. 3.13) and at the surface (Fig. 3.14), strongest currents occur around Julian Days 97 and 109 corresponding to the period of turbidity maxima and smallest tidal range, reported in Section 3.3.1. Despite the smaller absolute tidal range during this period, the diurnal equality results in a greater tidal excursion leading to the observed current speed maxima (Figs. 3.13, 3.14). It is also during this period that the low-pass filtered data indicate stronger non-tidal currents (reaching speeds greater than 15 (20)  $\text{cm s}^{-1}$  at the bed (surface); Figs. 3.15, 3.16). A similar event occurs after Julian Day 115, however the mooring was recovered before this event had finished.

For CSIRO-3, time series from the 10 minute averaged data indicate that both near the bed (Fig. 3.17) and at the surface (Fig. 3.18), a period of less strong currents occurs during Julian Days 101-102, and 114-115. Both of these periods correspond in time to the period of time 2-3 days after the period of smallest tidal range, but coincides with a period of strong diurnal inequality (Julian Days 98-99, and 110-111; Fig. 3.10a). The low-pass filtered data indicate more constant non-tidal currents than those observed at CSIRO-2, however the period of strongest non-tidal current is concurrent with those at CSIRO-2 during Julian Days 102-103 (Figs. 3.19, 3.20).

The principle axes analysis at CSIRO-2 reveals that the surface currents are approximately 1.4 times the magnitude of the currents at the sea-bed in all directions. Regardless, the currents are well aligned, with the scatter plot for both surface and bed currents (Fig. 3.21a, b) both indicating the major axis to be oriented to the south-west ( $-100^\circ\text{N}$ ; Table 3.8), and the ellipticity of each being  $\sim 0.75$  (i.e., the major axis is approximately 4 times larger than the minor axis of the ellipses; Table 3.8). The low-pass filtered ellipses (Fig. 3.21c, d) indicate similar alignment to the 10-minute averaged currents. This indicates that mean currents are aligned with the axis of the tidal currents, although they are not of smaller magnitude.

At CSIRO-3, the principal axes analyses revealed that the main currents are aligned to the NW ( $\sim 60^\circ\text{N}$ ; Table 3.9), which is the same as the axis of the channel separating two algal reefs in which the mooring was deployed. Currents at the surface and seabed have similar magnitudes and both have a major axis of  $\sim 40 \text{ cm s}^{-1}$ . Surface currents have slightly less ellipticity (0.6196) compared to the currents at the seabed, as shown by the surface current scatter plot (Fig. 3.22b), which shows greater spread in the data than the bed currents (Fig. 3.22a).

Table 3.9. Principal axes of currents for 10 minute averaged data and low pass filtered data for a) CSIRO-2 and b) CSIRO-3.

	a) CSIRO-2		b) CSIRO-3	
	Bin 1 (1.6 m)	Bin 23 (7.4 m)	Bin 1 (1.6 m)	Bin 18 (6.1 m)
Major ( $\text{cm s}^{-1}$ ) 10 min avg.	36.79	52.76	38.45	40.48
Minor ( $\text{cm s}^{-1}$ ) 10 min avg.	8.96	12.93	12.88	15.40
Orient. ( $^\circ\text{N}$ ) 10 min avg.	-100.23	-100.15	-59.56	-62.49
Ellip. 10 min avg.	0.7566	0.7550	0.6651	0.6196
Major ( $\text{cm s}^{-1}$ ) Low Pass	5.60	6.66	4.33	4.83
Minor ( $\text{cm s}^{-1}$ ) Low Pass	1.01	1.33	2.64	2.78
Orient. ( $^\circ\text{N}$ ) Low Pass	-106.27	-104.00	-58.65	-52.32
Ellip. Low Pass	0.8194	0.8009	0.3906	0.4252

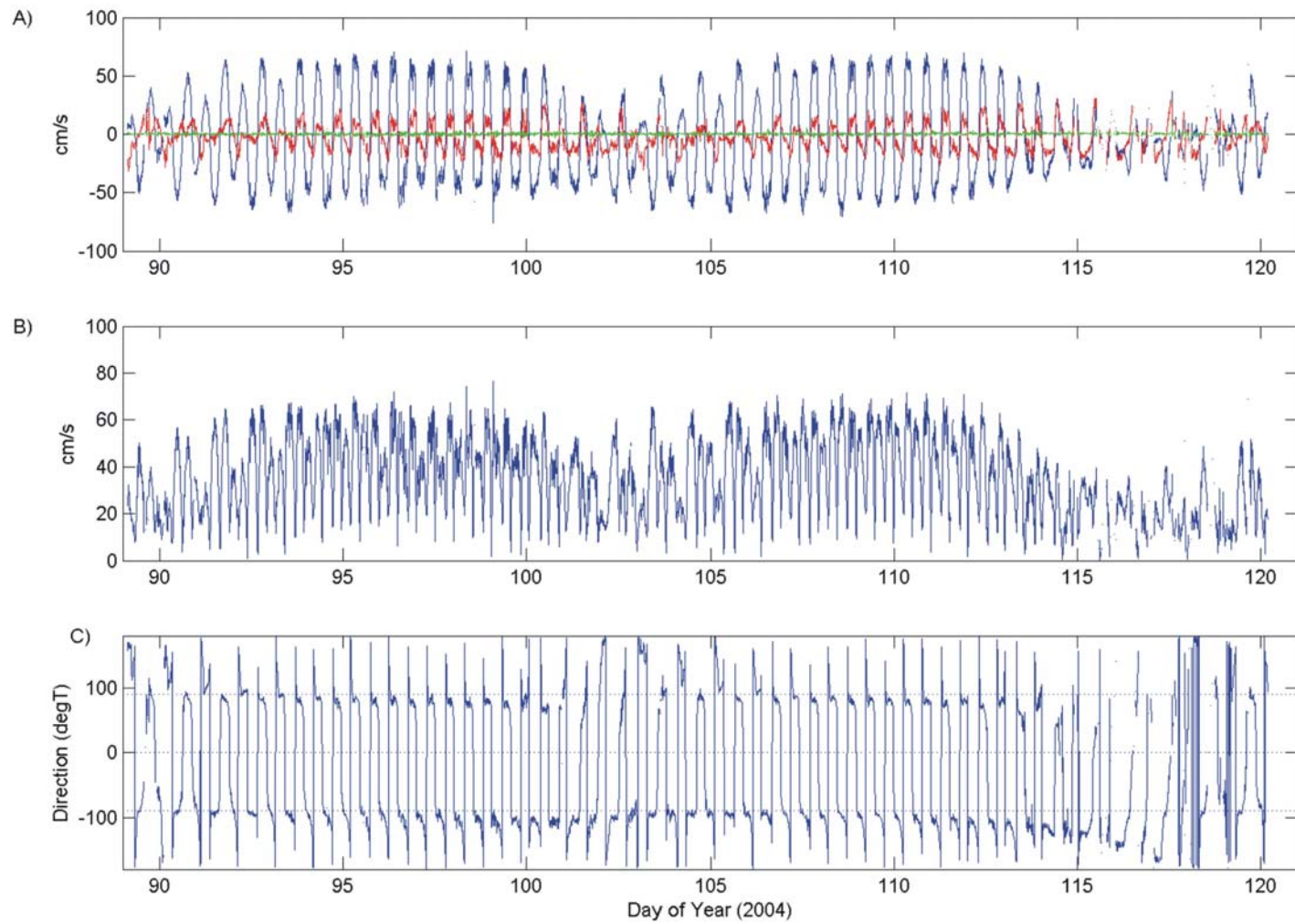


Figure 3.13. CSIRO-2 current meter time-series obtained from data recorded in bin 1 (1.6 m above seabed). a) Time series of East-North-Up velocity components; b) Time series of absolute current speed; c) Time series of current direction.

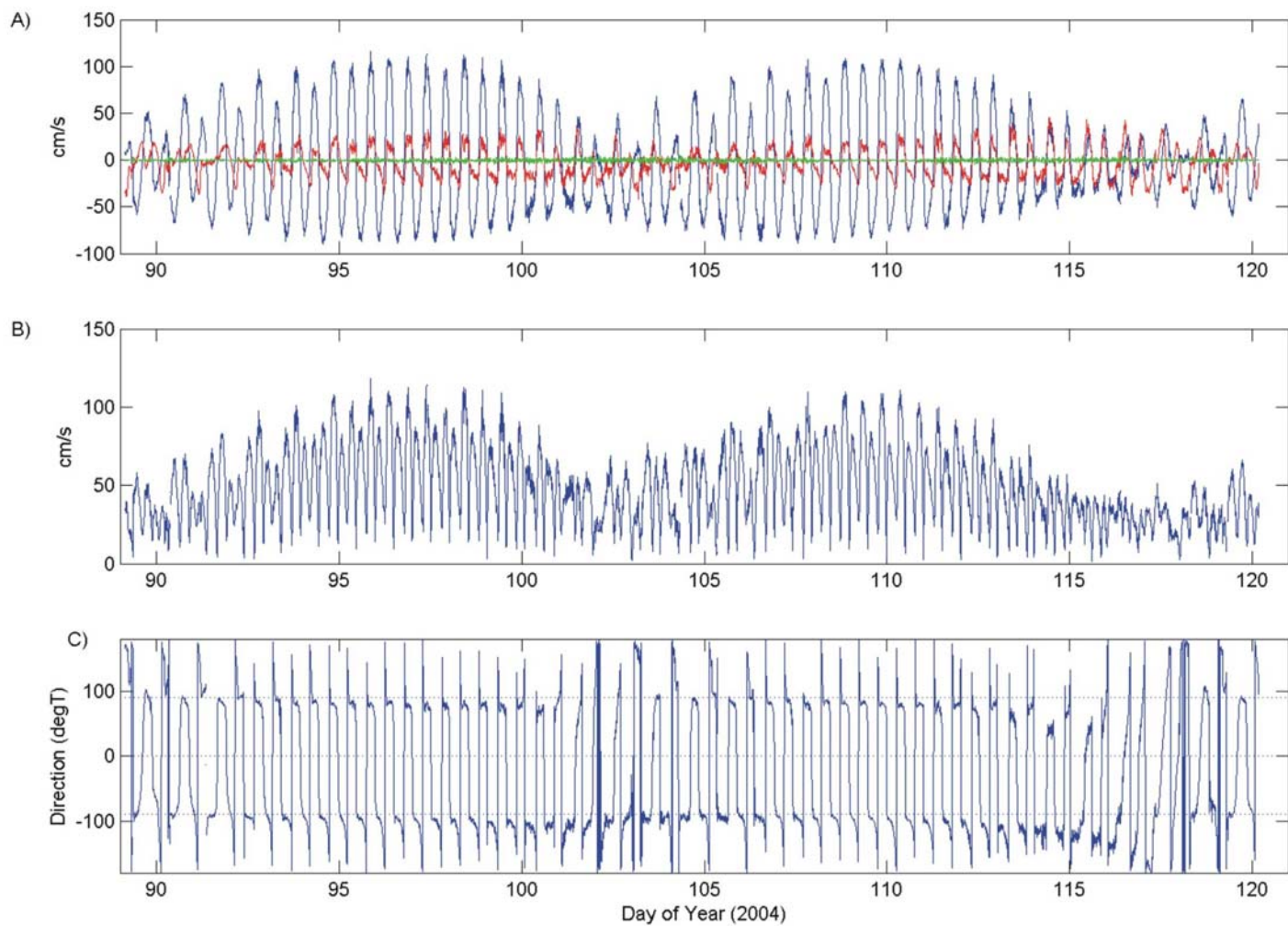


Figure 3.14. CSIRO-2 current meter time-series obtained from data recorded in bin 23 (7.4 m above seabed). a) Time series of East-North-Up velocity components; b) Time series of absolute current speed; c) Time series of current direction.

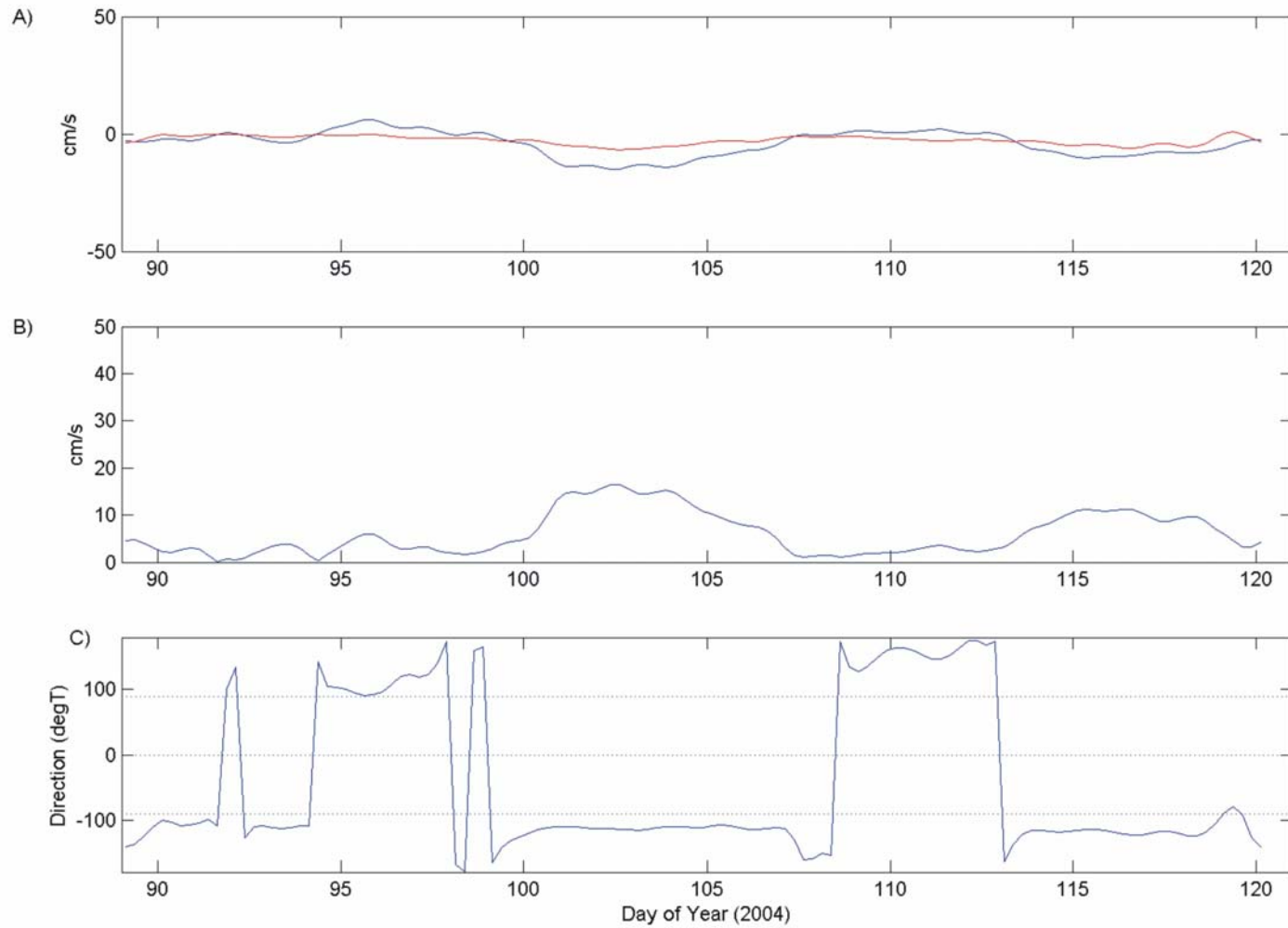


Figure 3.15. CSIRO-2 30-hr low-Pass Filtered current meter time-series obtained from data recorded in bin 1 (1.6 m above seabed). a) Time series of East-North-Up velocity components; b) Time series of absolute current speed; c) Time series of current direction.



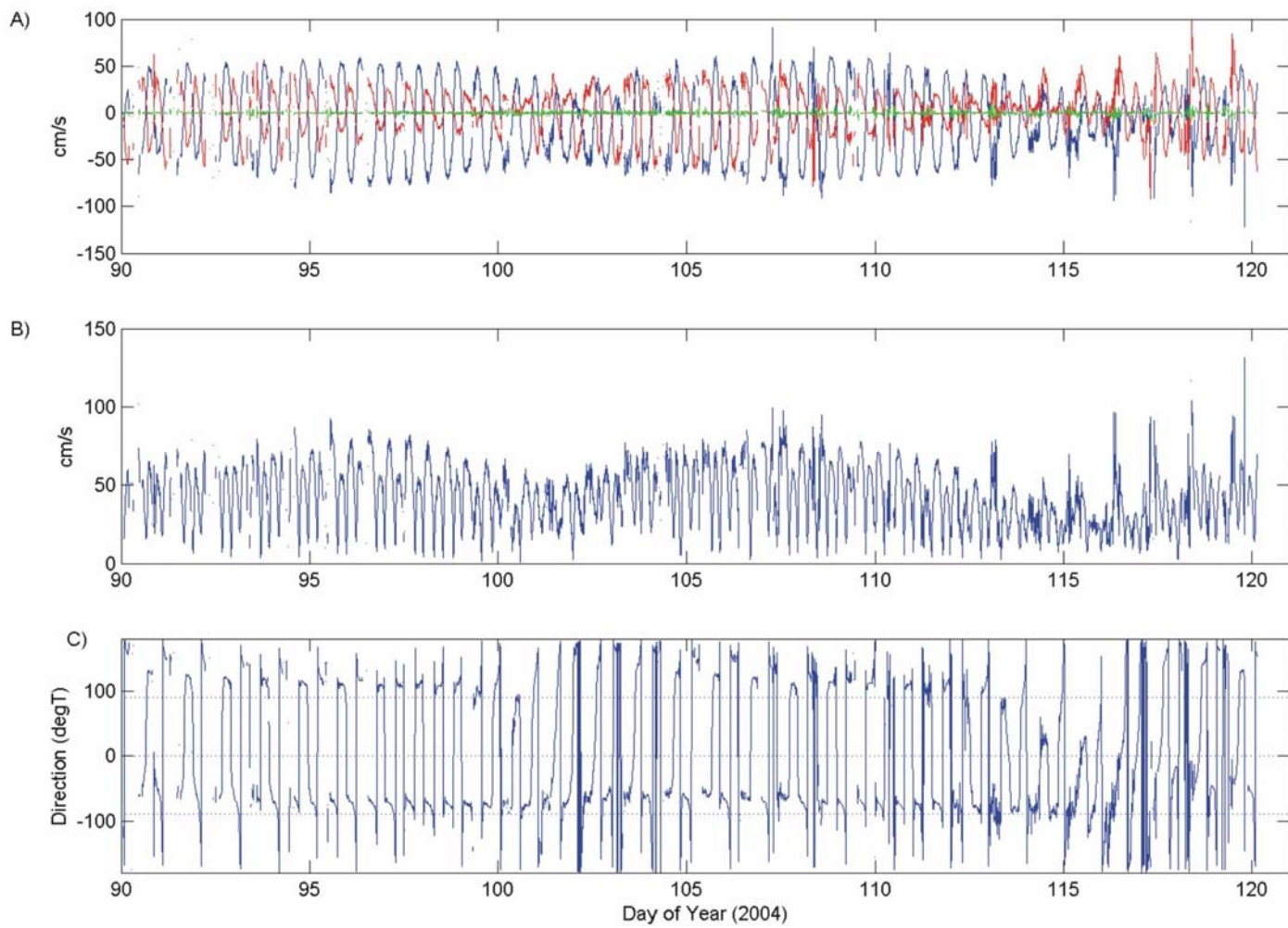


Figure 3.16. CSIRO-2 30-hr low-Pass Filtered current meter time-series obtained from data recorded in bin 23 (7.4 m above seabed). a) Time series of East-North-Up velocity components; b) Time series of absolute current speed; c) Time series of current direction.

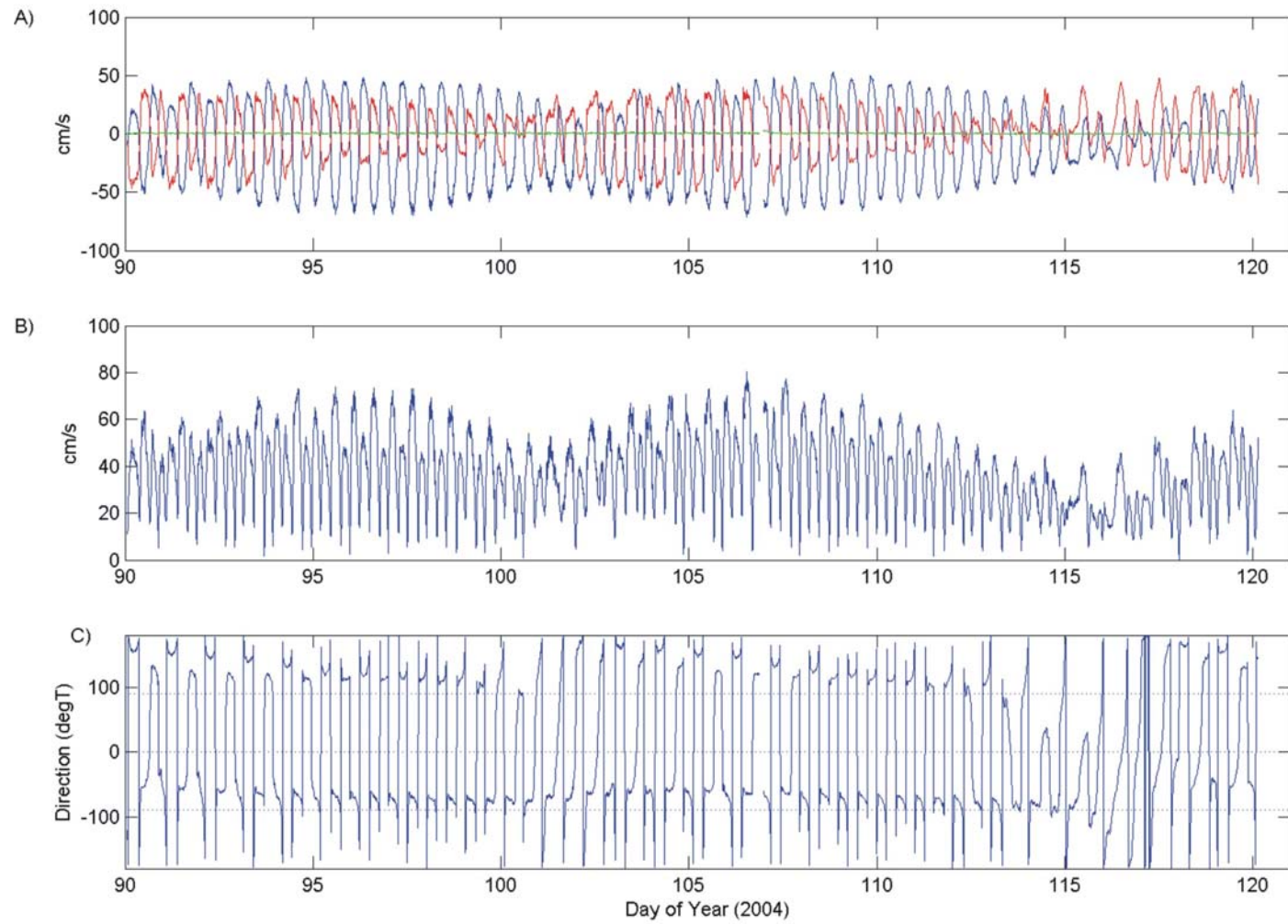


Figure 3.17. CSIRO-3 current meter time-series obtained from data recorded in bin 1 (1.6 m above seabed). a) Time series of East-North-Up velocity components; b) Time series of absolute current speed; c) Time series of current direction.

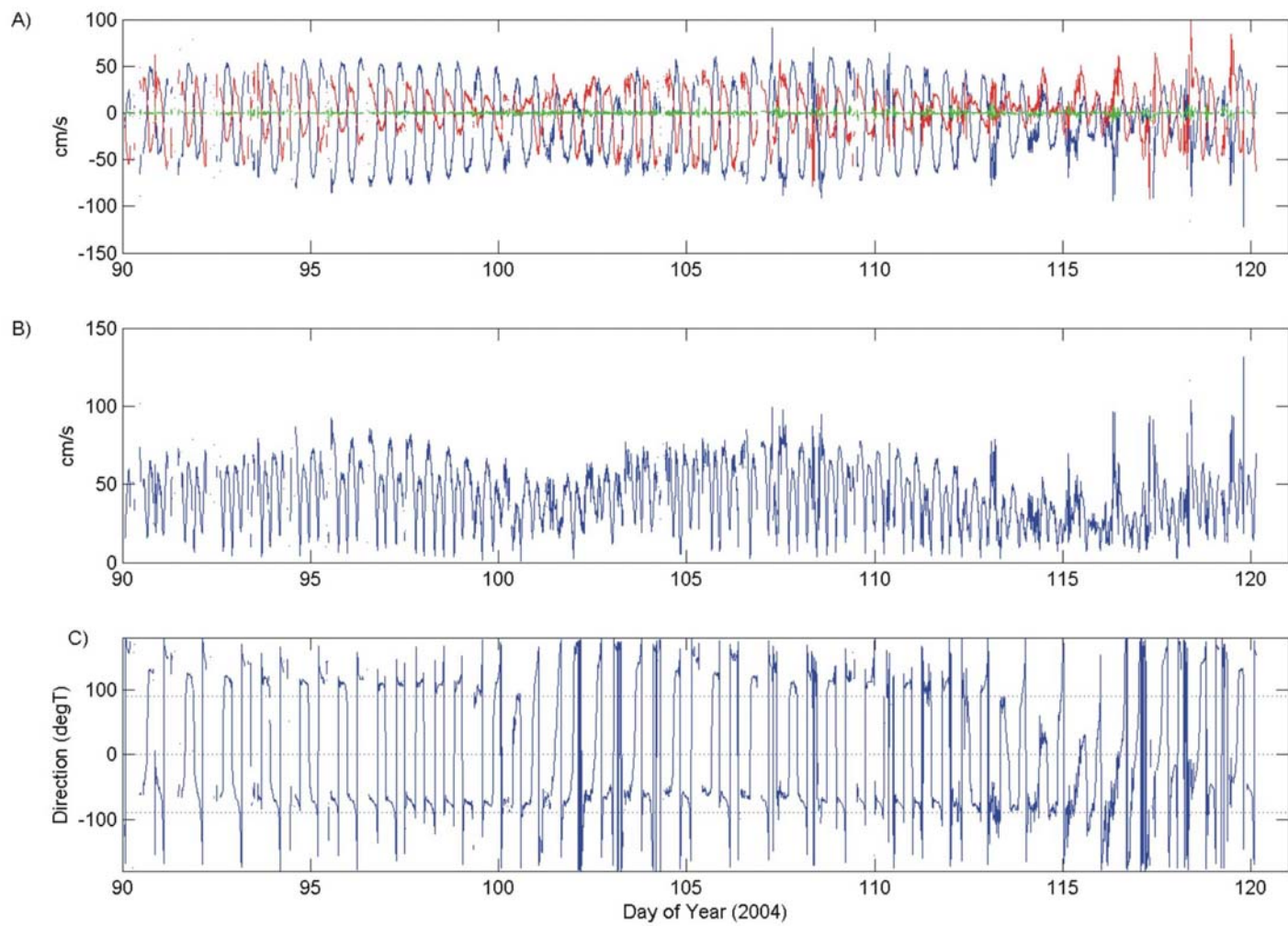


Figure 3.18. CSIRO-3 current meter time-series obtained from data recorded in bin 18 (6.1 m above seabed). a) Time series of East-North-Up velocity components; b) Time series of absolute current speed; c) Time series of current direction.

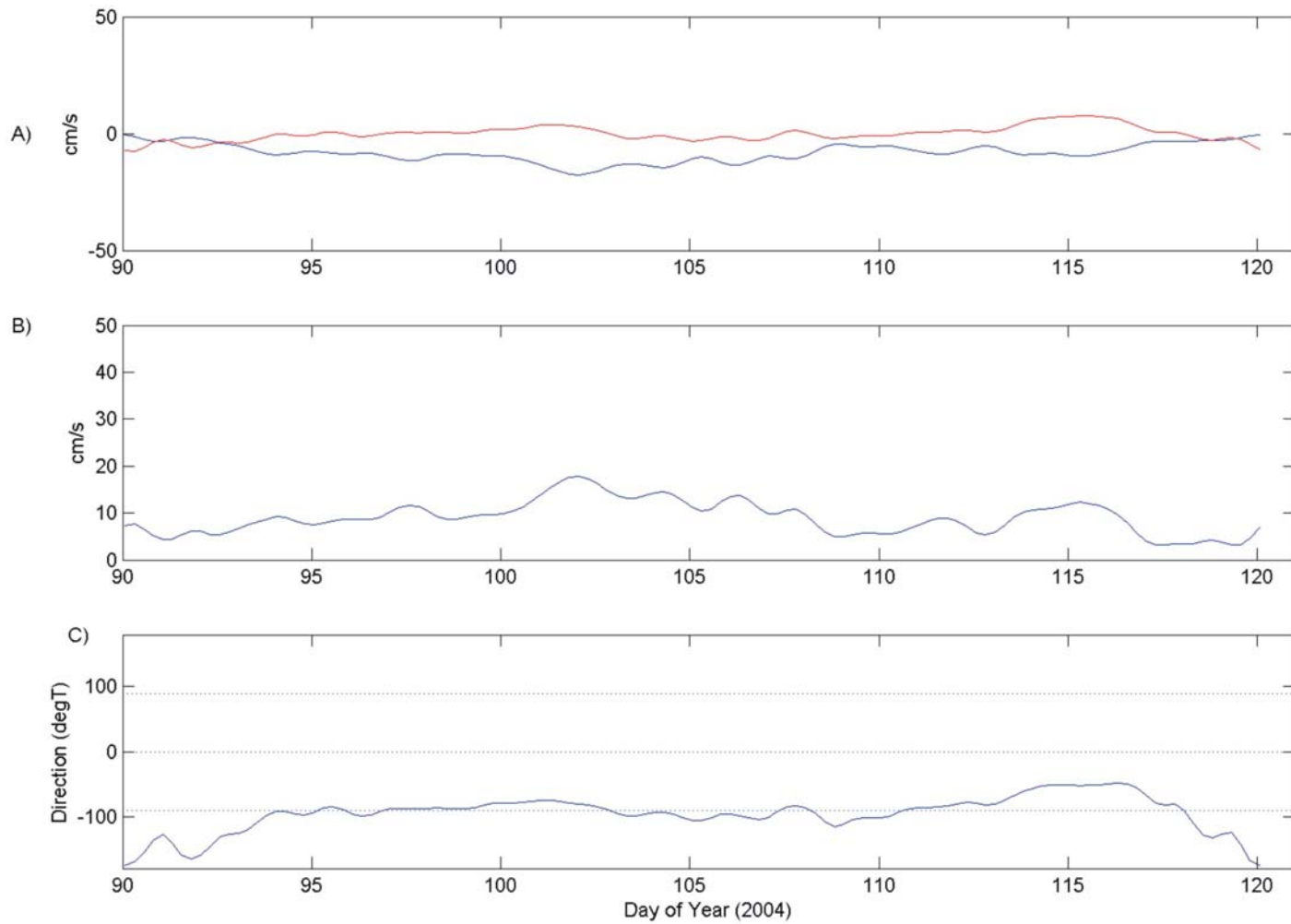


Figure 3.19. CSIRO-3 30-hr low-Pass Filtered current meter time-series obtained from data recorded in bin 1 (1.6 m above seabed). a) Time series of East-North-Up velocity components; b) Time series of absolute current speed; c) Time series of current direction.

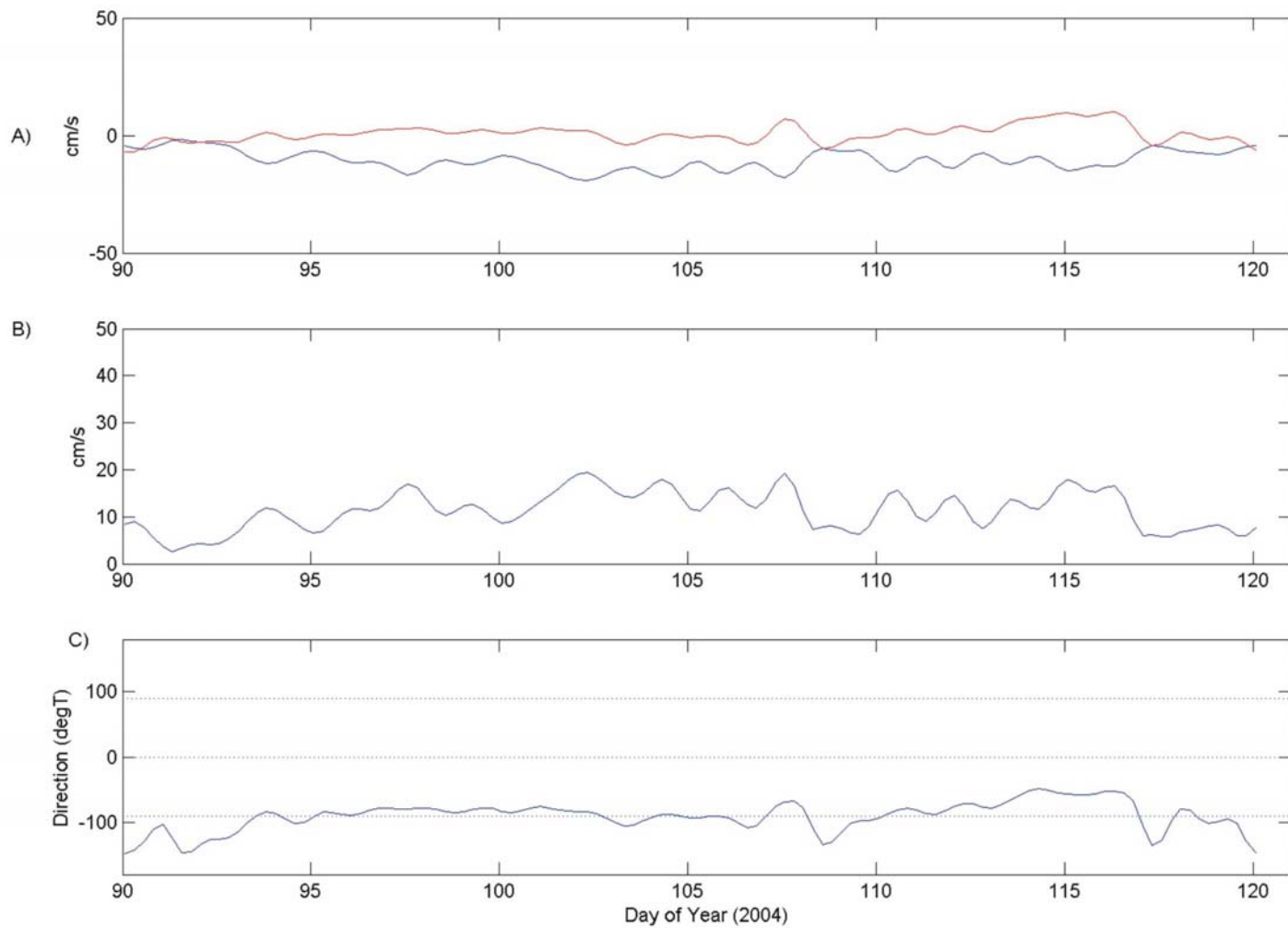


Figure 3.20. CSIRO-3 30-hr low-Pass Filtered current meter time-series obtained from data recorded in bin 18 (6.1 m above seabed). a) Time series of East-North-Up velocity components; b) Time series of absolute current speed; c) Time series of current direction.



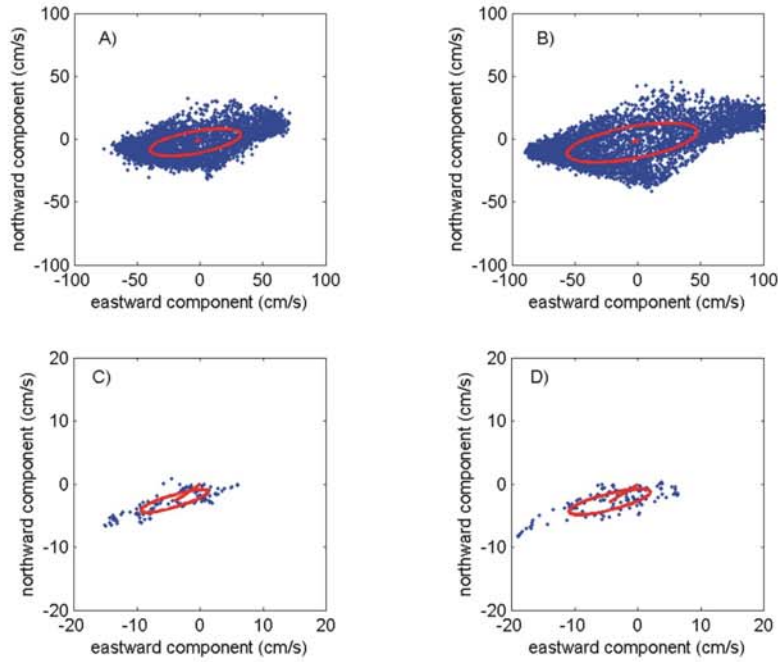


Figure 3.21. CSIRO-2 current meter scatter plot. a) 10-min processed current data from bin 1 (1.6 mab); b) 10-min processed current data from bin 23 (7.4 mab); c) 30-hr low-pass filtered current data from bin 1 (1.6 mab); d) 30-hr low-pass filtered current data from bin 23 (7.4 mab). Each plot has the calculated ellipse of the principal axes of the currents, and the mean current vector (origin zero) superimposed. The ellipse is centred upon the mean current vector.

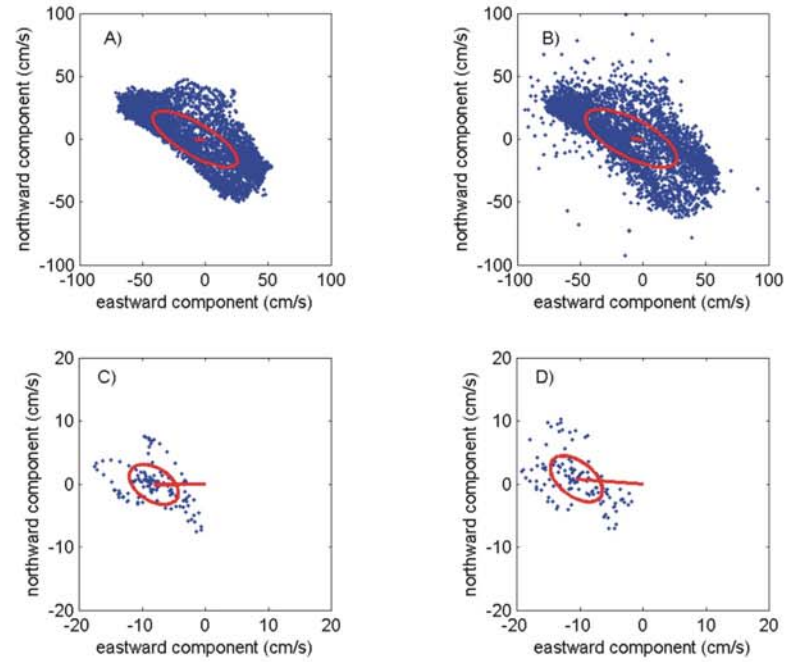


Figure 3.22. CSIRO-3 current meter scatter plot. a) 10-min processed current data from bin 1 (1.6 mab); b) 10-min processed current data from bin 18 (6.1 mab); c) 30-hr low-pass filtered current data from bin 1 (1.6 mab); d) 30-hr low-pass filtered current data from bin 18 (6.1 mab). Each plot has the calculated ellipse of the principal axes of the currents, and the mean current vector (origin zero) superimposed. The ellipse is centred upon the mean current vector.

Despite the mean currents at CSIRO-3 being larger than those at CSIRO-2 (Table 3.8), the major axis is larger at CSIRO-2 (Table 3.8). This indicates that the tidal displacement is larger at CSIRO-2, but net displacement at CSIRO-3 is larger.

Tidal analysis of the current meter records at CSIRO-2 and CSIRO-3 show, in agreement with the sea-level record, the tides at the two mooring sites is mixed, semi-diurnal, with the principal lunar tide (M2) being the most dominant constituent (Table 3.10).

Table 3.10. Tidal Ellipse parameters of bed and surface currents from a) CSIRO-2 and b) CSIRO-3.

a) CSIRO-2						
Bin	Tide	Semi-major Axis (cm s <sup>-1</sup> )	Eccentricity	Inclination (degrees)	Phase (degrees)	
1	M2	43.31	0.99	8.83	312.87	
	S2	24.21	0.635	13.81	9.58	
	K1	5.36	0.237	38.34	60.38	
	O1	6.72	0.653	28.99	1.29	
23	M2	61.94	0.995	8.15	312.48	
	S2	36.41	0.669	13.19	13.43	
	K1	5.58	0.231	49.04	46.70	
	O1	8.18	0.718	36.67	339.46	
b) CSIRO-3						
Bin	Tide	Semi-major Axis (cm s <sup>-1</sup> )	Eccentricity	Inclination (degrees)	Phase (degrees)	
1	M2	44.94	0.858	152.88	83.84	
	S2	24.65	0.605	149.51	246.80	
	K1	9.39	0.764	106.35	217.70	
	O1	6.94	0.459	91.37	2.71	
18	M2	50.32	0.877	153.80	80.76	
	S2	26.36	0.558	150.22	243.83	
	K1	10.44	0.671	101.97	214.71	
	O1	7.38	0.449	85.22	2.32	

At CSIRO-2, the M2 tides high eccentricity (0.99) and inclination of ~9° indicates that the dominant tide is almost rectilinear in an east-west direction. At CSIRO-3, the M2 tide also exhibits a relatively high eccentricity (0.86), is aligned more to the north-west, south-east, and is not as eccentric (Table 3.10). These characteristics are clearly illustrated by the tidal ellipses shown in Figures 3.23a and 3.24a, and show similar characteristics at the surface and the sea-bed. These strong almost rectilinear M2 tides are most likely set-up as a result of the large phase differences observed between the two sites.

At both CSIRO-2 and CSIRO-3, the S2 tidal constituent is also relatively large (the semi-major axis is approximately 25 cm s<sup>-1</sup>; Table 3.10). The inclination of the S2 tide is aligned closely with the M2 tide, however the S2 tide has a smaller eccentricity (more circular), defining a less rectilinear current as a result of the S2 constituent (Figs. 3.23b, 3.24b).

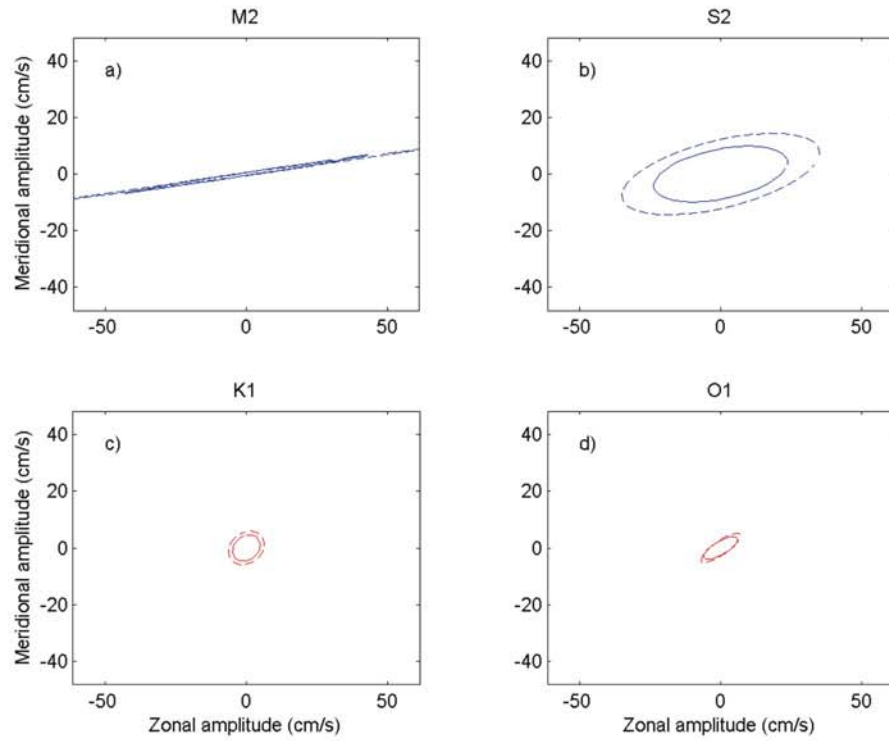


Figure 3.23. CSIRO-2 Tidal ellipses plotted for the four major constituents a) M2, b) S2, c) K1, and d) O1. Red indicates that the ellipses are travelled clockwise, blue indicates that the ellipses are travelled anti-clockwise. Dashed lines indicate 'surface' (bin 23, 7.4 mab) ellipses, solid lines indicate 'bed' ellipses (bin 1, 1.6 mab).

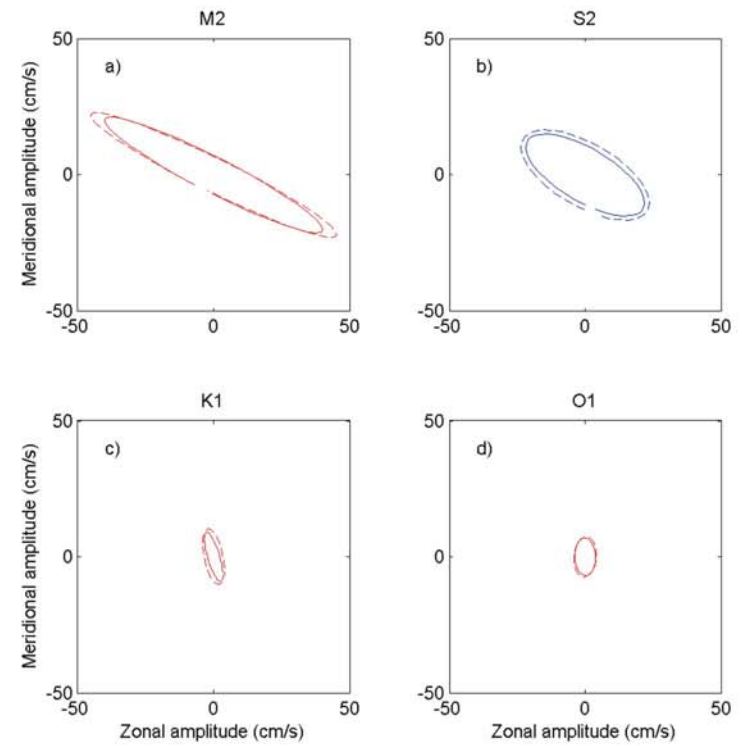


Figure 3.24. CSIRO-3 Tidal ellipses plotted for the four major constituents a) M2, b) S2, c) K1, and d) O1. Red indicates that the ellipses are travelled clockwise, blue indicates that the ellipses are travelled anti-clockwise. Dashed lines indicate 'surface' (bin 18, 6.1 mab) ellipses, solid lines indicate 'bed' ellipses (bin 1, 1.6 mab).

The semi-major axes of the diurnal constituents, K1 and O1, have much smaller magnitudes than the semi-diurnal constituents (Table 3.10). The eccentricity of the diurnal constituents is smaller, suggesting a more circular motion (Figs. 3.23c-d; 3.24c-d). However, given the smaller magnitude of the diurnal constituents, these currents are not clearly apparent in the current meter record.

### 3.3.3. Bedload Transport Estimates

The ADCP's located on CSIRO-2 and CSIRO-3 were not configured to record wave statistics. Estimates of bed shear stresses, and hence bedload transport, are based on the assumption of a steady flow. Five methods were used to estimate bedload transport at each location, so that a range of values could be obtained, and errors in bedload transport estimates from previous researchers could be deduced. The methods used are as follows:

1. Bagnold's bedload equation, modified by Gadd et al. (1978):

$$q = (\beta / \rho_s) (u_{100} - u_{cr})^3 \quad (9)$$

where  $q$  is the volume rate of sediment transport per unit width of bed ( $m^2/s$ ),  $\beta = 1.73$  as used in the SEDTRANS96 model (Li & Amos, 2001),  $\rho_s$  = density of the bed sediment. The critical velocity for the initiation of bedload transport ( $u_{cr}$ ) is obtained from  $\tau_{cr} = 0.5 \rho_{cs} u_{cr}^2$ , where  $\tau_{cr}$  is the critical shear stress required for bedload transport ( $N m^{-2}$ ) and  $f_{cs}$  is the dimensionless current friction factor.  $u_{100}$  is the current speed measured 1.0 m above the bed ( $cm s^{-1}$ ).

2. The Engelund-Hansen (1967) total load equation. For continental shelf conditions, this equation can be modified to (Li & Amos, 2001):

$$q = 0.05 u_{100}^2 \rho^2 u^{*3} / D (\Delta \rho g)^2, \quad (10)$$

where  $\Delta \rho = \rho_s - \rho$ , and  $\rho_s$  is the density of the bed sediment. The surface sediments are >75% carbonate grains (see Fig. 4.11a) so this value is assumed to be  $2700 kg m^{-3}$ .  $\rho$  is the density of seawater,  $u^*$  is the skin-friction shear velocity,  $g$  is the acceleration due to gravity or  $9.8 m s^{-2}$ , and  $D$  is sediment grain size (m).

3. The Einstein-Brown bedload equation (Brown, 1950). This equation can be written as (Li and Amos., 2001):

$$q = 40 W_s D (\rho / \Delta \rho g D)^3 u^{*5} |u^*|, \quad (11)$$

where  $W_s$  is the settling velocity ( $m s^{-1}$ ).

4. Yalin bedload equation (Yalin, 1963):

$$q = 0.635 D u^* [(\tau^* - (1/a) \ln(1 + a \tau^*))], \quad (12)$$

where  $\tau^* = (\tau_b - \tau_{cr}) / \tau_{cr}$  and is the normalised bed shear stress and  $a = 2.45(\rho / \rho_s)^{0.4} (\tau_{cr} / \Delta\rho g D)^{0.5}$ .

5. Bagnold's bedload equation as modified by Hardisty (1983):

$$q = k1(u_{100}^2 - u_{cr}^2) u_{100}, \quad (13)$$

where the critical threshold velocity in this instance is calculated as  $u_{cr} = 1.226(100D)^{1.29}$  as outlined by Miller et al. (1977).  $k1$  is a function of sediment grain size ( $D$ ) and is calculated as  $k1 = [1/6.6 (1000D)]^{1.23} \text{ kg m}^{-4} \text{ s}^2$ .

All of the bedload transport estimates calculated above have units of  $\text{m}^2 \text{ s}^{-1}$ . They were multiplied by  $1/(10\rho_s)$  to express them in units of  $\text{g cm}^{-1} \text{ s}^{-1}$  to be consistent with previous Geoscience Australia publications. Where appropriate, a mean grain size of 0.0005 m has been assumed in the calculations.

Mean bedload transport rates in the vicinity of CSIRO-2 for the entire deployment range from  $0.16 \times 10^{-2} \text{ g cm}^{-1} \text{ s}^{-1}$  using equation 13 to  $1.92 \times 10^{-2} \text{ g cm}^{-1} \text{ s}^{-1}$  using equation 9 (Table 3.11). Total bedload transport rates ranged from  $0.17 \times 10^4 \text{ g cm}^{-1}$  using equation 13 to  $1.55 \times 10^4 \text{ g cm}^{-1}$  using equation 9. Net bedload transport directions over the period of deployment were to the ESE and E. Each method used is based on differing empirical relations obtained in various laboratories. Differences in the net transport and direction observed are related to the differences between the methods, particularly in relation to the critical speed at which sediment transport commences. Bagnold's equation, as modified by Hardisty (1983), provided the lowest bedload transport rates but these rates were of similar magnitude to the rates calculated by three of the other equations.

Significant bedload transport occurred from Julian Day (JD) 94 to 100 and again from JD 107 to 117 at CSIRO-2 (Fig. 3.25a-e). An apparent property of bedload estimates at CSIRO-2 is that despite the net current moving to the west, bedload transport estimates are eastwards. Figure 3.25 indicates that sediment is transported during the period of eastward currents, and not during westward currents. During periods of strongest current magnitudes when currents are capable of mobilising bed sediments, eastward currents are larger than westward currents, however, during the period where currents are not large enough to mobilise bed sediments, westward currents are larger. Bagnold estimates (Eq. 9), indicate little to no bedload transport to the south-west, as predicted by the other methods (Fig. 3.25a). Consequently, the large eastward transport is predicted using this method.

Table 3.11 Bedload transport estimates in the vicinity of CSIRO-2.

	Bagnold (Gadd et al., 1978)	Engelund- Hansen	Einstein- Brown	Yalin	Bagnold (Hardisty, 1983)
q mean ( $10^{-2} \text{ g cm}^{-1} \text{ s}^{-1}$ )	1.92	1.77	0.41	0.92	0.16
q total ( $10^4 \text{ g cm}^{-1}$ )	1.55	0.48	0.16	0.40	0.17
Direction (° T)	73.45	67.73	69.85	91.54	75.08



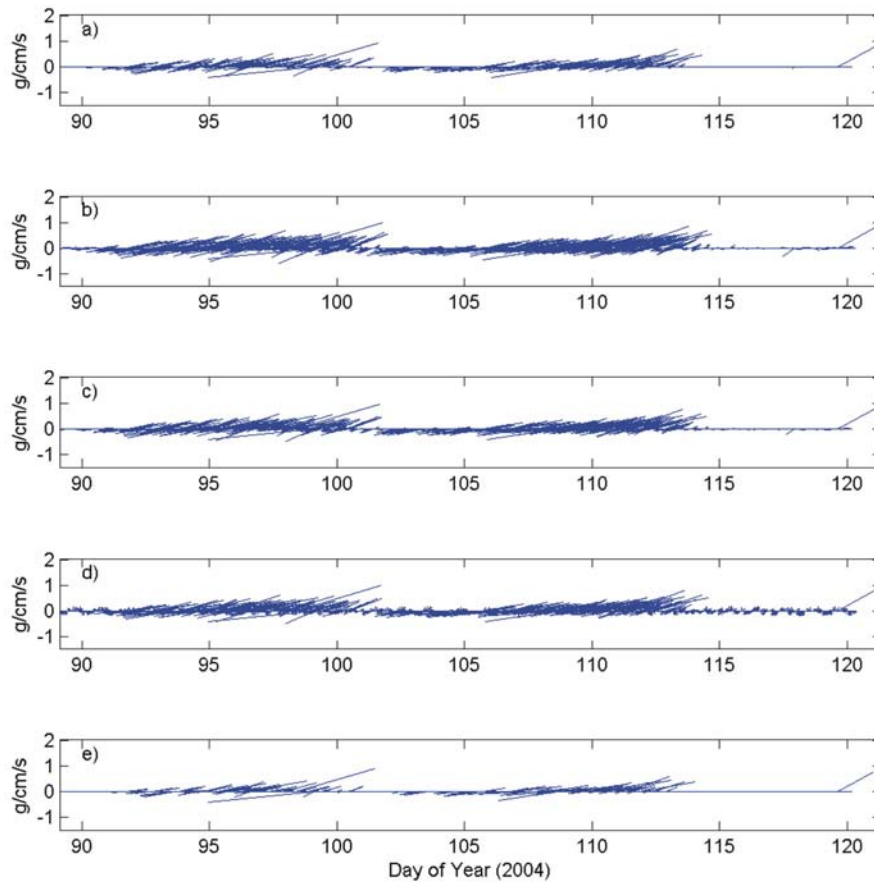


Figure 3.25. Vector stick plots of bedload transport at CSIRO-2, as calculated using a) Bagnold (Gadd et al., 1978), b) Engelund Hansen, c) Einstein-Brown, d) Yalin, e) Bagnold (Hardisty, 1983).

Mean bedload transport rates in the vicinity of CSIRO-3 for the entire deployment range from  $0.33 \times 10^{-2} \text{ g cm}^{-1} \text{ s}^{-1}$  using equation 13 to  $2.79 \times 10^{-2} \text{ g cm}^{-1} \text{ s}^{-1}$  using equation 9 (Table 3.12). Total bedload transport rates ranged from  $0.83 \times 10^4 \text{ g cm}^{-1}$  using equation 13 to  $6.50 \times 10^4 \text{ g cm}^{-1}$  using equation 9. Net bedload transport directions over the period of deployment were within  $4^\circ$  and towards the WSW. Bagnold's equation, as modified by Gadd et al. (1978), and the Engelund-Hansen equation provide similar estimates of the mean bedload transport. The Einstein-Brown equation and Bagnold's equation, as modified by Hardisty (1983), also provide very similar estimates of the mean bedload transport. Significant bedload transport occurred from JD 94 to 97 and again from JD 104 to 109 during periods of spring-tide currents (Fig. 3.26a-e). All methods indicate that current magnitudes during neap tides are insufficient to mobilise sediments (Fig. 3.26), and consequently, no transport is predicted during these periods. Transport is predominantly estimated to occur during the flood tide, when currents are heading westwards. This leads to the net westward transport experienced.

At both sites, Bagnold's equation, as modified by Hardisty (1983), provided the lowest bedload transport estimates and Bagnold's equation, as modified by Gadd (1977), provided the highest bedload transport estimates.

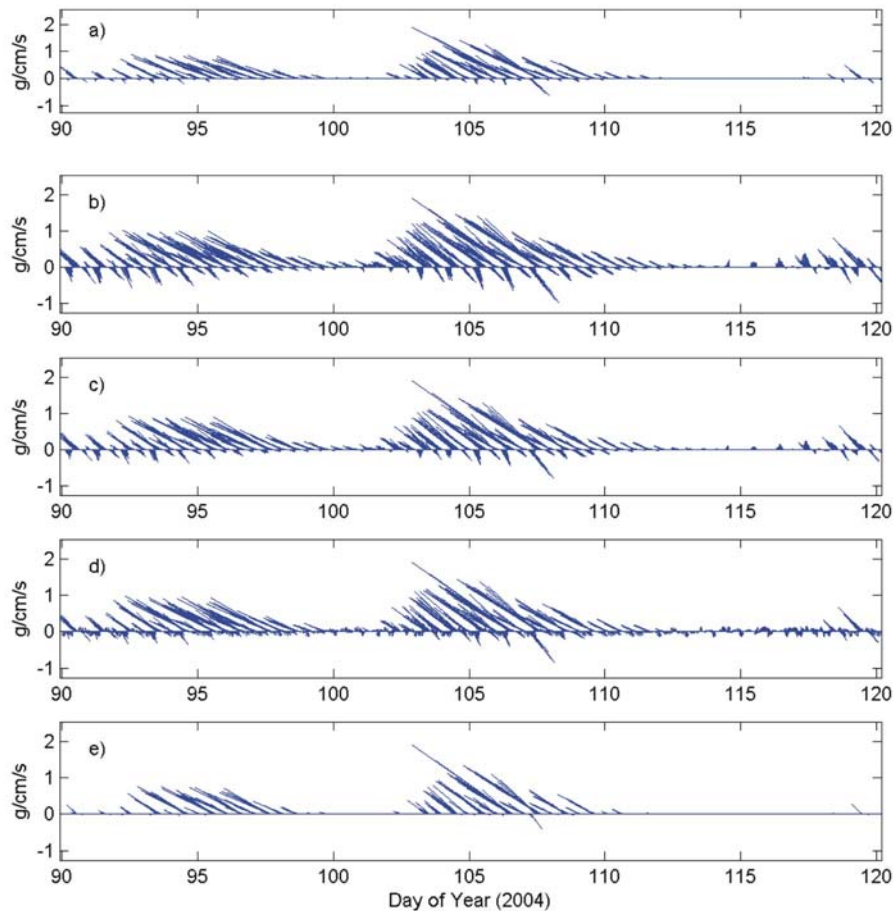


Figure 3.26. Vector stick plots of bedload transport at CSIRO-3, as calculated using a) Bagnold (Gadd et al., 1978), b) Engelund Hansen, c) Einstein-Brown, d) Yalin, e) Bagnold (Hardisty, 1983).

Table 3.12. Bedload transport estimates in the vicinity of CSIRO-3.

	Bagnold (Gadd et al., 1978)	Engelund- Hansen	Einstein- Brown	Yalin	Bagnold (Hardisty, 1983)
q mean ( $10^{-2} \text{ g cm}^{-1} \text{ s}^{-1}$ )	2.79	2.12	0.52	1.10	0.33
q total ( $10^4 \text{ g cm}^{-1}$ )	6.50	3.21	0.88	1.97	0.83
Direction (° T)	293.95	290.60	291.72	290.40	294.60

### 3.3.4. Estimates of Sandwave Migration

The swath sonar survey revealed that the crests of the sandwaves in Area A and Area B moved towards the west between the first and second survey (Section 2.4.1). The crests moved 6-19 m between the first and second swath surveys. The volume of sand transported by a moving sandwave of height  $H$  can be estimated as the product of the cross sectional area ( $A$ ) and celerity ( $C$ ) divided by the wavelength denoted by crest spacing ( $L$ ). Assuming

the sandwaves are triangular in cross-section ( $A = 0.5 LH$ ) then the volume transport rate ( $Q$ ) is:

$$Q_c = 0.5 HC, \quad (14)$$

where the subscript c denotes that the voids between sediment grains are included. In terms of the dry weight of sediment grains the volume transport rate is:

$$Q = 0.5d (1 - P) H C, \quad (15)$$

where  $P$  is the average porosity of the sediment of 0.59 (measured from the cores; [Section 4.3.5](#)), and  $d$  is the grain density ( $2.70 \text{ g cm}^{-3}$  for carbonate grains). Sandwave celerity is estimated by solving Equation 15 for  $C$  and using the estimated bedload transport rate ( $q$ ) and the sandwave height (2.0 m). Estimates of sandwave migration ( $Q$ ) have been computed based on the five bedload transport estimates ( $q$ ) calculated in [Section 3.3.3](#).

For sandwaves located in the vicinity of CSIRO-2, the estimated average migration rate or celerity over the period of deployment ranges from  $0.9 \text{ cm d}^{-1}$  using the Bagnold equation as modified by Hardisty (1983) to  $11 \text{ cm d}^{-1}$  using the Engelund-Hansen equation and the Bagnold equation as modified by Gadd et al. (1978) ([Table 3.12](#)). For sandwaves located in the vicinity of CSIRO-3, the estimated average migration rate or celerity over the period of deployment ranges from  $2 \text{ cm d}^{-1}$  using the Bagnold equation as modified by Hardisty (1983) to  $16 \text{ cm d}^{-1}$  using the Bagnold equation as modified by Gadd et al. (1978) ([Table 3.13](#)). Not surprisingly, the magnitudes of the migration rates are reflected in the magnitude of the net bedload transport rates calculated in [Section 3.3.3](#).

Table 3.13. Sandwave migration rates in  $\text{m d}^{-1}$  for the entire deployment in the vicinity of CSIRO-2 and CSIRO-3.

	Bagnold (Gadd et al., 1978)	Engelund- Hansen	Einstein-Brown	Yalin	Bagnold (Hardisty, 1983)
CSIRO-2	11.0	11.0	2.4	5.3	0.9
CSIRO-3	16.0	12.2	3.0	6.3	2.0

## 4. Sedimentology

### 4.1. SAMPLE ACQUISITION

A total of 83 stations were occupied during the survey (Fig. 4.1). The locations of the stations were designed to capture the full spectrum of sedimentary environments and habitats. A variety of operations were undertaken at each station to characterise the seabed sediments, sedimentary processes, and biota and habitats (Table 4.1).

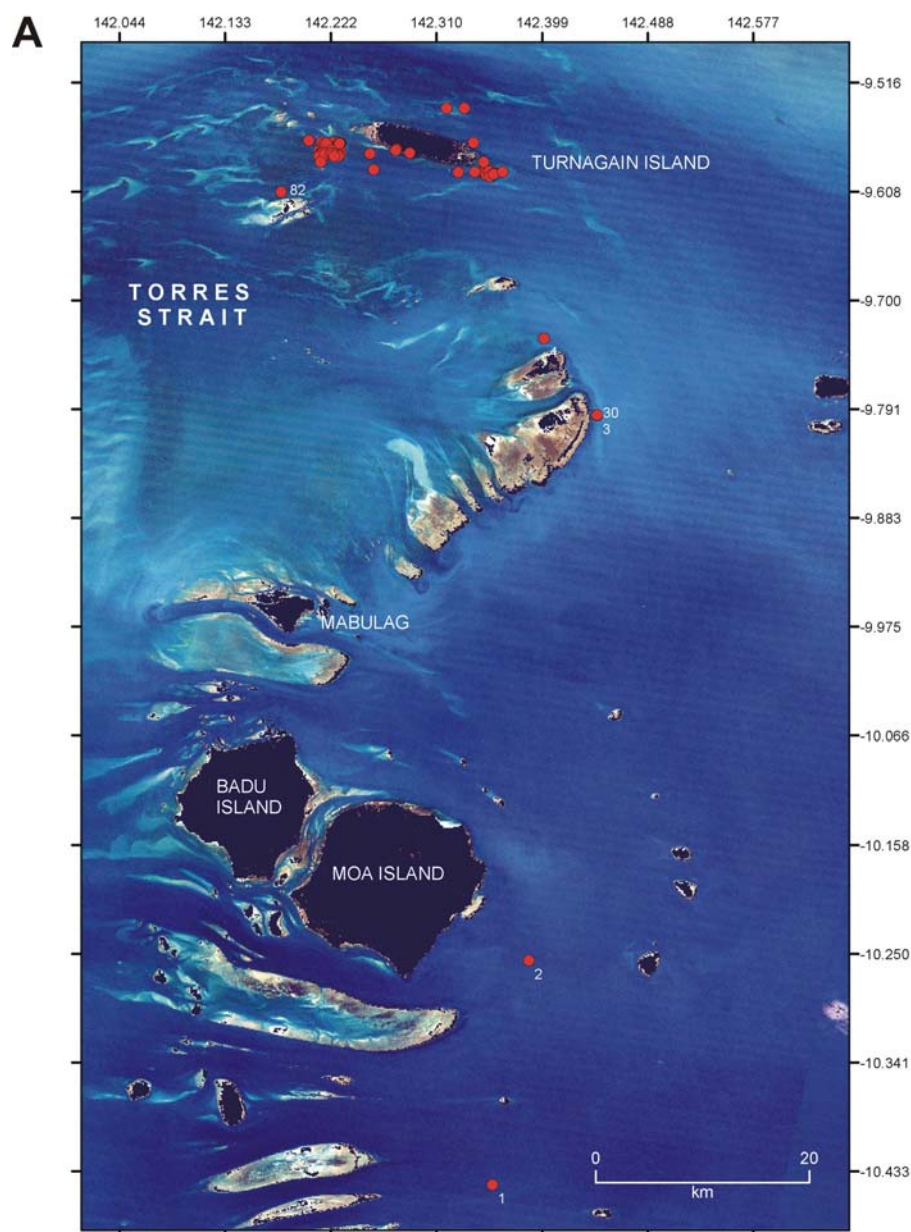


Figure 4.1. Map showing location of sample stations for a) regional, b) Area A and c) Area B sites. The locations of the stations were designed to capture the full spectrum of sedimentary environments and habitats. A variety of operations were undertaken at each station to characterise the seabed, sedimentary and oceanographic processes, and habitats and biota (see Table 4.1).

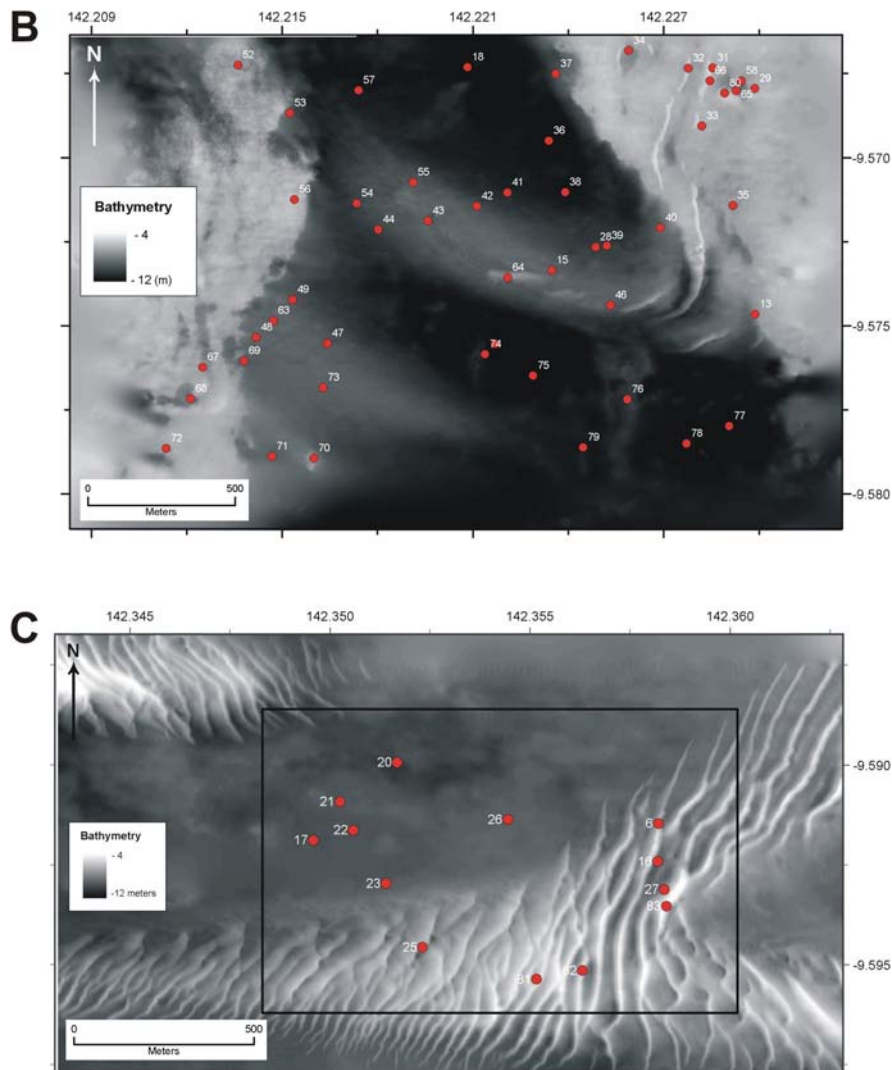


Figure 4.1-cont. See page 63 for caption.

#### 4.1.1. Water Samples

A total of 301 water samples (WS1-WS301) were taken using a 2 litre Niskin bottle fitted with a messenger (Fig. 4.2a; Table 4.1). The Niskin bottle was lowered to the bed and then raised approximately 0.5 m off the bottom before the messenger was sent down the wire to trigger the Niskin bottle and collect the water sample. Water samples were collected at select locations on the transit from Thursday Island to the study sites and every 20 minutes at four stations (58, 62, 80, 81) that were occupied for 25 hours to capture suspended sediment concentrations over an entire neap and spring tidal cycle in both Area A and B. The details were entered into Geoscience Australia's Marine Sediment database (MARS).

#### 4.1.2. Digital Video Footage

Video footage of the seabed was collected to characterise the substrate, morphology, habitats, and benthic biota in the study area (Fig. 4.1; Table 4.1). A video camera was lowered to the seabed and recorded a minimum of three minutes of video. The video camera was built by Geoscience Australia and consists of a digital video camera in a watertight housing attached



Table 4.1. Station operations.

Station	Camera	Grab	Core	Water Sample	Station	Camera	Grab	Core	Water Sample
1	-	-	-	WS1	43	CAM38	GR39	-	-
2	-	-	-	WS2	44	CAM39	GR40	-	-
3	CAM1	GR1	-	WS3	45	CAM40	GR41	-	-
4	-	GR2, 3	-	-	46	CAM41	GR42	-	-
5	CAM2	GR4	-	-	47	CAM42	GR43	-	-
6	CAM3	GR5	-	-	48	CAM43	GR44	-	-
7	CAM4	GR6	-	-	49	CAM44	GR45	-	-
8	CAM5	GR7	-	-	50	CAM45	GR46	-	-
9	CAM6	GR8	-	-	51	CAM46	GR47	-	-
10	CAM7	GR9	-	-	52	CAM47	GR48	-	-
11	CAM8	GR10	-	-	53	CAM48	GR49	-	-
12	CAM9	GR11	-	-	54	CAM49	GR50	-	-
13	CAM10	GR12	-	-	55	CAM50	GR51	-	-
14	CAM11	GR13	-	-	56	CAM51	GR52	-	-
15	CAM12	GR14	-	WS4	57	CAM52	GR53	-	-
16	-	-	-	-	58	CAM53	-	-	WS6-77
17	-	-	-	-	59	-	GR54	-	-
18	CAM13	GR15	-	-	60	-	GR55	-	-
19	CAM14	-	-	-	61	-	GR56	-	-
20	CAM15	GR16	-	-	62	CAM54	GR57	-	WS78-152
21	CAM16	GR17	-	-	63	-	-	VC1	-
22	CAM17	GR18	-	-	64	-	-	VC2, 3	-
23	CAM18	GR19	-	-	65	-	-	VC4, 5	-
24	CAM19	GR20	-	-	66	-	-	VC6	-
25	CAM20	GR21	-	-	67	CAM55	GR58	-	-
26	CAM21	GR22	-	-	68	CAM56	GR59	-	-
27	CAM22	GR23	-	WS5	69	CAM57	GR60	-	-
28	CAM23	GR24	-	-	70	CAM58	GR61	-	-
29	CAM24	GR25	-	-	71	CAM59	GR62	-	-
30	CAM25	GR26	-	-	72	CAM60	GR63	-	-
31	CAM26	GR27	-	-	73	CAM61	GR64	-	-
32	CAM27	GR28	-	-	74	CAM62	GR65	-	-
33	CAM28	GR29	-	-	75	CAM63	GR66	-	-
34	CAM29	GR30	-	-	76	CAM64	GR67	-	-
35	CAM30	GR31	-	-	77	CAM65	GR68	-	-
36	CAM31	GR32	-	-	78	CAM66	GR69	-	-
37	CAM32	GR33	-	-	79	CAM67	GR70	-	-
38	CAM33	GR34	-	-	80	CAM68	-	-	WS155-228
39	CAM34	GR35	-	-	81	CAM69	-	-	WS229-301
40	CAM35	GR36	-	-	82	-	GR71	-	-
41	CAM36	GR37	-	-	83	-	-	VC7, 8	-
42	CAM37	GR38	-	-					

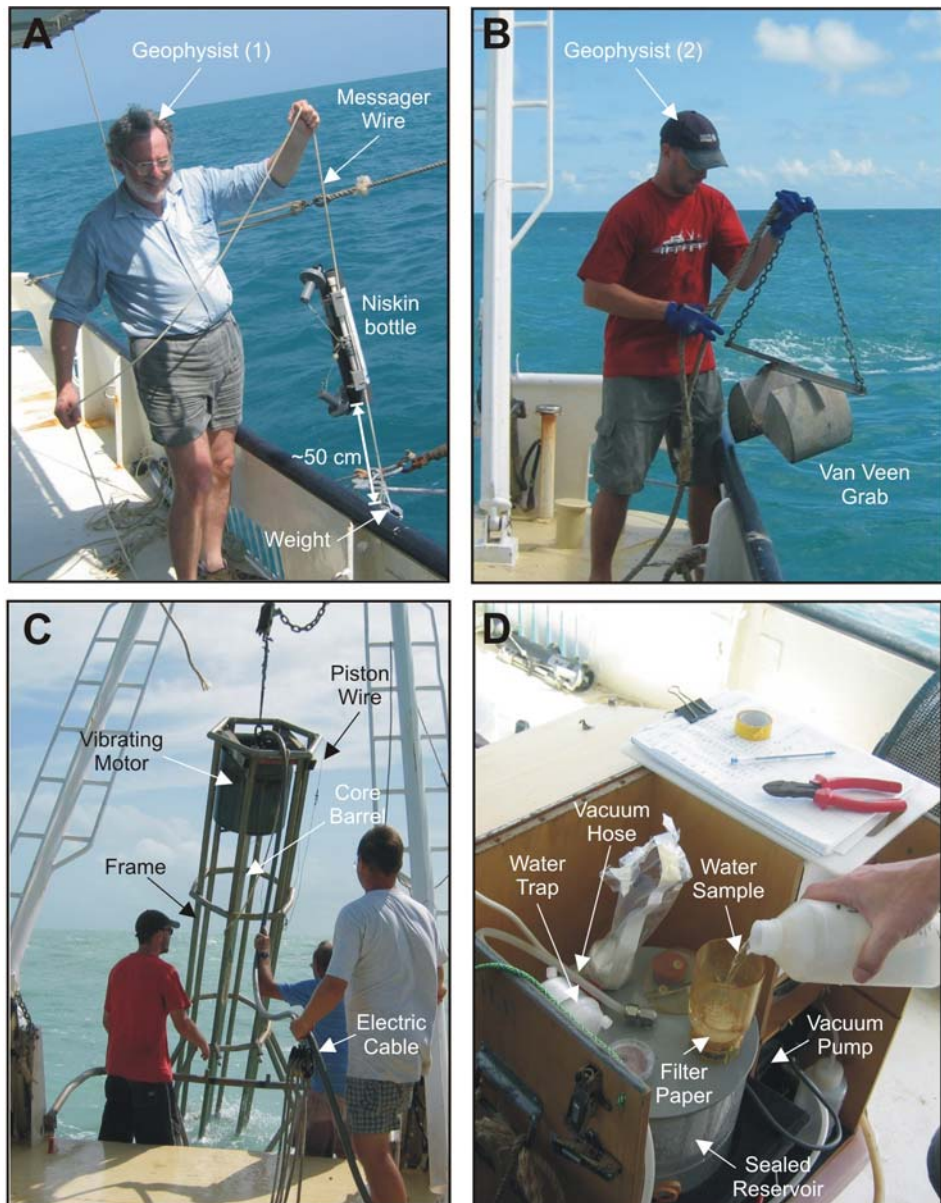


Figure 4.2. Photographs of: a) Niskin bottle for water samples, b) Van-veen grab for surface samples, c) electric vibrocorer for sub-surface samples, and d) water filtering system. Note that in c) the piston wire is extended indicating that the vibrocorer is being retrieved and the electric cable has been disconnected from the power source.

to a steel frame (Fig. 4.3). Two 25W halogen lights were used to illuminate the seabed where necessary. In addition, the camera was deployed at four stations to collect digital footage of the seabed to monitor the resuspension of bed sediment. At each station approximately 90 seconds of video was collected every 20 minutes for 25 hours (i.e., over one tidal cycle) and was timed to correspond to measurements of tide and wave currents with an acoustic current meter. Due to difficulties in maintaining a constant position at the 25-hour stations, the camera frame was lowered to the seabed just before the measurements were taken. At all sites, a cm-scale was set up on the camera frame in the view finder to determine the size of seabed features and objects in the water column. The underwater camera captured real-time broadcast quality digital footage that was recorded on digital videotape in the camera and was also fed to VHS tape on board the vessel. All video footage is contained in [Appendix F](#).

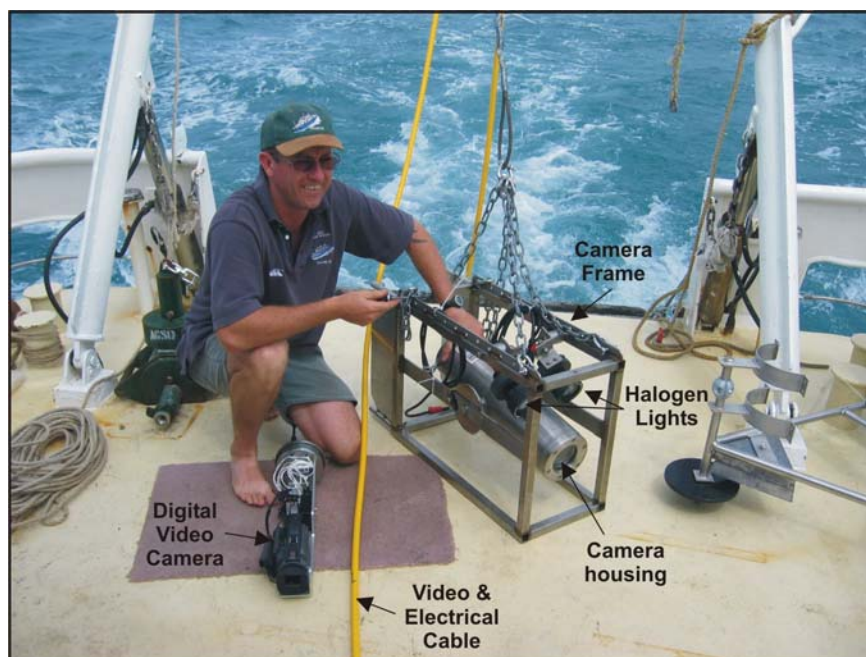


Figure 4.3. Photograph of the underwater digital video camera. The camera provides broadcast quality digital video. The camera and lights are powered from the surface and a live video feed is transmitted to the vessel.

### 4.1.3. Surface Sediment Sampling

Samples of the seabed were collected using a Van-Veen grab (Fig. 4.2b). Each grab was sub-sampled for bulk sediment and seagrass types. All sub-samples were double bagged, labelled (including an aluminium tag), stored in a refrigerated container, and the details entered into Geoscience Australia's Marine Sediment database <http://www.ga.gov.au/oracle/mars>).

### 4.1.4. Subsurface Sediment Sampling

Subsurface sediments were sampled using an electric-powered vibrocorer (Fig. 4.2c; Table 4.1). The 240V electric cable connected to the vibrating head unit was attached to the coring wire as a lazy line and powered from the vessel. The core frame was held upright on the seabed by three legs that extended outwards and maintained orientation into the current by a fin attached to one of the legs. The core barrels were 0.60 m diameter stainless steel and contained a 0.58 m diameter PVC liner fitted with a core catcher. The empty core liners were 4.5 m long and contained a piston that was tethered to the frame to assist with core recovery. From previous experience, each core was vibrated into the seabed for about 3 mins to achieve maximum penetration. On board, the cores were cut into 0.5 m sections, sealed with end caps (and packed with high-density foam biscuits where necessary), labelled, and stored in a refrigerated container before being transported to Canberra for geophysical logging (see below). The details were entered into the MARS database. In order to fully characterise the Late Quaternary sediments and evolution of the regions, cores were collected from the major sedimentary environments and several locations within the sand ridges and sandwaves.

## 4.2. SAMPLE PROCESSING AND ANALYSIS

### 4.2.1. Water Samples

One litre of water was filtered through pre-weighed 0.45 µm mesh glass filter papers using a vacuum system on board the vessel (Fig. 4.2d). The filter papers were then stored in a dry freezer and on return to the laboratory were oven dried at 60° C and re-weighed to ±0.0001 g to obtain the weight of suspended sediment. Suspended sediment concentrations were then calculated from these weights for the 1 litre of seawater filtered through the paper. Select filter papers were then visually inspected using a standard binocular microscope to provide an assessment of the type and nature of particles in suspension.

### 4.2.2. Digital Video Footage

Approximately 3-5 minutes of video was captured at each site, and 1.5 minutes of video was captured every 20 minutes for the 24-hour stations. At each site, including the 24-hour stations, the video footage recorded was edited down to 20-30 s snippets that showed the major habitats, biota and sedimentary processes that were observed at each station. The video was edited using standard video editing software.

### 4.2.3. Surface Sediments

#### 4.2.3.1. Sediment texture

Initially, the bulk sample was split into two sub-samples for grain size analysis. Bulk grain size distributions were determined for the first sub-sample using a Malvern™ Mastersizer-2000 laser particle size analyser (e.g., Heap et al., 1999). The bulk sample was sieved through a 2 mm mesh to remove the gravel fraction, which was retained for visual inspection. Organic matter in the fine fraction was then removed by immersing the sample in 10-20 ml of dilute hydrogen peroxide (H<sub>2</sub>O<sub>2</sub>). After rinsing thoroughly with distilled water, the sample was placed in an ultrasonic bath for up to 2 mins to break up any remaining aggregates. The grain size distribution of the fine fraction was then determined using the laser particle size analyser.

Approximately 10-20 g of the second sub-sample was sieved through a 2 mm and 63 µm sieve with distilled water. Each size fraction was retained. The mud fraction was spun in a centrifuge at 3,500 rpm for 10 mins to separate out the sample. All of the fractions were dried in an oven at 40° C for at least 24 hours and then allowed to cool to room temperature. The dried material for each fraction was then weighed with an analytical balance to obtain the amount of gravel, sand and mud in the sample.

#### 4.2.3.2. Sediment composition

Carbonate concentrations were determined on all of the bulk samples, as well as the sand and mud fractions using the “carbonate bomb” method of Muller and Gastner (1971). Initially the 3-5 g of bulk sample was dried in an oven at 40° C for 24 hours. This sample was then ground to a fine powder and exactly 0.8 g was reacted with 10 ml of orthophosphoric acid (H<sub>3</sub>PO<sub>4</sub>). The flask was agitated until the entire sample had reacted with the acid (usually about 60 s). The pressure of the gas liberated was then compared to a standard curve that converted the pressure into carbonate concentrations (the curve is constructed by reacting known amounts of pure calcium carbonate between 0.1 – 0.8 g and recording the



corresponding pressure). The carbonate content of the gravel fraction was estimated from a visual inspection for all samples.

Select samples were also visually inspected for composition on board the vessel and in the laboratory using a standard binocular microscope. The bulk, gravel, sand and mud fractions were inspected separately, with only the coarse silt-sized grains visible in the mud fraction. An estimate of the abundance of each constituent in each fraction was made based on a visual assessment of the grains. At the time of writing, no point counting of the grains had been carried out.

#### ***4.2.3.3. Seagrass type and distribution***

The type, distribution and abundance (where possible) of seagrass was determined from samples recovered in the surface sediment grabs and from expert interpretation of the seabed video footage. Both data sets were used to give a representative indication of the habitat and biota in each area. Interpretation and classification of the seabed footage was compromised in some locations by significant near-bed turbidity coupled with “wash-out” caused by too much ambient light; wash-out was particularly bad at stations occupied during the middle part of the day. When this occurred, the video footage could only be used to indicate the presence and absence of seagrass. Seagrasses were identified and classified using a standard reference chart showing the form and structure of major seagrass types known to exist in Torres Strait. Samples collected in the grabs and captured on video were compared to this chart. All interpretation was undertaken on the vessel.

### **4.2.4. Subsurface Sediments**

To characterise the Late Quaternary history comprising the sandwaves wet bulk density, P-wave velocity, fractional porosity, texture, composition, and age of the sediments contained in the cores were determined. The data for each physical property were “cleaned” by a visual inspection of the downcore profiles to remove spurious and bad data caused by logging artefacts (such as those around section breaks) and poor core condition. The archive section of each core was also x-rayed at the local veterinary hospital to reveal internal structures and constituents not visible on the surface.

#### ***4.2.4.1. Physical Properties***

After equilibration with ambient laboratory conditions (between 18° and 20°C), wet bulk density (WBD), P-wave Velocity ( $V_p$ ), and Fractional Porosity (FP) were determined at 0.01 m intervals down VC1-5 using a GEOTEK™ MS2 multi-sensor core logger (e.g., Heap et al., 2001).

Wet bulk density (WBD) was determined by measuring the gamma attenuation of the sediment from a Cs-137 source. WBD of the sediment is positively correlated with gamma attenuation. The relationship between density and gamma attenuation was initially calibrated using a graduated density standard consisting of 13 water/aluminium density components (e.g., Best and Gunn, 1999). This procedure corrects for gamma attenuation (caused by the Al liner), count rate effects (e.g., Weber et al., 1997), and the different scattering properties of seawater and sediment (e.g., Gerland and Villinger, 1995). The calibration was undertaken using a water density of  $1.001 \text{ g cm}^{-3}$ , and aluminium density of  $2.71 \text{ g cm}^{-3}$ , which is approximately equal to the mineral densities of siliciclastic ( $2.65 \text{ g cm}^{-3}$ )



and carbonate ( $2.67 \text{ g cm}^{-3}$ ) grains. Using this calibration, repeat density measurements were within  $0.05 \text{ g cm}^{-3}$ .

P-wave velocity ( $V_p$ ) was determined by measuring the travel time of a 500 kHz ultrasonic compressional pulse across the core. The pulse propagates through the core from the transmitter and is detected by the receiver.  $V_p$  is directly related to changes in the composition and texture of the sediments (e.g., mineral composition, grain shape and size, packing, etc.). To prevent variations in the ambient conditions masking differences between sedimentary units, the  $V_p$  was also corrected for temperature of the water and sediment and salinity of the interstitial fluid for each core.

Fractional Porosity (FP) was calculated directly from the WBD using equation 16:

$$FP = (MGD - WBD) / (MGD - WD) \quad (16)$$

where FP = fractional porosity, MGD = mineral grain density, WBD = wet bulk density, and WD = fluid density (i.e., sea water). This calculation assumes that the sediment was fully saturated with seawater, a mineral density of siliciclastic and carbonate sediment of  $\sim 2.65 \text{ g cm}^{-3}$ , and a fluid (i.e., seawater) density of  $1.024 \text{ g cm}^{-3}$ .

#### 4.2.4.2. Sediment texture

Grain size distributions were determined for bulk samples using a Malvern™ Mastersizer-2000 laser particle size analyser (e.g., Heap et al., 1999). The samples were prepared and analysed using the same methods as those undertaken for the surface samples ([section 4.2.3.1](#)).

Core sub-samples were analysed for percent gravel, sand and mud. Approximately 2-5 g of bulk sediment was washed with distilled water through sieves of mesh sizes of 2 mm and  $63 \mu\text{m}$ . The sub-samples were then treated and analysed using the same methods as those undertaken for the surface samples ([section 4.2.3.1](#)).

#### 4.2.4.3. Sediment Composition:

Carbonate concentrations were determined on the bulk samples, as well as the sand and mud fractions according to the bomb method of Muller and Gastner (1971). The procedure used is the same as that for the surface sediments ([section 4.2.3.2](#)).

#### 4.2.4.4. Sediment Age:

At the time of writing no samples had been collected for radiocarbon age determinations. Samples will be collected from the cores with reference to cores collected during the survey to be undertaken after the trade wind season in October 2004.

### 4.3. RESULTS

#### 4.3.1. Water Samples

Four stations (58, 62, 80, 81) were occupied to measure near-bed suspended sediment concentrations (SSC) in the study areas over a spring and neap tidal cycle (i.e., 25 hours) (see [Fig. 3.1](#)). Station 58, located in Area A, was occupied from 11:00 02/04/2004 until 12:00 03/04/2004 UTC and Station 62, located in Area B, was occupied from 15:40 03/04/2004 until 16:40 04/04/2004 during spring tides. Station 80, located in Area A, was occupied from 08:20

09/04/2004 until 09:20 10/04/2004 UTC and Station 81, located in Area B, was occupied from 11:40 10/04/2004 until 12:40 11/04/2004 UTC during neap tides.

#### 4.3.1.1. Area A:

Near-bed suspended sediment concentrations during spring tides (Station 58) attain a maximum of  $21.9 \text{ mg l}^{-1}$  at 14:00 and 02:20 UTC and a minimum of  $5.1 \text{ mg l}^{-1}$  at 09:40 UTC (Fig. 4.4a). The mean SSC over the tidal cycle is  $13.2 \text{ mg l}^{-1}$ . More than a quarter of the samples (27%) had suspended sediment concentrations of  $>17 \text{ mg l}^{-1}$  and 21 samples (29%) had a SSC of  $<10 \text{ mg l}^{-1}$ . Maximum and minimum concentrations occur approximately 12 hours apart, suggesting a tidal influence. Smaller, short-term fluctuations also occur in the concentrations which are probably related to waves. Between 04:00 and 09:00 UTC these fluctuations in SSC are spaced approximately 1.3 hours apart.

Near-bed suspended sediment concentrations during neap tides (Station 80) are variable with a general reduction over the tidal cycle (Fig. 4.4b). Unlike during spring tides, the concentrations do not show any obvious cyclicity in the data. Maximum concentrations attain  $20.8 \text{ mg l}^{-1}$  at 12:00 UTC and the minimum concentration is  $2.1 \text{ mg l}^{-1}$  at 08:40 UTC. Mean SSC over the tidal cycle is  $11.6 \text{ mg l}^{-1}$ . In comparison to the record for spring tides, a total of 7 samples (9.6%) have a SSC of  $>17 \text{ mg l}^{-1}$  and 24 samples (33%) have a SSC of  $<10 \text{ mg l}^{-1}$ . The reduction in concentrations during the tidal cycle appears as a series of steps from 08:20 to 13:40 UTC (mean =  $16.7 \text{ mg l}^{-1}$ ), from 14:20 to 03:40 UTC ( $11.6 \text{ mg l}^{-1}$ ), and from 04:00 to 09:20 UTC ( $6.4 \text{ mg l}^{-1}$ ). If the last four observations, where significant variability occurs in the last part of the tidal cycle, are removed the mean SSC for this period drops to  $5.9 \text{ mg l}^{-1}$ .

#### 4.3.1.2. Area B:

Near-bed suspended sediment concentrations during spring tides (Station 62) attain a maximum of  $31.2 \text{ mg l}^{-1}$  at 15:00 UTC and a minimum of  $8.9 \text{ mg l}^{-1}$  occur at 17:20 UTC (Fig. 4.4c). The mean SSC over the tidal cycle is  $18.31 \text{ mg l}^{-1}$ . This station had the highest average SSC with only 3 samples having concentrations of  $<10 \text{ mg l}^{-1}$ . Maximum and minimum concentrations occur approximately 12-13 hours apart, suggesting a tidal influence like that shown in the data for Area A. The concentrations show gradual rise to a peak and then a rapid decline. The first peak in SSC is broader occurring between 20:00 and 03:40 UTC (~5.6 hours) and comprises of 15 observations where concentrations were  $>20 \text{ mg l}^{-1}$ . The second peak is narrower, occurring between 13:00 and 15:40 (~2.6 hours) and comprising 9 observations where concentrations were  $>20 \text{ mg l}^{-1}$ .

Near-bed suspended sediment concentrations during neap tides (Station 81) are variable with a general reduction over the tidal cycle (Fig. 4.4d). Unlike during spring tides, the concentrations do not show any obvious cyclicity in the data. Concentrations attain a maximum of  $15.4 \text{ mg l}^{-1}$  at 11:20 UTC and a minimum of  $3.1 \text{ mg l}^{-1}$  at 16:00 UTC. The mean SSC over the tidal cycle is  $8.9 \text{ mg l}^{-1}$  which is the lowest of all the stations occupied. The concentrations record a period of rapid increase followed by a period of gradual decline. An extended period of low concentrations below  $6 \text{ mg l}^{-1}$  occurs in the record between 14:20 and 19:40 UTC (~5.3 hours), followed by a sharp rise in concentrations to  $11\text{--}13 \text{ mg l}^{-1}$ , and then decrease to a minimum of  $4.2 \text{ mg l}^{-1}$  at 08:00 UTC. The last part of the record is characterised by a relatively rapid rise in suspended sediment concentrations after 08:00 to  $15.4 \text{ mg l}^{-1}$  at 11:20 UTC and lasting until 12:40 UTC.

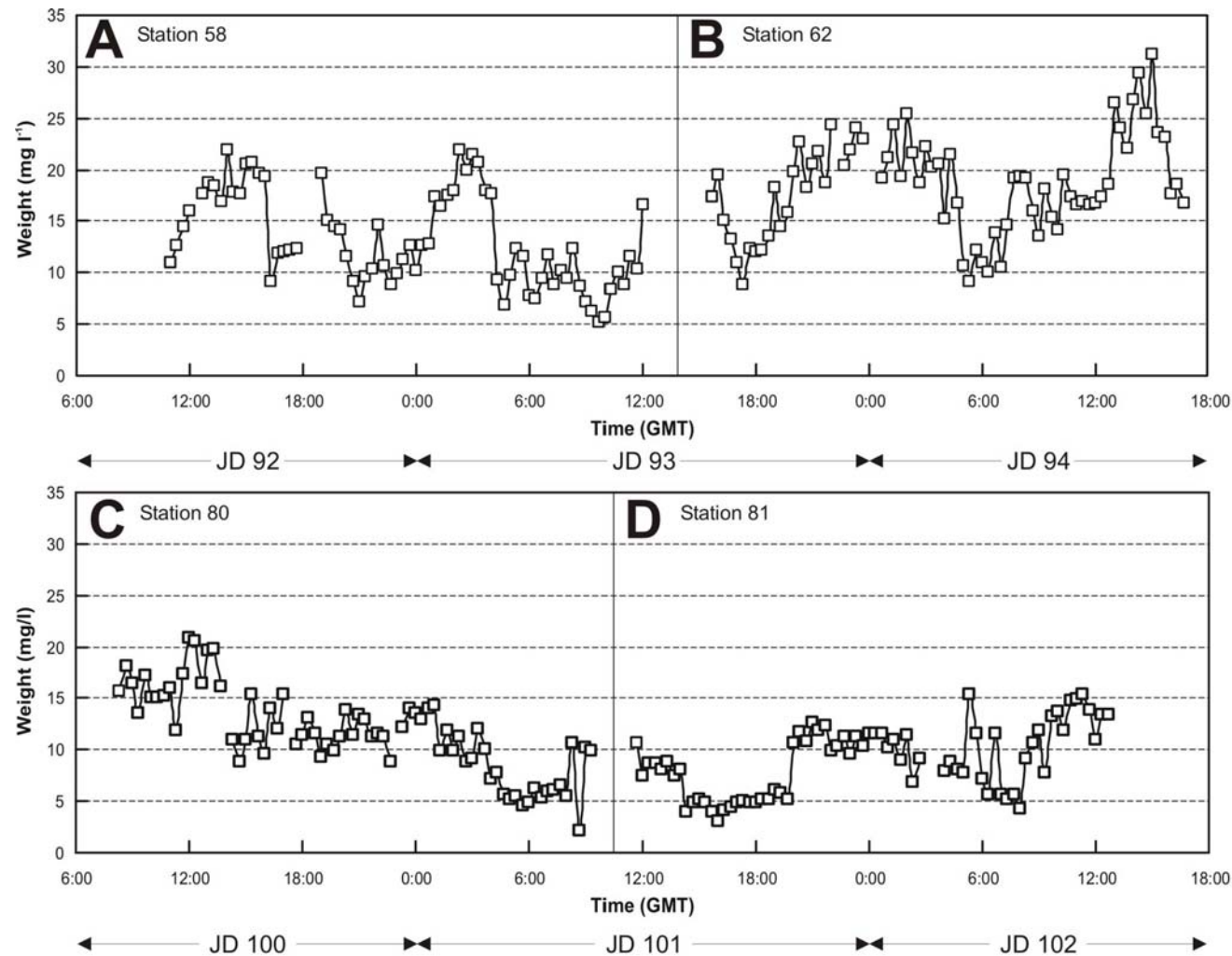


Figure 4.4. Graphs showing suspended sediment concentrations for: a) station 58, b) station 62, c) station 80, and d) station 81. Stations 58 and 80 were located in Area A and stations 62 and 81 were located in Area B. Stations 58 and 62 were occupied during neap tides and 80 and 81 were occupied during spring tides. Highest near-bed SSC's occurred during neaps where the tide was observed to run from LLW to HHW. While the most sediment was suspended by waves, the time-series show a distinct tidal influence with peaks in SSC's approximately 12 hours apart. These peaks correspond to peaks in the near-bed tidal current velocity (see Fig. 3.13 & 3.15 respectively).

### 4.3.2. Digital Video Footage

Video footage was recorded at a total of 60 camera stations (Fig. 4.5; Table 4.1). A total of 11 stations (5, 7-12, 14, 34, 50, 73) in the regional survey, 41 stations (13, 15, 18, 29-33, 35-49, 51-57, 67-70, 73-79) in Area A, and 8 stations (6, 19, 21-26) in Area B were occupied. Overall the digital video captured is of high to reasonable quality, although visibility is significantly compromised due to high turbidity at stations 67-70 and 73-79. The 20-30 s snippets of the video footage recorded at each station are located in Appendix F. The digital video tapes containing the entire video recordings can be viewed on request from Geoscience Australia.

#### 4.3.2.1. Regional Survey:

Greatest variability in seabed habitats and sedimentary environments occurs across the regional camera stations. In the regional survey, sedimentary environments on the seabed include partially-cemented hard-grounds, algal and coral reefs, and sedimented areas comprised of calcareous muddy gravelly sand and coral rubble. Macro-algae (*Sargassum* sp.) was observed at all locations except stations 9 and 34 where no benthic biota were observed, although the cover ranged from sparse to patchy to abundant at the other stations. Seagrasses were observed at only 5 stations (7-8, 10, 50, 73), and these stands were mostly sparsely distributed. Other biota observed included sponges, soft corals, echinoids, hard corals, fish and gorgonians in decreasing order of abundance. Small sandwaves and ripples were observed at station 34, with bedload transport visible at stations 34 and 73.

#### 4.3.2.2. Area A:

Significant variability in seabed habitats and sedimentary environments was observed in the camera stations in Area A. Sedimentary environments and habitats on the seabed include algal and coral reefs located on the surfaces of the marginal platforms, hard-grounds and sedimented areas characterised by calcareous muddy medium to coarse sand. Most variability in seabed character was observed on the marginal platforms, where the seabed was generally uneven and rough in places with numerous rocky outcrops interspersed with sedimented areas and coral rubble. Between the marginal platforms, the seabed was generally flat to undulating with gentle slopes. Possible evidence for bioturbation was observed from this area as pock marks, pits and mounds up to a few centimetres in diameter in some stations. Macro-algae (*Sargassum* sp.) was observed at nearly all the stations and the cover ranged from sparse to abundant. Other biota observed included sponges, seagrass, hard corals, soft corals, fish and echinoids in decreasing order of abundance. Seagrasses formed relatively large contiguous patches on the sedimented areas (52-54, 56) and formed more isolated stands interspersed with algal stands on the algal and reefal platforms (e.g., 13, 47-49, 51). Greatest diversity of biota was observed on the algal and coral reefs of the marginal platforms, where sponge gardens (33, 56, 78), hard and soft corals (13, 30, 32, 52, 56, 77) and numerous fishes and echinoids (40, 48) were observed. In the vicinity of the sand ridges, the biota was less abundant and dominated by filamentous brown algae (13, 29-33, 35, 40). Sandwaves and sand ripples were observed at stations that were characterised by unconsolidated sediment (31, 33, 35). Bedload transport was observed at numerous stations throughout the area (29, 36, 38-39, 41-42, 47, 51, 54, 73-74). Significant turbidity was observed in the southern regions (67-70, 73-79). These elevated levels were probably associated with strong tidal currents due to the timing of these stations during neap tides (JD100), where the tide was observed to run unabated from LLW to HHW age (Fig. 3.6).



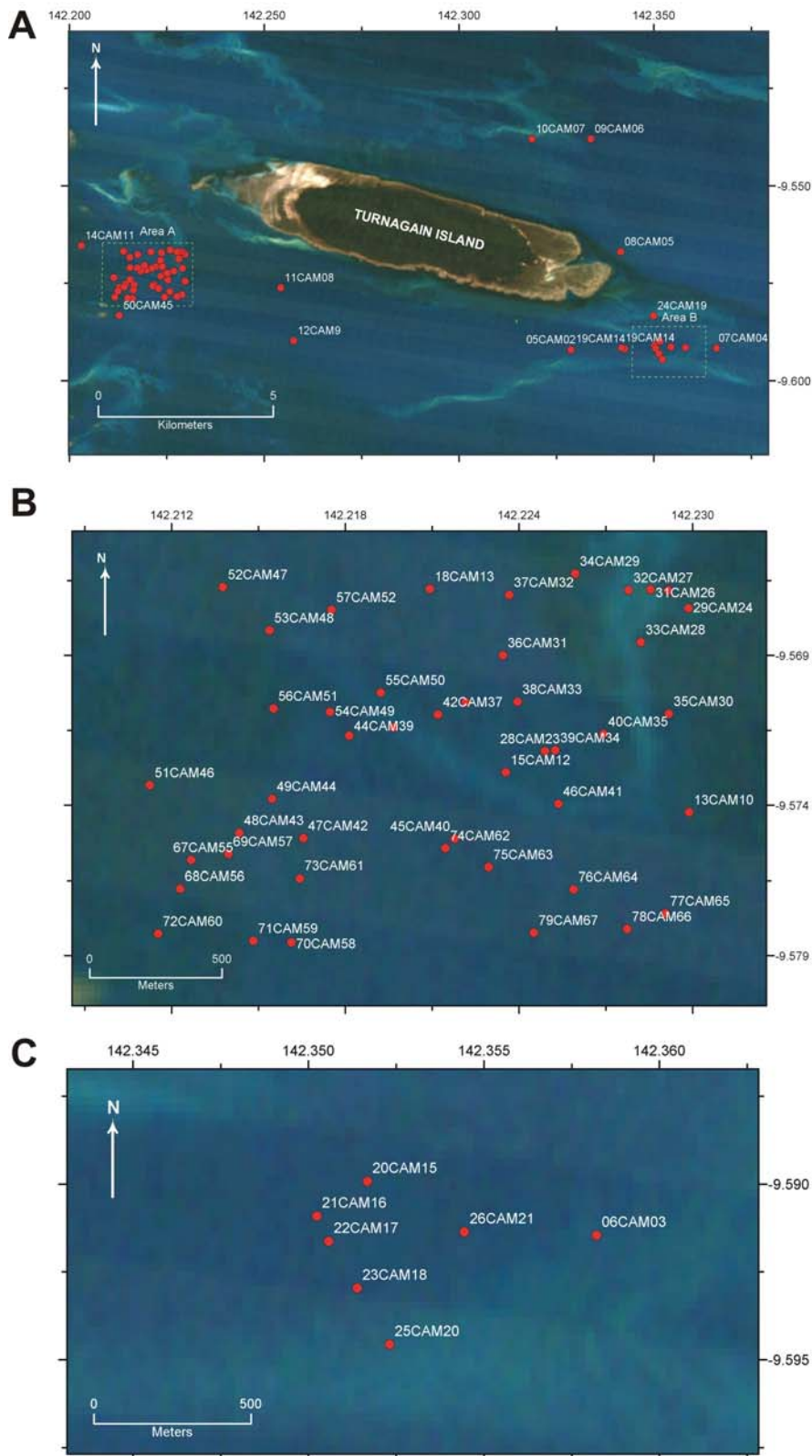


Figure 4.5. Map showing location of camera stations for: a) regional, b) Area A, and c) Area B sites. A total of 60 camera stations were occupied during the survey. Approximately 3-5 mins of video footage was collected at each station. Basic notes were made on the sediments, morphology and biota/habitats on the seabed at each location. The video has been condensed to 20-30 s snippets that depict the major features and can be found in Appendix F.



#### 4.3.2.3. Area B:

Least variability in seabed habitats and sedimentary environments occurs in the Area B camera stations. Sedimentary environments and habitats on the seabed include sedimented areas comprised of unconsolidated calcareous gravelly medium to coarse sand, partially cemented hard-grounds, algal beds, and coral rubble. The rubbly areas contained cobble- and pebble-sized clasts of hard coral and partially-cemented limestone (24). The seabed at each station was generally smooth to undulating with gentle slopes. Macro-algae (*Sargassum* sp.) was observed at nearly all sites except station 25, where no biota were observed. This site was characterised by strong currents and coarse bed sediment. Other biota observed include seagrasses, gorgonians and fish (6, 21-24, 26). Seagrasses formed isolated stands interspersed with algal stands. Although the cover of biota was generally good, the biota in Area B was less abundant than that observed in the regional stations and Area A.

#### 4.3.2.4. 24-Hour Stations:

Video footage recorded during the 24-hour stations captured significant bedload transport in the vicinity of the sand ridges in Area A and sandwaves in Area B. The transport of the grains along the seabed occurred during both neap and spring tides. Although bedload transport occurred throughout the tidal cycle probably due to tidal currents, most of the grains were transported along the bed in pulses that moved in association with passing waves (e.g., see [Appendix F](#); 80CAM0640; 81CAM2220). Grains of all sizes were observed to move in these pulses. Only the finer grains were observed to move under the influence of tidal currents.

### 4.3.3. Surface Sediments

This section describes grab and core top samples recovered from the two survey areas. Samples are described in terms of their texture and composition providing insights into the nature of seabed. A total of 71 grabs (GR1-GR71) were collected over the two study sites that broadly characterise the texture and composition of the seabed sediments and associated habitats ([Fig. 4.6](#); [Table 4.1](#)). Seabed sediment samples in Area A and B contain mud, sand and gravel, and are dominated by carbonate material. Seagrass is also an important constituent of some samples collected from Area A, and is evident in the video footage of regions in Area B. Texture and composition information for the surface samples are contained in [Appendix G](#).

#### 4.3.3.1. Area A

*Folk Classification:*— Sediment making up the hard-grounds located between the reef platforms is generally comprised of poorly-sorted, muddy sand and gravel. The ridge that extends across the central regions consists of poorly-sorted slightly muddy sand and gravel. Sediments on the reef platforms comprise poorly-sorted muddy medium to coarse sand, with minor amounts of gravel, and gravelly sand. In general, sediments in Area A are made up of foraminifera, mollusc, bryozoan, and *Halimeda* fragments with minor amounts of sponge spicules and lithic fragments. Some samples also contain hard coral fragments, and weathered and cemented limestone clasts encrusted with worm tubes. Samples recovered from the sand ridge and reef platforms contained minor amounts of seagrass.

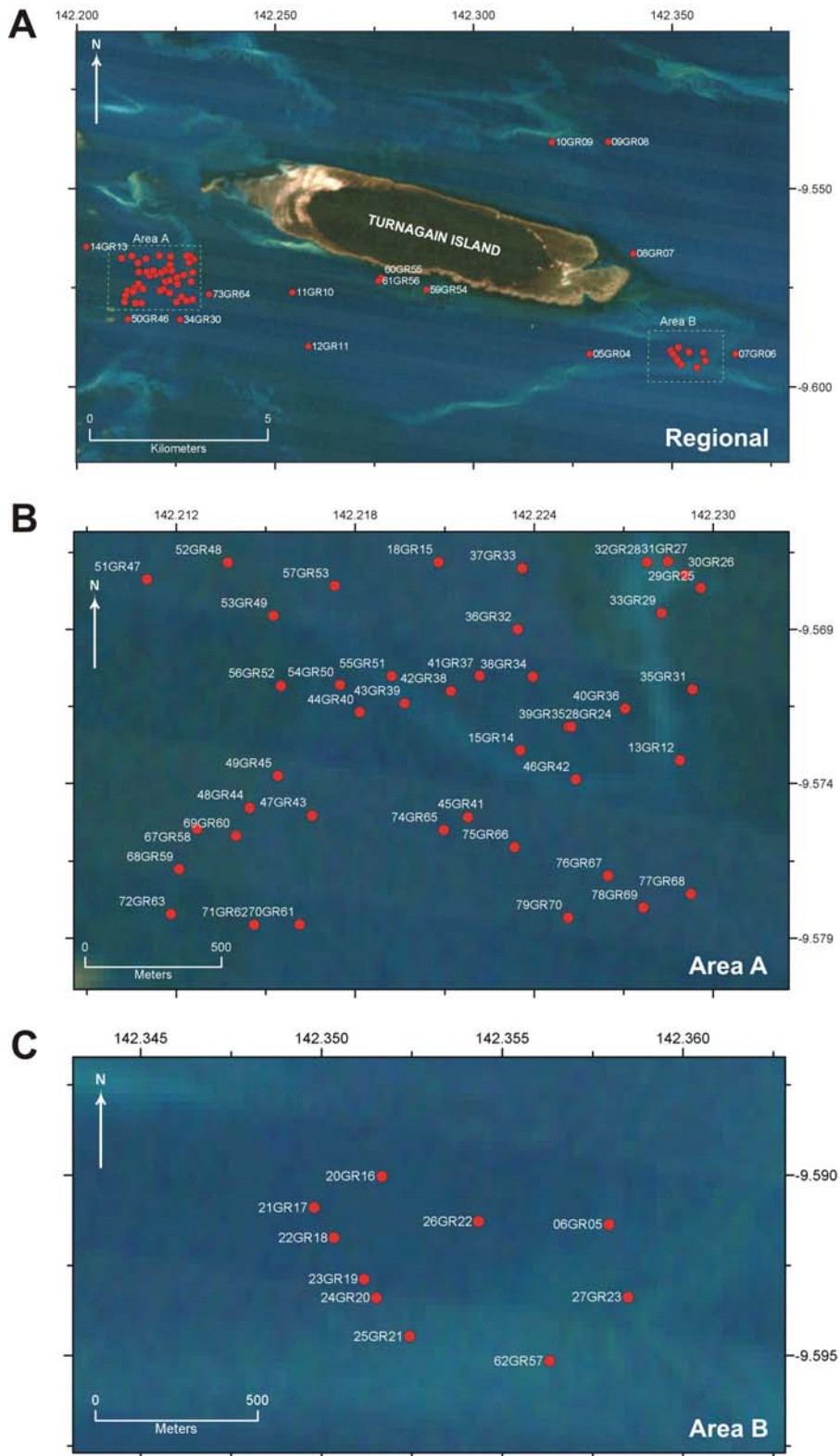


Figure 4.6. Map showing location of grab samples for: a) regional, b) Area A and c) Area B sites. A total of 71 grabs were collected during the survey. Basic visual descriptions of the sediments and biota were conducted on the vessel.

*Gravel:*— Gravel concentrations range from 8.99% to 65.64%. Higher gravel concentrations are generally associated with higher sand concentrations. Highest concentrations of 41.32-65.64% occur on the reef platforms (e.g., 29GR25, 31GR27) and hard-

grounds (e.g., 79GR70, 78GR69) (Fig. 4.7a). Lowest concentrations occur locally in the north of the eastern reef platform (30GR26). On the mobile sand ridge, gravel concentrations range from 14.59% to 35.05%. The gravel fraction is made up of mollusc shells and fragments (e.g., 38GR34, 47GR43), bivalve fragments (e.g., 18GR15), foraminifer tests (e.g., 32GR28, 57GR53), bryozoans (e.g., 38GR34), *Halimeda* flakes (e.g., 77GR68, 79GR70), terrigenous clasts (e.g., 36GR32, 31GR27, 35GR31), cemented limestone (e.g., 35GR31), coral fragments (e.g., 45GR42), carbonate pebbles (e.g., 74GR65) and encrusted carbonate fragments (e.g., 72GR63, 77GR68). The carbonate component of the gravel fraction generally has a fresh to intermediate preservation.

*Sand:*— Sand is the dominant size fraction in all samples recovered from Area A. Sand concentrations range from 34.09% to 88.25%, but are mostly between 60–70% (Fig. 4.7b). Highest concentrations occur on the hard-grounds in the north (e.g., 57GR53). The concentration of sand generally increases with the concentration of gravel. The lowest sand concentration of 34.09% occurs on the hard-grounds in the south (79GR70). On the mobile sand sheet, sand concentrations are generally higher than the surrounding seabed with concentrations over >60%. The sand fraction is comprised of a variety of constituents including mollusc and bryozoan fragments, foraminifera tests, *Halimeda* flakes and small amounts of lithic fragments. The carbonate component of the sand fraction generally has an intermediate preservation.

*Mud:*— The mud fraction makes up a relatively small amount of the seabed samples recovered from Area A and displays least variability across the area. Mud concentrations range from 0.04% to 17.99% (Fig. 4.7c). Lower mud concentrations occur where there is higher sand and gravel concentrations. Highest mud concentrations occur next to the reef platform in the west. Samples in this region contain between 15.27% and 17.99% mud (e.g., 71GR62). Lowest mud concentrations occur on the reef platform and hard-grounds. Here, seabed sediments contain between 0.04% and 0.69% mud (e.g., 32GR28, 52GR48, 57GR53, 79GR70). The mud fraction mostly consists of calcareous fragments and the silt-sized grains observed under the microscope are mostly foraminifer tests and mollusc fragments.

*Carbonate (Bulk):*— In Area A, bulk carbonate concentrations are >50% for all samples, and samples comprising >80% carbonate were recovered from all seabed environments (Fig. 4.7a). Highest bulk concentrations of >90% occur on the reef platforms and sand ridge. Lowest bulk carbonate concentrations of <54% occur between the reef platforms on the hard-grounds in the north. In Area A, the carbonate material is made up mostly of mollusc fragments, foraminifer tests and bryozoan fragments, with smaller amounts of *Halimeda* flakes and coral fragments. Distinctively, reefal deposits such as calcareous nodules and cemented limestone fragments are common constituents, especially of the gravel fraction.

*Carbonate (Sand):*— The carbonate sand fraction displays the highest concentrations and shows least variation across Area A, ranging from 88.2% to 96.3% (Fig. 4.8b). Because the seabed is dominated by calcareous sediments, carbonate sand concentrations show a strong correlation with sand concentrations (compare Figs. 4.7b and 4.8b). For example, high carbonate sand concentrations located on the eastern reef platform and the sand ridge correspond to high sand concentrations in those areas. Highest carbonate sand concentrations occur in the interior of the eastern reefal platform (e.g., 65VC05/0-2). Lowest carbonate sand concentrations occur on the hard-grounds where the sand content is highly variable. The carbonate sand fraction is made up mostly of benthic foraminifer tests, mollusc and bryozoan fragments, polychaete worms and *Halimeda* fragments (e.g., 13GR12, 15GR14).



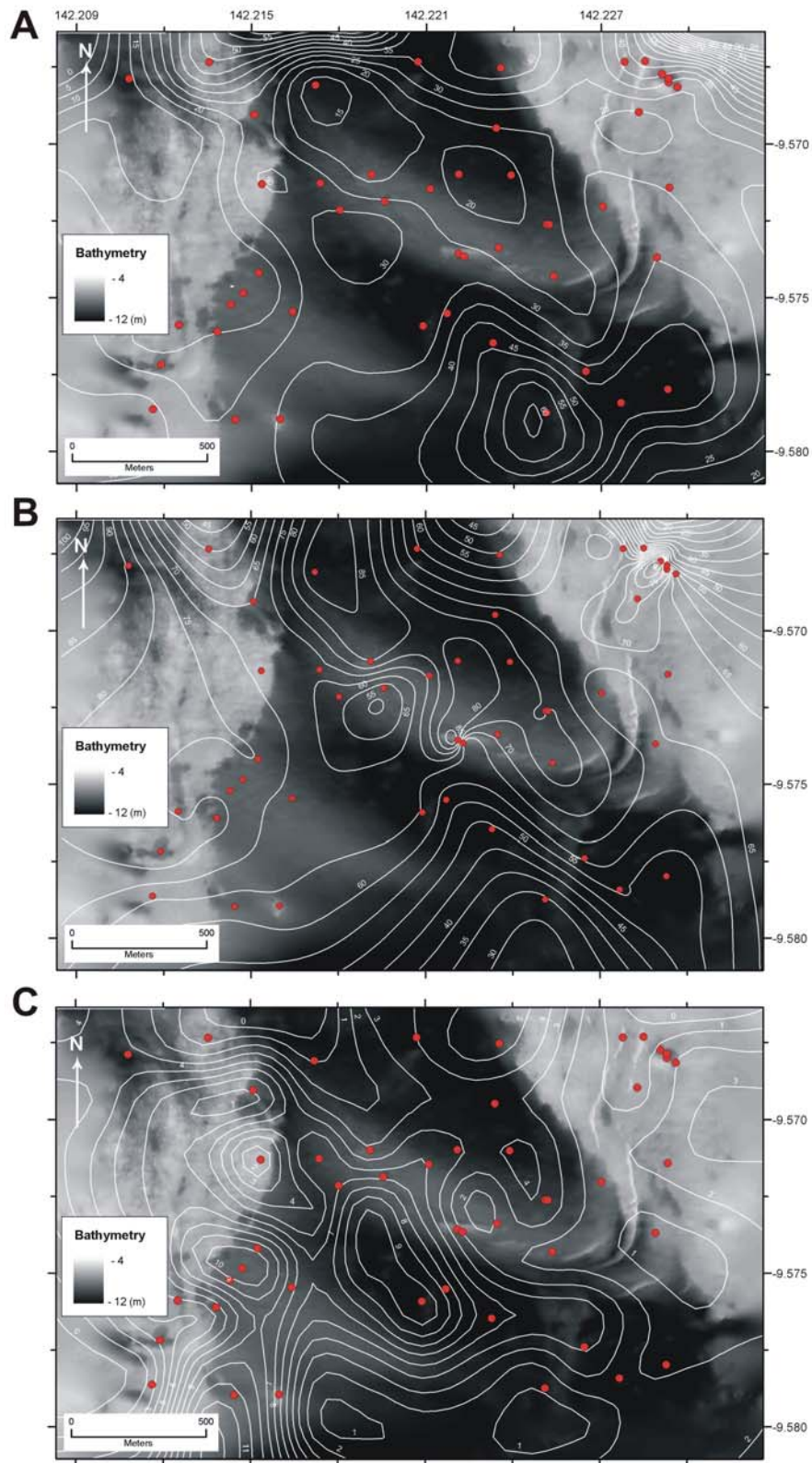


Figure 4.7. Maps showing: a) %Gravel, b) %Sand and c) %Mud from the surface sediments in Area A. Sand and gravel are the dominant size fractions, with very little mud present. See text for full details. Textural and compositional data for the samples are reported in Appendix G.

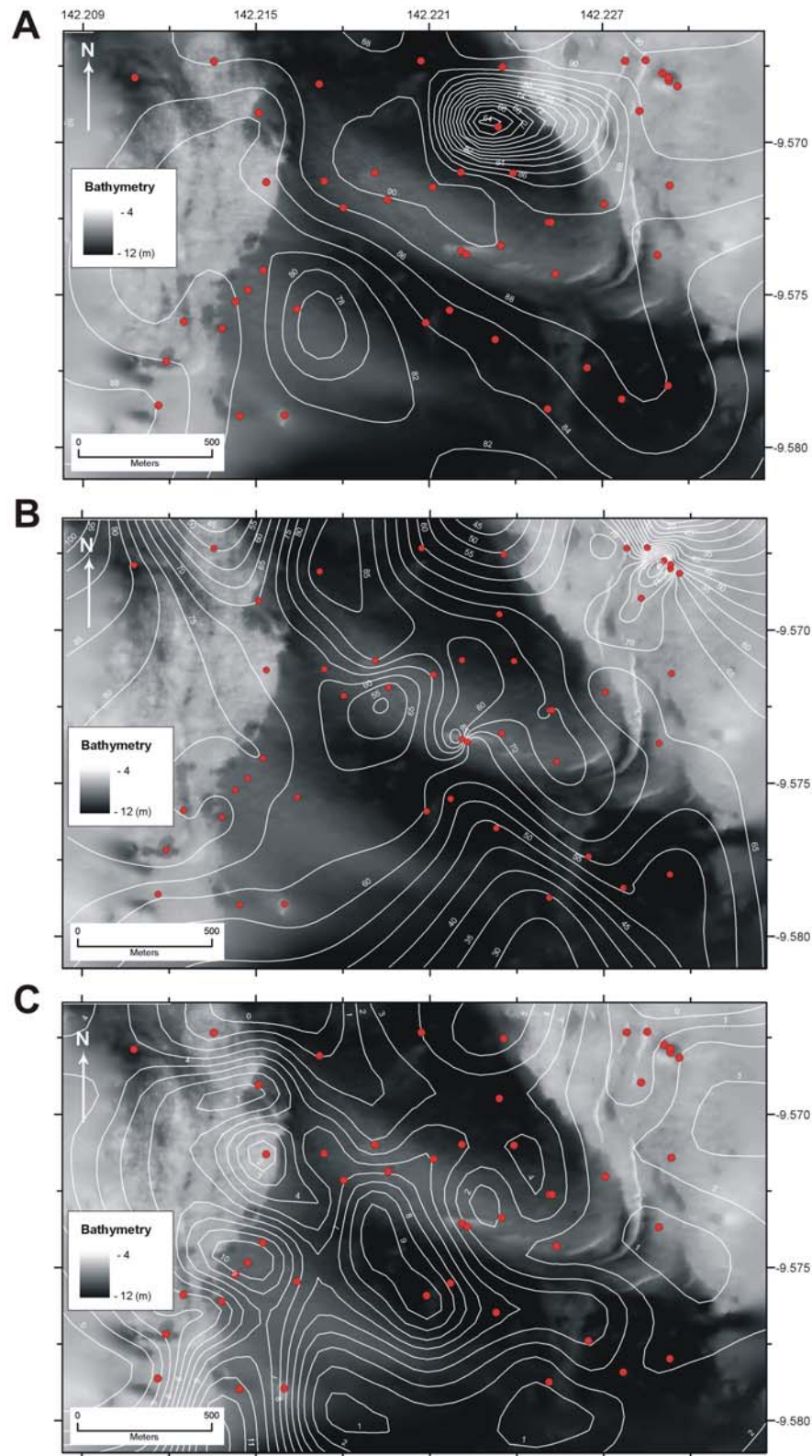


Figure 4.8. Maps showing: a)  $\%CaCO_3$  (Bulk), b)  $\%CaCO_3$  (Sand), and c)  $\%CaCO_3$  (Mud) from the surface sediments in Area A. Carbonate is by far the dominant fraction of the sediments for all size fractions. See text for full details. Textural and compositional data for the samples are reported in Appendix G.



*Carbonate (Mud):*— Carbonate mud concentrations range from 68.9% to 74% and show only slight variation across Area A (Fig. 4.8c). Highest concentrations of >70% occur on the hard-grounds in the north (e.g., 70GR61). Lowest concentrations of 67.9% occur on the hard-grounds and also on the sand ridge (e.g., 37GR33, 43GR39). Concentrations of >72% occur on the western reef platform. Carbonate mud is not a major component of seabed sediment in Area A with more than half of the samples containing insufficient quantities for analysis. A visual inspection of the carbonate mud fraction by microscope indicates that the silt-sized grains are mostly comprised of foraminifer tests, mollusc fragments and *Halimeda* fragments.

#### 4.3.3.2. Area B

*Folk Classification:*— Sediments making up the hard-grounds between the sandwaves are poorly-sorted calcareous sandy gravel. Sediments on the sand sheet surrounding the sandwaves and making up the sandwaves themselves are well- to moderately-sorted calcareous medium to coarse sand, with local occurrences of calcareous gravel. Larger clasts including cobbles and pebbles are also locally present in the sand sheet. In general, sediments in Area B are made up of mollusc fragments, foraminifer tests, bryozoans with minor amounts of coral fragments, *Halimeda*, rhodoliths, sponge spicules and terrigenous clasts.

*Gravel:*— Gravel concentrations range from 2.96% to 89.54% (Fig. 4.9a). Higher gravel concentrations are generally associated with lower sand concentrations. Gravel concentrations display a slight correlation with sedimentary environment, with higher concentrations located on the hard-grounds and sand sheet. Highest concentrations of 64.39% and 89.54% occur in areas bordering the sand sheet and on the edge of the sandwaves (e.g., 22GR18, 24GR20). Sample 22GR18 contains cobble-sized clasts of encrusted coralline algae. Lowest gravel concentrations of 2.96-34.66% occur on the sandwaves (e.g., 27GR23, 62GR57). The gravel fraction is made up of reef detritus including mollusc and coral fragments (e.g., 25GR21), encrusted bryozoans (e.g., 26GR22) and limestone clasts (e.g., 20GR16). The gravel clasts are commonly encrusted with worm tubes and coralline algae. Many clasts are also iron-stained and show evidence of significant oxidation. Rhodoliths were also present in some samples (e.g., 05GR04). The carbonate component of the gravel fraction generally has an intermediate to relict preservation.

*Sand:*— Sand is the dominant size fraction in all samples recovered from Area B. Sand concentrations range from 9.36% to 97.03% (Fig. 4.9b). Higher sand concentrations occur in regions with lower gravel concentrations. The highest sand concentrations of >92% occur on the sandwaves. Lowest sand concentrations occur on the hard-grounds, where the concentrations are markedly lower, being <45%. North of the main sandwave field sand concentrations are comparable to the gravel concentrations (compare Figs. 4.9a and 4.9b). High sand concentrations occur on the sandwaves, with more variability associated with the hard-grounds and sand sheet. The sand fraction is mostly made up of mollusc fragments, foraminifer tests with smaller amounts of bryozoans, *Halimeda*, coral fragments and lithic clasts.

*Mud:*— The mud fraction makes up a relatively small amount of the seabed sediment in Area B (Fig. 4.9c). Mud concentrations are between 0.01% and 4.23% and show slight variation across the area. Lowest concentrations of mud correspond with highest concentrations of sand and lowest concentrations of gravel (compare Figs. 4.9a-c). Lowest concentrations occur in the vicinity of the sandwaves, although sample 23GR19, which

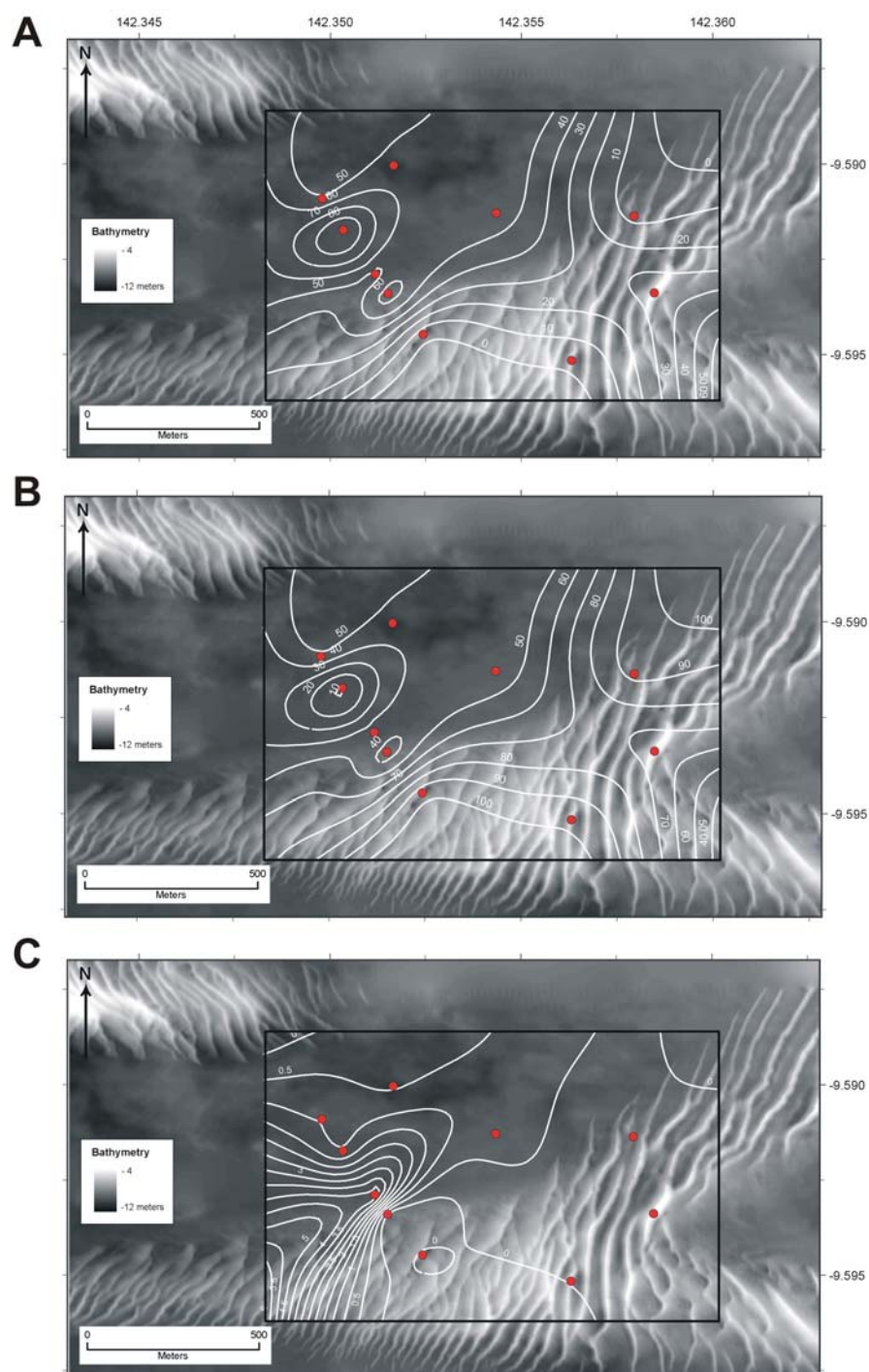


Figure 4.9. Maps showing: a) %Gravel, b) %Sand and c) %Mud from the surface sediments in Area B. Sand and gravel are the dominant size fractions, with very little mud present. See text for full details. Textural and compositional data for the samples are reported in Appendix G.

borders the sandwaves, has the highest concentration of 4.23%. A visual inspection of the mud fraction with a microscope indicates that the silt-sized clasts are mostly mollusc fragments and foraminifer tests.

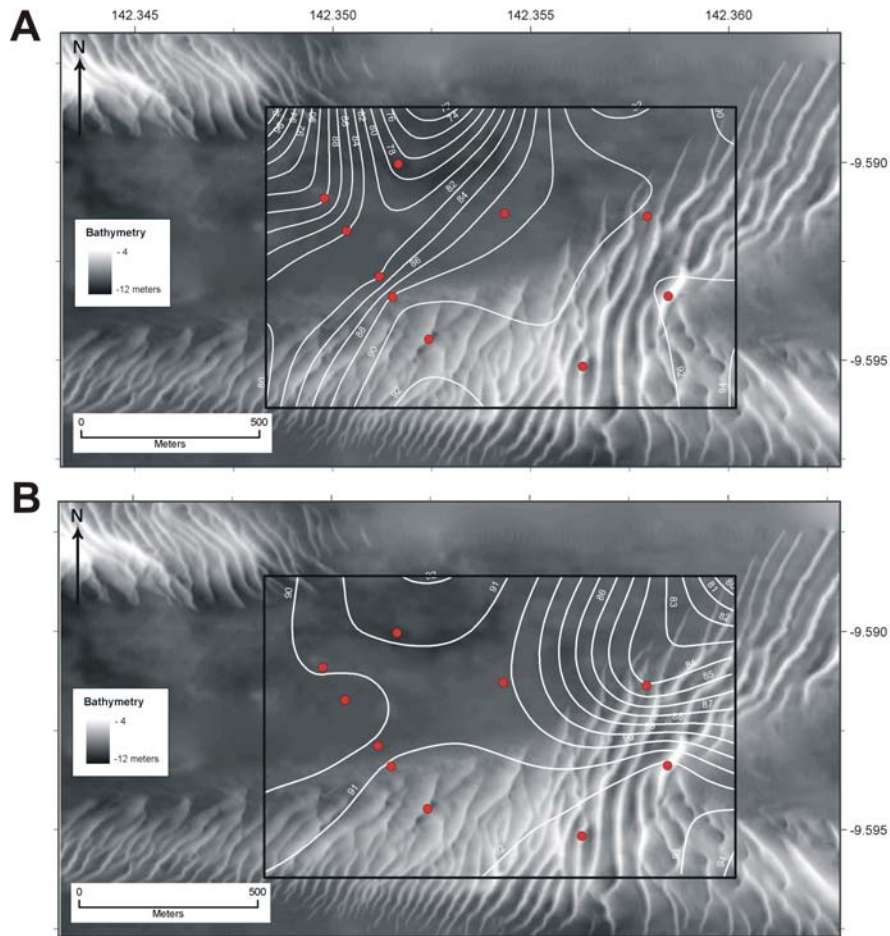


Figure 4.10. Maps showing: a) %CaCO<sub>3</sub> (Bulk) and b) %CaCO<sub>3</sub> (Sand) from the surface sediments in Area B. Carbonate is by far the dominant fraction of the sediments for all size fractions. Only one sample contained sufficient CaCO<sub>3</sub> Mud for analysis. See text for full details. Textural and compositional data for the samples are reported in Appendix G.

*Carbonate (Bulk):*— In Area B, bulk carbonate concentrations are >77% for all samples, and samples comprising >90% carbonate were recovered from the sandwaves (Fig. 4.10a). High bulk carbonate concentrations correspond to high sand concentrations. On the sand sheet, bulk carbonate concentrations range from 82.1% to 88.2%. Lowest concentrations of 77% occur on the hard-grounds. The carbonate fraction consists of mollusc fragments, foraminifer tests and bryozoan fragments with smaller amounts of coral fragments and *Halimeda* flakes. Also present in three samples (21GR17, 23GR19, 22GR18) are pebble-sized rhodolith clasts. The carbonate fraction has an intermediate preservation and contains both fresh and relict components with the fresh component dominating slightly. The relict clasts are heavily encrusted with coralline algae and worm tubes.

*Carbonate (Sand):*— Concentrations of carbonate sand range from 84.1 to 92.3% and are relatively uniform across the area (Fig. 4.10b). The most significant variations in carbonate sand concentrations occur from the crest to the trough of the sandwaves. For example 27GR23 which was recovered from the crest of a sandwave has a concentration of 92.3%,

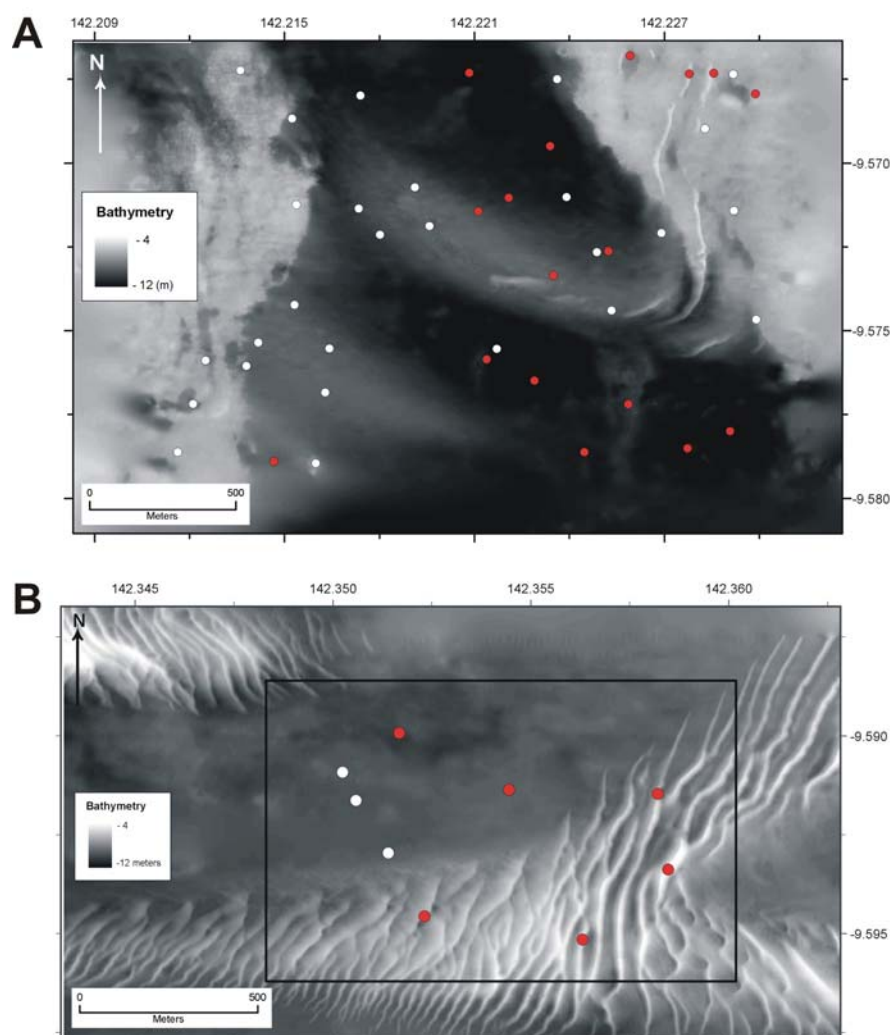


Figure 4.11. Map showing the location of seagrass in a) Area A and b) Area B. Stations where seagrass was observed are denoted by the white coloured circles. The locations represent regions where seagrasses were observed either in the camera or sampled directly from the grab samples. While seagrasses occurred throughout the study area, they were most abundant on the marginal platforms in Area A interspersed with algal beds. Seagrasses were least abundant and formed least contiguous beds in the vicinity of the sand ridges and sandwaves. The types of seagrasses present at each location are presented in Table 4.2.

while sample 06GR05 which was recovered from a trough has a concentration of 84.1%. Carbonate sand is mostly composed of mollusc fragments, foraminifer tests, *Halimeda* flakes and bryozoans.

*Carbonate (Mud):*— Carbonate mud is a very minor constituent of the sediments in Area B. Only one sample (23GR19) contained enough carbonate mud for analysis and yielded a concentration of 67.9%. A visual inspection under the microscope revealed that the silt-sized grains are mostly mollusc fragments and foraminifer tests.

#### 4.3.4. Seagrass Types and Distributions

Seagrass was observed at a total of 37 stations, either in the underwater video footage or contained in the surface grab (Fig. 4.11; Table 4.2). Seagrass was observed in both the video



and grab at only 14 stations. A total of eight seagrass species were observed in the study areas.

Table 4.2. Distribution and types of seagrasses in Areas A and B.

Station	Seagrass*								Total
	Cs	Cr	Hd	Ho	Hs	Hu	Si	Th	
8CAM05		x		x		x	x	x	5
11CAM08	x			x	x		x		4
13CAM10				x	x				2
14CAM11	x			x	x		x		4
19CAM14	x						x		2
21CAM16	x								1
22CAM17	x			x					2
23CAM18	x			x					2
24CAM19	x			x			x		3
28CAM23	x						x		2
30CAM25	x			x	x				3
35CAM30			x	x	x				3
37CAM32	x								1
38CAM33	x			x					2
40CAM35	x								1
43CAM38				x	x				2
44CAM39	x		x						2
45CAM40			x						1
46CAM41					x				1
47CAM42	x								1
48CAM43	x								1
49CAM44	x								1
50CAM45	x		x		x		x		4
51CAM46			x		x		x		3
52CAM47	x		x	x	x		x		5
53CAM48	x		x	x	x		x		5
54CAM49	x		x	x	x				4
55CAM50			x	x					2
56CAM51			x	x	x		x		4
57CAM52	x				x				2
68CAM56	x								1
69CAM57	x						x		2
70CAM58	x			x		x	x		4
73CAM61	x			x					2
<b>Total CAM</b>	<b>25</b>	<b>1</b>	<b>10</b>	<b>18</b>	<b>14</b>	<b>2</b>	<b>13</b>	<b>1</b>	
8GR07		x				x	x	x	4
30GR26	x								1
33GR29					x				1
35GR31			x						1



40GR36	x						x		2
43GR39				x					1
47GR43	x								1
49GR45	x								1
67GR58			x			x			2
70GR61				x		x	x		3
72GR63							x		1
<b>Total GR</b>	<b>4</b>	<b>1</b>	<b>2</b>	<b>1</b>	<b>2</b>	<b>3</b>	<b>4</b>	<b>1</b>	
<b>Occurrences</b>	<b>25</b>	<b>1</b>	<b>11</b>	<b>18</b>	<b>15</b>	<b>3</b>	<b>15</b>	<b>1</b>	

\* Cs = *Cymodocea serrulata*, Cr = *Cymodocea rotundata*, Hd = *Halophila decipiens*, Ho = *Halophila ovalis*, Hs = *Halophila spinulosa*, Hu = *Halodule uninervis*, Si = *Syringodium isoetifolium*, Th = *Thalassia hemprichii*.

The seagrass *Cymodocea serrulata* is the most common type and was observed at 25 stations, followed by *Halophila ovalis* (18), *Halophila spinulosa* and *Syringodium isoetifolium* (15) and *Halophila decipiens* (11). The seagrasses *Cymodocea rotundata* and *Thalassia hemprichii* are the least abundant and were each observed at one station.

Seagrass is present in all environments in Areas A and B, but most commonly occurs on the reef platforms and sand ridge in Area A. Seagrass was less prominent in the video footage and samples collected from Area B. In Area B, seagrass was observed mostly on the hard-grounds in between the sandwave fields. Station 23, located on the edge of the sandwaves contained abundant seagrass.

The seagrasses observed on the seabed in Areas A and B are generally found throughout Torres Strait and far-north Queensland coastal waters (Coles et al., 2004). Coverage of the bed is variable and interspersed with stands of the micro-algae *Sargassum* sp. The seagrass beds are mostly sparse to patchy. The seagrasses observed in Areas A and B are known to part of the diet of dugong in Torres Strait and the relatively soft seabed in these regions makes them potential dugong feeding grounds.

### 4.3.5. Subsurface Sediments

A total of 8 vibrocores were recovered during the survey (Fig. 4.12; Table 4.3). The core logs are presented in Appendix H and the core photos and x-rays are contained on the accompanying CD. The 5 cores (VC1-VC6) that were logged had a total length of 4.17 m and were all recovered from Area A. The cores ranged in length from 0.32 m (VC2) to 1.29 m (VC3). The other 2 cores (VC7-VC8) contained sediment only in the core catchers and were not logged for physical properties. Texture and composition information for the subsurface samples are contained in Appendix I.

#### 4.3.5.1. Physical Properties

In all cases the P-wave velocities are lower than expected for marine sediments of this type. The low velocities are probably caused by numerous air spaces in the sediment. The airspaces have probably formed from water draining or evaporating from coarse unconsolidated sediment and the values and trends must be treated with caution. Low magnetic susceptibility values are the result of the overwhelming dominance of carbonate sediment and indicate very little terrigenous input. As such, any trends must be interpreted with extreme caution as they may reflect instrument drift.



Figure 4.12. Map showing the location of the vibrocores. The vibrocores were located on the crests of the sand ridges in Area A and prominent sandwaves in Area B to sample any internal bedding surfaces that could depict historical changes in the orientation of the dunes, and to provide samples for analysis of physical properties of the sediment. No internal structures or changes in texture and composition were observed in the cores. Details of the vibrocores recovered during the survey are located in Table 4.3. The core logs are provided in Appendix H and textural and compositional data for the sub-surface samples are reported in Appendix I.

Table 4.3. Details of vibrocores recovered during the survey.

Core	Latitude	Longitude	Water Depth (m)	Length (m)
VC1	-9° 34.481	142° 12.906	7.4	1.21
VC2	-9° 34.402	142° 13.333	6.0	0.32
VC3	-9° 34.408	142° 13.344	6.0	1.29
VC4	-9° 34.059	142° 13.750	5.2	0.65
VC5	-9° 34.051	142° 13.752	6.5	0.70
VC6	-9° 34.041	142° 13.704	5.3	Core catcher only
VC7	-9° 35.612	142° 21.504	3.5	Core catcher only
VC8	-9° 35.612	142° 21.504	3.5	Core catcher only

VC1:— Wet bulk densities range from 1.05 g cm<sup>-3</sup> at 1.21 m to 2.04 g cm<sup>-3</sup> at 1.13 m (Fig. 8.1). Average wet bulk density for the core is 1.75 g cm<sup>-3</sup>. Bulk densities are mostly uniform but increase slightly downcore. A slight reduction in bulk density occurs between 0.1-0.25 m and then rises again at 0.4 m. P-wave velocities range from 1,050 m s<sup>-1</sup> at 0.53 m to 1,554 m s<sup>-1</sup> at 1.03 m (Fig. 8.1). Average P-wave velocity for the core is 1,245 m s<sup>-1</sup>. The velocities are mostly uniform downcore with significant gaps due to bad and spurious data. Magnetic susceptibility values range from 0.6 cgs at 0.07 m to 8.2 cgs at 0.66 m (Fig. 8.1). The average value for the core is 2.9 cgs. The magnetic susceptibility record shows highs at 0.27-0.42 m, 0.52-0.73 m and 0.74-0.93 m and generally increases downcore. Fractional porosity ranges from 0.40 at 1.13 m to 0.98 at 1.21 m (Fig. 8.1). The average porosity for the core is 0.58. The physical property data for VC1 show a possible correlation between 0.37-0.41 m and 1.01-

1.06 m characterised by relatively high bulk densities and magnetic susceptibility values. However, this pattern is not reflected in the sedimentology of the core which is uniform throughout. Further analysis is required to determine the cause of this possible correlation.

VC2:— Wet bulk densities range from  $1.06 \text{ g cm}^{-3}$  at 0.12 m to  $1.93 \text{ g cm}^{-3}$  at 0.17 m in this short core (Fig. 8.2). Average wet bulk density for the core is  $1.59 \text{ g cm}^{-3}$ . The data show a general decrease in bulk density below 0.14 m. P-wave velocities range from  $810 \text{ m s}^{-1}$  at 0.02 m to  $1,022 \text{ m s}^{-1}$  at 0.09 m (Fig. 8.2). Average P-wave velocity for the core is  $945 \text{ m s}^{-1}$ . Magnetic susceptibility values range from 0.15 cgs at 0.28 m to 0.9 cgs at 0.11 m (Fig. 8.2). The average value for the core is 0.42 cgs. Fractional porosity ranges from 0.47 at 0.17 m to 0.97 at 0.12 m (Fig. 8.2). The average porosity for the core is 0.66. The p-wave velocities show a similar trend to the bulk densities and there is a reasonable correlation between higher bulk densities and p-wave velocities below 0.14 m ( $r^2 = 0.48$ ). Magnetic susceptibility values show no correlation with any of the other physical data.

VC3:— Wet bulk densities range from  $1.04 \text{ g cm}^{-3}$  at 0.04 m to  $1.98 \text{ g cm}^{-3}$  at 0.75 m (Fig. 8.3). Average wet bulk density for the core is  $1.75 \text{ g cm}^{-3}$ . The data show a general increase downcore, probably due to increased compaction of the sediment grains, and then a general decrease below 0.91 m. There is also a prominent decrease in bulk density between 0.44–0.60 m. P-wave velocities range from  $813 \text{ m s}^{-1}$  at 0.27 m to  $1,058 \text{ m s}^{-1}$  at 0.75 m (Fig. 8.3). Average P-wave velocity for the core is  $943 \text{ m s}^{-1}$ . The data are relatively uniform downcore with numerous breaks due to bad and spurious data. Magnetic susceptibility values range from 0.14 cgs at 0.14 m to 18.5 cgs at 1.14 m which is the maximum value for all the cores (Fig. 8.3). The data are relatively uniform downcore except for a small rise in the values to 1.8 cgs between 0.59–0.71 m and a prominent spike between 1.12–1.18 m where values are  $>3$  cgs and rise to a maximum of 18.5 cgs. The reason for the spike in magnetic susceptibility values at the base of this core is not known, with no obvious sedimentary characteristic present to account for a significant increase in magnetic susceptibility. The average value for the core is 1.11 cgs or 0.65 if the spike is not considered. Fractional porosity ranges from 0.44 at 0.75 m to 0.99 at 0.04 m (Fig. 8.3). The average for the core is 0.58. There is a significant correlation in the physical property data for this core characterised by higher P-wave velocities and bulk densities, especially between 0.39–0.79 m ( $r^2 = 0.62$ ), and between 0.59–0.72 m also correspond to slightly higher magnetic susceptibility values.

VC4:— Wet bulk densities range from  $1.01 \text{ g cm}^{-3}$  at 0.66 m to  $1.99 \text{ g cm}^{-3}$  at 0.11 m (Fig. 8.4). Average wet bulk density for the core is  $1.74 \text{ g cm}^{-3}$ . The data show a general increase downcore until 0.48 m after which the bulk densities decrease to a minimum. The lowest bulk density values are associated with an increase in grain size and the presence of gravel in the core. P-wave velocities range from  $853 \text{ m s}^{-1}$  at 0.66 m to  $1,065 \text{ m s}^{-1}$  at 0.14 m (Fig. 8.4). Average P-wave velocity for the core is  $935 \text{ m s}^{-1}$ . The data are relatively uniform downcore with numerous breaks due to bad and spurious data. Magnetic susceptibility values range from 0.14 cgs at 0.35 m to 1.07 cgs at 0.64 m (Fig. 8.4). The magnetic susceptibility data show a similar pattern downcore as wet bulk density. Fractional porosity values range from 0.43 at 0.11 m to 0.88 at 0.64 m (Fig. 8.4). The average for the core is 0.57. There is slight correlation between the physical properties in this core from 0.06–0.15 m and 0.43–0.53 m which correspond to higher bulk densities, higher p-wave velocities, and peaks in magnetic susceptibility.

VC5:— Wet bulk densities range from  $1.04 \text{ g cm}^{-3}$  at 0.11 m to  $2.15 \text{ g cm}^{-3}$  at 0.48 m (Fig. 8.5). Average wet bulk density for the core is  $1.71 \text{ g cm}^{-3}$ . The data are highly variable, but show a slight increase downcore, particularly between 0.29–0.48 where the data are less

variable. P-wave velocities range from 816 m s<sup>-1</sup> at 0.23 m to 1,343 m s<sup>-1</sup> at 0.46 m (Fig. 8.5). Average P-wave velocity for the core is 988 m s<sup>-1</sup>. The data reflect the patterns in the bulk density data. Magnetic susceptibility values range from 0.37 cgs at 0.48 m to 0.96 cgs at 0.10 m (Fig. 8.5). The average for the core is 0.59 cgs. The data display significant variability downcore and show a general inverse relationship with bulk density and P-wave velocity. Fractional porosity values range from 0.34 at 0.48 m to 0.98 at 0.03 m (Fig. 8.5). The average for the core is 0.60. Between 0.29-0.48 m, where the physical property data display least variability downcore, wet bulk densities are 2.04-2.14 g cm<sup>-3</sup> and P-wave velocities are between 1034-1106 m s<sup>-1</sup> and there is positive correlation between the properties.

There are no significant correlations of the physical properties that occur across all of the cores, or even between cores recovered in the same study area (VC1-3: Area A, VC4-5: Area B). However, the average porosity values are similar for all of the cores ranging from 0.57 for VC4 to 0.66 for VC 2. These values indicate that in general the sediment makes up less than half of the core volume. These values are typical for unconsolidated marine sediments.

#### 4.3.5.2. Sediment Properties

Sediment contained in all the cores is very similar in texture and composition. All of the cores contain relatively homogenous poorly-sorted calcareous slightly-muddy gravelly sand (Figs. 8.1-8.5). Gravel clasts attain up to 6 mm in diameter in VC1 and VC3 and up to 2 mm in VC4. All of the gravel clasts are rounded to sub-rounded. The sediment is slightly coarser in VC4 and VC5 recovered from the sandwaves in Area B. Coarser gravel beds containing pebble-sized clasts occur between 0.08-0.23 m and below 0.49 m in VC4 and below 0.44 m in VC5. The boundaries of the coarse beds in VC 4 are irregular and distinct. The upper boundary for the coarse bed in VC5 is gradational. Other than these relatively coarse beds, there are no other distinct facies changes down any of the cores and no evidence to indicate breaks or hiatuses in sedimentation. Primary and secondary sedimentary structures are also absent from the cores. These structures possibly have been destroyed by burrowing organisms. However no live specimens were observed and the sediment appears to be comprised entirely of fossil material. Alternatively, any structures present in the sandwaves may have been destroyed during coring.

The x-rays reveal that the sediment recovered in each of the cores is reasonably homogenous throughout, with no evidence of internal bedding or alignment of grains, unconformities, or subtle changes in grain size (Figs. 8.1-8.5). However, significant changes in grain size are revealed by changes in the contrast of the x-rays down the core, including the coarse gravel beds in VC4 and VC5. The similar texture of these pebble-sized clasts in the x-rays indicates that they have a similar density to the rest of the sediment and are comprised of mostly carbonate material. Regions of relatively dense material and large consolidated gravel clasts are shown as lighter areas on the x-rays. A relatively dense region occurs below 1.08 m in VC1 and corresponds to an increase in density and p-wave velocity data (Fig. 8.1). Conversely, dark patches on the x-rays represent areas of the film that have been exposed and are inferred to represent gaps and holes in the sediment.

Sediment in all of the cores is composed of calcareous grains consisting of mollusc and bryozoan fragments, foraminifer tests (including abundant platy tests), *Halimeda* flakes and coral fragments, in decreasing abundance. The carbonate material contains both fresh and relict components. The relict grains are rounded and commonly encrusted with coralline

algae and worm tubes. Many clasts also bear the marks of (prolonged?) oxidation and have been substantially bored by organisms. The large gravel clasts in at the base of VC5 are comprised of encrusted consolidated coral and mollusc fragments. Sediment in the cores is generally greenish-grey (2.5Y 6/2 and 5Y 5/1) and has a mottled appearance due to the presence of numerous discoloured and dark patches. Lithic clasts are uncommon to rare but occur throughout. They are composed of very well-rounded mudstone and siltstone grains.



## 5. Discussion and Summary

The present survey has revealed for the first time, and in considerable detail, a picture of the dynamic nature of the seabed in Torres Strait. A range of seabed environments were revealed, including: reefal platforms, hard-grounds and fields of mobile sand ridges and sandwaves. These environments correspond to a range of habitats with different and varied associations of biota. In total, all the survey objectives were met and valuable data has been collected on the nature of the seabed geomorphology and sedimentary processes occurring in the major seabed environments in the vicinity of Turnagain Island that will be used to document the major biophysical processes in Torres Strait. A brief assessment of the survey objectives and tasks is provided below. The principal outcomes of our survey will also be used in support of regional marine planning in Australia. The results will directly feed into the process for identifying and selecting candidate marine protected areas for northern Australia, which is due to commence early in 2005.

### 5.1. Sediment Transport

Sediments in Torres Strait have been locally fashioned into well-developed sand ridges and sandwaves by wave, tide and wind-driven currents. The sediment transport estimates provide valuable insights into the sedimentary processes operating on the seabed in the vicinity of Turnagain Island and shallow tide-dominated environments in general. The data indicate that the sand is not simply transported back and forth across the bedforms but follows diverse pathways driven by complex water movements. The complex bathymetry produced by the fashioning of sand into bedforms enhances the complexity of the water flows around them.

Maximum sandwave crest migration estimates of  $11 \text{ m d}^{-1}$  in Area B and  $16 \text{ m d}^{-1}$  in Area A based on the data from the oceanographic moorings are comparable to rates for bedforms of comparable dimensions in Bass Strait (cf., Malikides et al., 1989). Estimates of  $0.9 \text{ m d}^{-1}$  in Area B and  $2.0 \text{ m d}^{-1}$  in Area A using the method of Bagnold (Eq. 13) are comparable to those reported for sandwaves in Torres Strait at Ackers Shoal and Aldophus Channel by Harris (1991). Interestingly, the data from the oceanographic moorings predict opposite net bedload transport vectors over the sand ridges in Area A and sandwaves in Area B. Net transport vectors are towards the east in Area B, opposite to the recorded movement of the sandwave crests based on the swath sonar surveys. This is due to the reversed asymmetry between the speeds of the ebb and flood currents between the two study sites.

Net bedload transport vectors are often different between flood and ebb currents (e.g., Huthnance, 1982). However, in Area B, small-scale ladder ripples indicate that net bedload transport vectors are also different for the crests and troughs of the main sandwaves. Diverging net bedload transport vectors, particularly between the troughs and crests of sandwaves, have also been reported for bedforms of comparable dimensions in Bass Strait (Malikides et al., 1989) and southern North Sea (Belderson et al., 1982; Kenyon et al., 1981). These secondary features are common and with the advent and application of high-resolution swath sonar, as in this study, they are now being resolved in extraordinary detail to reveal the fine-scale structure of water movements and associated sediment transport pathways over bedforms.

The principal advantage of using high-resolution bathymetry from the swath sonar surveys to calculate sediment transport rates over estimates from oceanographic data is that

it measures the actual change in seabed morphology (e.g., volume). In the present study, the swath sonar data has a resolution of 1 m<sup>2</sup>. The total volume of sediment transported in the bedforms during the 20 day survey attained 3 m<sup>3</sup>, in both Area A and B, which is equivalent to a total of 5.1 and 5.2 tonnes for the 14 days between bathymetric surveys, assuming an average density of 1.70 g cm<sup>-3</sup> and 1.73 g cm<sup>-3</sup> from the core data, respectively.

In Torres Strait, during the monsoon season when N and NW winds dominate, residual water movements are driven by these persistent winds towards the east, and during the trade wind season when E and SE winds dominate residual water flows are driven towards the west (e.g., Wolanski et al, 1988; Harris 1989, 1991). The magnitude of these wind-driven currents is typically <0.2 m s<sup>-1</sup> and is sufficient to induce a seasonal reversal in bedload and thus a reversal in the orientation and migration direction of sandwaves (Harris, 1991). The present survey fortuitously captured a moment when the sand ridges and sandwaves in the vicinity of Turnagain Island reversed their orientation from east to west associated with a related change in predominant wind direction. Our data have revealed that these reversals in orientation occur over a few days, and that individual sandwaves are highly responsive to the changes in residual water motions. What is still to be established is how quickly the sand ridges and sandwaves adopt a new equilibrium profile associated with the changed conditions. A second survey in October 2005 will provide additional data to help test this hypothesis by measuring the form of the bedforms after the end of the trade wind season.

Analysis of the high-resolution bathymetry and oceanographic data collected on the sand ridges in Area A and sandwaves in Area B provides insights into the migration of the bedforms in Torres Strait. The repeat bathymetry surveys indicate that while the crests of individual sand ridges and sandwaves may move several metres in response to changes in the direction of residual currents, the larger bedforms that they collectively form do not significantly alter their position. Individual sand grains are also transported great distances relative to the bedforms, as indicated by the oceanographic data and sediment transport estimates. This implies that the location of the bedforms in Torres Strait is relatively fixed. Presumably their morphology and positions are controlled by regional oceanographic conditions. It follows that the widespread movement of sandwaves in Torres Strait might result from prolonged perturbations in the regional oceanographic processes (e.g., several years of weaker monsoon-driven currents).

## 5.2. Seabed Environments and Habitats

Our high-resolution mapping and sampling has revealed fine scale variations in the morphology, texture and composition of the seabed in the vicinity of Turnagain Island. The nature of seabed environments and habitats is relatively diverse and the transitions between environments occur over very short distances. The varied nature of the sediments, sedimentary environments and habitats is associated with the complex and dynamic oceanographic processes throughout Torres Strait (e.g., Wolanski, 1986; Harris, 1988, Hemer et al., 2004). This is largely because seabed processes are enhanced around the islands and reefs and in the constricted channels between them due the local acceleration of tidal currents. The shallow seismic profiles indicate that the bed sediments form a relatively thin (<4 m thick) veneer over probable fluvial, coastal and marine deposits laid down when Torres Strait was emergent during the last glacial (~18,000 years ago) and in past periods of high sea level during the Late Quaternary.

Seabed sediments in Torres Strait are poorly-sorted calcareous sands and gravels. Only slight reworking and weathering of the grains is evident. The poorly-sorted nature and dominance of sand and gravel indicates that the sediments are not in equilibrium with the local oceanographic conditions. These textural features and the fresh nature of the carbonate grains implies that the seabed sediments are derived locally, principally from the in-situ break-up of fauna. Poorly-sorted calcareous sands and gravels are common all along the northern tropical Australian margin, and identical textural and compositional characteristics occur in sediments collected from throughout the northern and central Great Barrier Reef shelf (e.g., Heap et al., 2002; Orpin & Woolfe, 1999; Orpin et al., 2004).

Significantly, the seabed sediments do not contain large amounts of mud. Fine-grained material is unlikely to be present in large quantities due to the effects of the strong near-bed wave- and tide-induced currents removing all but the largest grains. Where present, the fine fraction is overwhelmingly dominated by carbonate material. Subsurface samples collected from the cores have the same textural and compositional characteristics as the surface sediments. The presence of the carbonate mud indicates that fine-material does accumulate in small quantities, but given the absence of significant quantities of terrigenous material in the surface and subsurface sediments it is unlikely that sediment exported from the Fly River is accumulating in the vicinity of Turnagain Island.

Near-bed suspended sediment concentrations peak at 30 mg l<sup>-1</sup> during neap tides. These concentrations are comparable to those observed in other shallow shelf regions in northern Australia with complex bathymetry such as between the patch reefs of the Great Barrier Reef and the Whitsunday Islands (e.g., Heap, 2000). While near-bed concentrations measured during the survey were variable, the turbidity data from the moorings and suspended sediment concentrations from the filter papers show a clear response to tidal currents, with peak concentrations coinciding with fastest currents. The composition of the suspended grains is the same as that of the seabed sediments. The patterns and nature of suspended sediment implies that increased turbidity associated with flood plumes from the Fly River is unlikely to have a significant effect on the seagrasses under the climate regime experienced during the survey, and no compelling evidence for their existence or effects was found. However, increased near-bed turbidity and abrasion by grains during peak tidal currents and a prolonged period of elevated concentrations during storm events could well be significant.

### **5.3. Implications for Seagrasses and Fisheries Management**

One of the principal objectives of the study was to better understand the relationship between oceanography, sandwaves and seagrasses and determine what effect (if any) the sandwaves might have on the distribution, abundance and survival (or otherwise) of seagrass in Torres Strait. The geophysical, oceanographic and sedimentary data collected on this survey indicate that the sandwaves are highly mobile and a significant amount of sediment is suspended in the water column. The movement of this sand has important implications for seagrasses in the vicinity of the sandwaves and sand ridges.

The ability of the seagrasses to colonise and germinate via seed dispersal is likely to be low in close proximity to the sandwaves, particularly those located in Area B. The physical effects of sediment abrasion and possible smothering would almost certainly cause seagrass seedlings and plants to become dislodged. Near-bed suspended sediment concentrations were also higher over the sandwaves and the associated reduction in light, especially at

depth, would be an important factor in determining the presence or absence of seagrasses. As such, Areas A and B are not considered ideal seagrass habitats due to the strong tidal currents, high near-bed turbidity and very mobile bedforms. This is reflected in the generally low abundance and sparse nature of seagrasses found in each area.

Seagrasses in Torres Strait are growing in an environment characterised by frequent disturbances of the seabed. Our survey has revealed that such seabed disturbances are associated with the widespread re-orientation of sandwaves associated with seasonal changes in wind direction, and more frequent and rapid increases in near-bed turbidity and strong near-bed currents coinciding with spring tides and waves. Higher suspended sediment concentrations near the bed result in a reduction in light for photosynthesis. Widespread and significant movement of the sandwaves result in smothering of available habitat and existing seagrass stands. Consequently, it seems likely that there is continual competition between species which may account for the mixed species meadows observed in each of the study areas.

The patterns of seagrass observed in Areas A and B are similar to those found by other workers. For example, Rasheed (2004) found *Syringodium isoetifolium* to be a rapid asexual coloniser of disturbed areas with very fast rhizome growth rates. It out competed *H. ovalis* by asexual growth but *H. ovalis* was found to be a pioneer species and more successful through sexual (seed) reproduction. The distribution and abundance of these species in the study areas indicates that similar processes are occurring in the study areas.

Three of the species found *Halophila ovalis*, *Halophila decipiens* and *Halophila spinulosa* are known food for dugongs and were observed mostly in finer-grained sediments. *Syringodium isoetifolium* and *Cymodocea rotundata* are a more robust species and were observed on the coral and algal reefs; these species prefer rocky/rubbly or coarser-grained sediments. The densities of seagrass observed and the range of species recorded in all of the sedimentary environments in both Areas A and B provide suitable habitat for juvenile fish, crayfish and other vertebrates and invertebrates. This habitat is essential for the viability of the marine ecosystems in Torres Strait because it forms the primary trophic level in the food web for the region. As such, both of the study areas are considered an important fisheries resource. Movement of the sandwaves on a widespread basis could compromise this resource in Torres Strait by reducing the area of seagrasses available for juvenile fish and crayfish. Macro-algae were also observed at many sites where seagrass was not found. *Sargassum spp.* was one of the main algae species observed and it may support crayfish populations when seagrass is not available. It forms a considerable habitat structure and is valuable as a fisheries habitat. A detailed map of the seagrass and algae communities would quantify the significance of these habitat types.

## 6. Acknowledgements

We thank the crew and master of the RV *James Kirby* for their dogged assistance throughout the survey. We are grateful of Prof. Bob Henderson (School of Earth Sciences, James Cook University) for permission to use the RV *James Kirby* and hire the shallow swath sonar, Chirper and vibrocoring equipment. We are indebted to Toshi Nakada (Torres Strait Regional Authority) for advice on indigenous issues and the Torres Strait Island community for their support of the survey. Financial support was provided by Geoscience Australia, Reef CRC, and Queensland Department of Primary Industry and Fisheries. Dr Alan Butler (CSIRO – Marine Research) provided guidance on survey design. Alex McLachlan, Neil Ramsay, Tony Watson, and Richard Brown of the sedimentology laboratory at Geoscience Australia managed all sample analyses and are thanked for their timely and efficient production of the texture and composition data. The video footage was edited by Jakob Harris (Geoscience Australia). The original report benefited from reviews by Drs Brendan Brooke and Phil O'Brien of Geoscience Australia.



## 7. References

- Agrawal, Y.C. & Pottsmith, H.C., 2000. Instruments for particle size settling velocity observations in sediment transport. *Marine Geology* 168, 89-114.
- Belderson, R.H., Johnson, M.A. & Kenyon, N.H., 1982. Bedforms. In: Stride, A.H. (Ed.), *Offshore Tidal Sands, Processes and Deposits*, pp.27-57. Chapman and Hall, London.
- Best, A.I. & Gunn, D.E., 1999. Calibration of marine sediment core loggers for quantitative acoustic impedance studies. *Marine Geology* 160, 137-146.
- Brown, C.B., 1950. Sediment transportation. In: Rouse, H., (Ed.), *Engineering Hydraulics*, Wiley, New York. 797pp.
- Coles, R., Smit, N. McKenzie, L., Roelofs, A., Haywood, M. & Kenyon, R. 2004. Seagrasses. In: National Oceans Office, *Description of Key Species Groups in the Northern Planning Area*, pp.9-22. National Oceans Office, Hobart.
- Damuth, J.E., 1980. Use of high-frequency (3.5-12 kHz) echograms in the study of near-bottom sedimentation processes in the deep-sea: a review. *Marine Geology*, 38, 51-75.
- Engelund, F. & Hansen, E., 1967. *A Monograph on Sediment Transport in Alluvial Streams*. Teknisk Vorlag, Copenhagen, 62pp.
- Gadd, P.E. Lavelle, J.W. & Swift, D.J.P., 1978. Estimates of sand transport on the New York shelf using near-bottom current meter observations. *Journal of Sedimentary Petrology*, 48, 239-252.
- Gagan, M.K., Chivas, A.R. & Herczeg, A.L., 1990. Shelf-wide erosion, deposition, and suspended sediment transport during cyclone Winifred, central Great Barrier Reef, Australia. *Journal of Sedimentary Petrology*, 60, 456-470.
- Gerland, S. & Villinger, H., 1995. Non-destructive density determination on marine sediment cores from gamma-ray attenuation measurements. *Geo-Marine Letters* 15, 111-118.
- Hardisty, J., 1983. An assessment and calibration of formulations for Bagnold's bedload equation. *Journal of Sedimentary Petrology*, 53, 1007-1010.
- Harris, P.T., 1991. Reversal of subtidal dune asymmetries caused by seasonally reversing wind-driven currents in Torres Strait, northeastern Australia. *Continental Shelf Research*, 11, 655-662.
- Harris, P.T., 1989. Sandwave movement under tidal and wind-driven currents in a shallow marine environment: Adolphus Channel, northeastern Australia. *Continental Shelf Research*, 9, 981-1002.
- Harris, P.T., 1988. Sediments, bedforms and bedload transport pathways on the continental shelf adjacent to Torres Strait, Australia-Papua New Guinea. *Continental Shelf Research*, 8, 979-1003.
- Heap, A.D., Daniell, J., Mazon, D., Harris, P.T., Sbaffi, L., Fellows, M. & Passlow, V., 2004. *Geomorphology and Sedimentology of the Northern Planning Region of Australia*. Geoscience Australia Record 2004/11, Canberra. 68pp.
- Heap, A.D., Dickens, G.R. & Stewart, L.K., 2002. Holocene storage of siliciclastic sediment around islands on the middle shelf of the Great Barrier Reef Platform, north-east Australia. *Sedimentology* 49, 603-621.

- Heap, A.D., Dickens, G.R. & Stewart, L.K., 2001. Late Holocene sediment in Nara Inlet, central Great Barrier Reef platform, Australia: sediment accumulation on the middle shelf of a tropical mixed clastic/carbonate systems. *Marine Geology* 176, 39-54.
- Heap, A.D., Larcombe, P. & Woolfe, K.J., 1999. Storm-dominated sedimentation in a protected basin fringed by coral reefs, Nara Inlet, Whitsunday Islands, Great Barrier Reef. *Australian Journal of Earth Sciences* 46, 443-451.
- Heap, A.D., 2000. *Composition and Dynamics of Holocene Sediment next to the Whitsunday Islands on the Middle Shelf of the Great Barrier Reef Platform, Australia*. Unpublished PhD Thesis, James Cook University, Townsville. 167pp.
- Hemer, M.A., Harris, P.T., Coleman, R. & Hunter, J., 2004. Sediment mobility due to currents and waves in the Torres Strait-Gulf of Papua region. *Continental Shelf Research* 24, 2297-2316.
- Huthnance, J.M., 1982. On one mechanism forming linear sandbanks. *Estuarine, Coastal and Shelf Science* 14, 79-90.
- Kenyon, N.H., Belderson, R.H., Stride, A.H. & Johnson, M.A., 1981. Offshore tidal sandbanks as indicators of net sand transport and as potential deposits. *International Association of Sedimentologists, Special Publication* 5, 257-268.
- Larcombe, P. & Carter, R.M., 2004. Cyclone pumping, sediment partitioning and the development of the Great Barrier Reef shelf system: a review. *Quaternary Science Reviews* 23, 107-135.
- Li, M.Z. & Amos, C.L., 2001. SEDTRANS96, the upgraded and better calibrated sediment-transport model for continental shelves. *Computers and Geosciences* 27, 619-645.
- Long, B.G. & Poiner, I.R., 1997. *Seagrass communities of Torres Strait, Northern Australia*. Report to the Torres Strait Scientific Advisory Committee No 27, December 1997, CSIRO, Cleveland. 49 pp.
- Long B.G., Skewes, T., Thomas, M., Isdale, P., Pitcher, R. & Poiner, I., 1997. *Torres Strait Seagrass Dieback. Final Report to TSFSAC* 26. CSIRO Division of Marine Research, Cleveland.
- Malikides, M., Harris, P.T. and Tate, P.M., 1989. Sediment transport and flow over sandwaves in a non-rectilinear tidal environment: Bass Strait, Australia. *Continental Shelf Research* 9, 203-221.
- McMillan, J., 1982. *A Global Atlas of GEO-3 Significant Wave Height Data and Comparison of the Data with National Buoy Data (156882)*. Technical Report, NASA, Wallops Flight Centre, Virginia.
- Miller, M.C., McCave, I.N. & Komar, P.D., 1977. Threshold of sediment motion under unidirectional currents. *Sedimentology* 24, 507-527.
- Muller and Gastner, 1971. The "Karbonat-Bombe", a simple device for the determination of the carbonate content in sediments, soils, and other materials. *Neues Jahrbuch fuer Mineralogie* 10, 466-469.
- Nortek, 2000. Vector Operations Manual, 1 November 2000. (<http://www.nortek-as.com>).
- Orpin, A.R., Brunskill, G.J., Zagorskis, I. & Woolfe, K.J., 2004. Patterns of mixed siliciclastic-carbonate sedimentation adjacent to a large dry-tropics river on the central Great Barrier Reef shelf, Australia. *Australian Journal of Earth Sciences*, 51, 665-683.

- Orpin, A.R. & Woolfe, K.J., 1999. Unmixing relationships as a method of deriving a semi-quantitative terrigenous sediment budget: central Great Barrier Reef lagoon. *Sedimentary Geology* 129, 25-35.
- Pawlowicz, R., Beardsley, B. & Lentz, S., 2002. Classical tidal harmonic analysis including error estimates in MATLAB using T\_TIDE. *Computers and Geosciences* 28, 929-937.
- Pingree, R.D. & Griffiths, D.K., 1979. Sand Transport paths around the British Isles resulting from M2 and M4 tidal interactions. *Journal of the Marine Biology Association, UK* 59 497-513.
- Pond, S. & Pickard, G.L., 2000. *Introductory Dynamical Oceanography*. Second Edition, Butterworth Heinemann, Oxford. 329pp
- Porter-Smith, R., Harris, P.T., Andersen, O.B., Coleman, R., Greenslade, D., & Jenkins, C.J., 2004. Classification of the Australian continental shelf based on predicted sediment threshold exceedance from tidal currents and swell waves. *Marine Geology* 211, 1-20.
- Rasheed, M.A., 2004. Recovery and succession in a multi-species tropical seagrass meadow following experimental disturbance: the role of sexual and asexual reproduction. *Journal of Experimental Marine Biology and Ecology* 310, 13-45.
- Weber, ME., Niessen, F., Kuhn, G. & Wiedicke, M., 1997. Calibration and application of marine sedimentary physical properties using a multi-sensor core logger. *Marine Geology* 136, 151-172.
- Williams, G.C. & Staples, D.J., 1990. Australia's fisheries research in the Torres Strait protected zone. In: Lawrence D. & Cansfield-Smith, T., (Eds.), *Sustainable development for traditional inhabitants of the Torres Strait region. Proceedings of the Torres Strait baseline study conference, November 1990*, pp. 229- 237. Great Barrier Reef Marine Park Authority, Townsville.
- Wolanski, E., Ridd, P. & Inoue, M., 1988. Currents through Torres Strait. *Journal of Physical Oceanography* 18, 1535-1545.
- Wolanski, E., 1986. The physical oceanography of Torres Strait. In: Haines, A., Williams, G.C. & Coates, D. (Eds.), *Torres Strait Fisheries Seminar*, pp.275-291. Australian Government Publication Service, Canberra.
- Woodroffe, C.D., Kennedy, D.M., Hopley, D., Rasmussen, C.E. & Smithers, S.G., 2000. Holocene reef growth in Torres Strait. *Marine Geology*, 170, 331-346.
- Xu, Z., 2002. *Ellipse Parameters Conversion and Velocity Profiles for Tidal Currents in Matlab*. Maurice-Lamontagne Institute, Ocean Science Division, Fisheries and Ocean Canada. 24pp.
- Yalin, M.S., 1963. An expression for bed-load transportation. *Journal of the Hydraulic Division, ASCE* 89, 49-59.

## 8. Appendices

### 8.1. Appendix A – Survey Leaders Log

Geoscience Australia Survey 266, Torres Strait, 2004

Survey Leaders Log

RV *James Kirby*

Peter Harris (28 March to 5 April), Andrew Heap (6 to 17 April)

**Sunday, 28 March 2004.** Scientific party boarded vessel in Thursday Island harbour. Vibrocore system plus 4 fuel drums unloaded and stored ashore. Underway @ 0900 UTC. After experiencing some difficulty with equipment software, CSIRO multisensor system was booted with delayed start time. Arrived on station east of the Orman Reefs @ 1500 UTC and deployed CSIRO instrument frame #1. Commenced swath sonar mapping and headed into an anchorage west of the Orman Reefs. At anchor @ 1830 UTC.

**Monday, 29 March 2004.** Underway @ 0600 UTC, headed north to survey area (B) located SE of Turnagain Island to run a preliminary transect and deploy instruments. BRUCE frame deployed @ 1230 UTC. CSIRO frame #2 deployed @ 1250. Transit to survey area (A) located NE of Turnagain Island. Swath head touched the crest of a sand ridge. After several grab and camera stations, it was determined that only algae beds (and not seagrass) occur in this area, and it is too shallow for swath mapping. Hence it was abandoned and an alternate survey area located SW of Turnagain Island was chosen. Arrived at the eastern margin of the area and found shallow water (swath head 1.2 m above seabed). A safe anchorage was found in 3.5 m water @ 1830 UTC. Camera and grab deployed at anchorage before tea.

**Tuesday, 30 March 2004.** Underway @ 0630 UTC, headed south and then west along 10m deep channel. After turning north and into the alternate survey area (A2) an area of seagrass was located using camera and grab. After 3 reconnaissance survey lines and two camera/grab stations, a 2 km x 2 km survey area was located with suitable seagrass and bedform distribution. The CSIRO mooring #3 was deployed @ 1130 UTC in the centre of the grid. Swath mapping commenced @ 1215 UTC with 40 m line spacing. Ship anchored at 1830 UTC. Camera and grab deployed at anchorage before tea.

**Wednesday, 31 March 2004.** Underway @ 0630 UTC, filling in gaps in swath coverage. Shallow areas <5 m LAT depth can only be mapped during high water, which was at 1230 PM today, using 25 m line spacing. Area A completed @ 1400 UTC, transit to Area B. Area B swath mapping started @ 1500 UTC, with 25 m line spacing due to shallow depths over sandwave crests.

**Thursday, 1 April 2004.** Underway @ 0600 swath mapping Area B. Finished @ 1500 UTC. Completed 9 grab sample and video stations by @ 1700 UTC before transit back to Area A. Arrived @ 1830 UTC. Camera and grab deployed at anchorage before tea.

**Friday, 2 April 2004.** Underway @ 0630 UTC. Completed 29 grab sample and video stations by 1600 UTC before selecting a suitable site for our 24-hour anchor station. The ideal combination of large bedforms occurring with seagrass was found in the NE corner of the survey area (A). In position and anchored fore and aft by 1800 UTC and

commenced sampling at 20 minute intervals. Problems with dragging the main anchor disrupted measurements several times during the night.

**Saturday, 3<sup>rd</sup> April 2004.** Completed 24-hour sampling at @ 2000 UTC and transited to Area B. The second 24-hour station located near station BRUCE was not started until 2 AM due to difficulties with getting ship's anchors to hold.

**Sunday, 4<sup>th</sup> April 2004.** Stern anchor dragged across the camera/current meter frame and damaged the camera cable. Repairs allowed the camera to function but not record digital data internally due to faulty communication connection. Complete repairs will require re-termination of the main camera wire. It was decided to abandon the stern anchor and just use the bow anchor to avoid further damage to the instruments. Sampling continued without further incident.

**Monday, 5 April 2004.** Sampling completed @ 0300 UTC. Transit to Thursday Island to pickup vibrocorer frame and drop off one scientist (P. Harris). Arrived into TI harbour @ 1200 UTC.

**Tuesday, 6 April 2004.** Departed Thursday Island at 0700 UTC and transited to field sites. Anchored behind Aldai Reef @ 1630 UTC for the night to set up vibrocorer, make repairs to damaged camera cable, and update the shipboard database.

**Wednesday, 7 April 2004.** Underway at 0630 UTC. Began vibrocoring in Area A @ 0700 UTC. Collected six vibrocores from four sites: VC1 (1.2 m) @ 0735 UTC; VC2 (0.43 m) @ 0846 UTC; VC3 (1.3 m) @ 0907 UTC; VC4 (0.69) @ 0944 UTC; VC5 (0.73) @ 1126 UTC; and VC6 (core catcher sample only) @ 1300 UTC. VC4-6 returned bent barrels. Cores VC1-5 terminated in poorly-sorted muddy medium to coarse calcareous sand. VC6 went in on an angle and terminated in very coarse calcareous sand and gravel. Transited to Area B @ 13:30 UTC to commence coring. Attempted VC7, but it was not completed due to rough sea conditions. Coring was abandoned for the day. Completed two swath lines over sandwaves in the south of Area B. Transited to safe anchorage behind Numar Reef @ 17:00 UTC.

**Thursday, 8 April 2004.** Underway @ 0630 UTC. Commenced vibrocoring in Area B @ 0700 UTC. Conditions quickly became too rough and it was decided to abandon coring for the day in Area B. Commenced grab stations in Area B @ 0815 UTC. The ship had difficulty maintaining position due to strong winds and strong tidal currents. Problems also continued to plague the camera. Transited to Area A to complete the swath mapping @ 1030 UTC. An additional 20 lines of 25 m spacing were completed by 1700 UTC. Anchored behind Aldai Reef for the night.

**Friday, 9 April 2004.** Underway @ 0630 UTC. Changed over vibrocorer in preparation for 24 hr camera stations. Commenced swath mapping to fill in gaps in Area A @ 0740 UTC. Completed swath mapping of additional region in Area A @ 0945 UTC. Completed additional 13 grab and camera stations @ 1630 UTC. Commenced 24 hr anchor station @ 1820 UTC. Due to strong currents and moderate seas, only the bow anchor was used to maintain position.

**Saturday, 10 April 2004.** Completed 24 hr anchor station in Area A @ 1920 UTC. The boat only had to be re-positioned once after the anchor dragged in rough conditions.



Commenced 24 hr anchor station in Area B @ 2140 UTC. Relatively rough conditions prevailed, with winds of 25 knots, gusting to >30 knots.

**Sunday, 11 April 2004.** Completed 24 hr anchor station in Area B @ 2240 UTC. Rough conditions prevailed throughout with waves frequently washing onto the back deck. The only incident to report during the station was a broken hydraulic hose on the A-frame which prevented a couple of samples from being taken while it was repaired by the crew. Transited to Thursday Island @ 2330 UTC.

**Monday, 12 April 2004.** Arrived in Thursday Island harbour @ 0800 UTC. S. Kerville (QDPI) left the boat and we took on more fuel and water. Went ashore at Horn Island. Departed Thursday Island harbour @ 1430 UTC on transit back to field sites. Anchored at Mt Earnest @ 1815 UTC for the night.

**Tuesday, 13 April 2004.** Underway @ 0400 UTC. Arrived at Area B and commenced repeat swath mapping survey @ 0945 UTC. Rough conditions meant that swath mapping proceeded more slowly than in the first week, and the data are more noisy. A smaller priority area, over the sand waves in the vicinity of the BRUCE current meter deployment, was delineated for swath and was expanded as time permitted. Anchored behind Numar Reef @ 1745 UTC for the night.

**Wednesday, 14 April 2004.** Underway @ 0630 UTC. Completed swath mapping of Area B @ 1135 UTC. Transited to Area A and commenced repeat swath survey of a priority area over sandwaves and seagrasses in the vicinity of the 24 hr station and CSIRO current meter mooring @ 1240 UTC. This priority area was expanded as time permitted. Anchored behind Aldai Reef @ 1845 UTC for the night.

**Thursday, 15 April 2004.** Underway @ 0630 UTC. Completed swath mapping of Area A @ 1645 UTC. Anchored behind Aldai Reef @ 1715 UTC for the night. Science party (4) and skipper went ashore to beach comb for shells and photograph sandy tidal bedforms on the associated cay. Collected a grab sample from the top of the sandy bedforms.

**Friday, 16 April 2004.** Underway @ 0630 UTC. Recovered CSIRO mooring in Area A @ 0923 UTC. The data from the ADCP and pressure sensor were downloaded onto PC and the sensors for all instruments were cleaned with fresh water. Mooring was redeployed at -9°34.386, 142°13.393 in 7.3 m water depth @ 0917 UTC. Commenced swath mapping SW region of Area B @ 1130 UTC to wait for slack water to recover BRUCE. Completed swath mapping @ 1255 UTC. Recovered the BRUCE mooring @ 1325 UTC. Water samples were taken and filtered to calibrate the instruments for the effects of biofouling of the LISST and OBS sensors. Could not get the PC to communicate with BRUCE so the instruments were cleaned with fresh water and disassembled. Attempted two vibrocores on top of the sandwaves in Area B: VC7 (core catcher sample only) @ 1547 UTC and VC8 (core catcher sample only) @ 1605 UTC. Completed swath mapping of sandwaves in Area B @ 1810 UTC. Began transit to Thursday Island @ 1820 UTC. Anchored behind Mt Earnest @ 0200 UTC.

**Saturday, 17 April 2004.** Underway @ 0700 UTC for final transit to Thursday Island. Equipment was packed up on deck by GA staff. Arrived in TI harbour @ 1100 UTC. Equipment was offloaded from boat and stored with SeaSwift in preparation for transit to Canberra. Scientists departed vessel @ 1330 UTC.

## 8.2. Appendix B – Shallow Seismic Profiles

Figures showing the shallow seismic profiles are provided on the data DVD in Windows Bitmap format. The figures are screen dumps obtained from the seismic viewing program SeisVU ([www.phoenixdatasolutions.co.uk/seisvu.htm](http://www.phoenixdatasolutions.co.uk/seisvu.htm)). The filenames follow the convention: *GA survey number\_Area\_Line Number*. (e.g., 266\_AreaA\_400). The line numbers indicate the distance in metres from the northern-most line. The latitudes and longitudes and shot points for the beginning and end of the lines are contained in the accompanying Excel spreadsheet called "line\_locations.xls".

## 8.3. Appendix C – Photos of the BRUCE Mooring

Photos of the BRUCE mooring are provided on the data DVD in jpg format.

## 8.4. Appendix D – Photos of the CSIRO Moorings

Photos of the CSIRO moorings are provided on the data DVD in jpg format.

## 8.5. Appendix E – Problems with the BRUCE Mooring

On recovery of the BRUCE mooring, the Nortek battery power was ~5V. Typically, the current meter operates with a voltage of 10-12 V. However, even with a new battery pack communications could not be established. The LISST-100 appeared to have no stored data. All instrumentation was packed away to be transported to Canberra with no data having been recorded. On closer inspection it was determined that salt-water had penetrated the housing of the current meter. No current meter data from the BRUCE mooring was recorded.

Data were recovered from the LISST-100. However, the data are very noisy with warnings ranging from 'Warning: water too clear' to 'Warning: water too turbid' over time scales of 0.5 s. The associated grain size distributions are random between successive observations and strangely multimodal, containing up to three jagged peaks that shift in position (i.e., modal size) over the period of recording separated by bins with no data at all. Given that the LISST-100 requires a signal from the Nortek current meter to commence sampling, it appears that the problems associated with the current meter have compromised the data recorded by the laser particle sizer. No analysis of the LISST-100 data has been carried out. As such, no meaningful data was recovered from the BRUCE mooring.

## 8.6. Appendix F – Digital Video Footage

Excerpts of the digital video footage for select sites are provided on the data DVD in mpeg format. The filenames follow the convention: *GA Survey Number\_Station Number, Operation Type and Operation Number* (e.g., 266\_21CAM16), and for the 24-hour stations *GA Survey Number\_Station Number, Operation Type and Operation Time* (e.g., 266\_21CAM0020GMT).

## 8.7. Appendix G – Textural Characteristics of Surface Sediments

The tables below show the textural data for each surface sample based on sieve analysis and carbonate bomb analysis, and are thus expressed as weight percents. Grainsize distribution graphs and associated data from the Malvern are contained on the data DVD in jpg format. The filenames follow the convention: *7-digit Lab Number\_GA Survey Number\_Station Number, Operation Type and Operation Number* (e.g., 1404874\_266\_03GR01).

Table 8.1. Textural characteristics of surface sediment samples collected in Area A.

Sample Id	Latitude	Longitude	%Gravel	%Sand	%Mud	%CaCO <sub>3</sub> (Bulk)	%CaCO <sub>3</sub> (Sand)	%CaCO <sub>3</sub> (Mud)
266/13GR12	-9.5735	142.2288	35.28	64.28	0.43	87.2	91.2	I/S
266/15GR14	-9.5732	142.2236	27.39	71.59	1.01	90.2	93.3	I/S
266/18GR15	-9.5670	142.2209	35.19	60.79	4.01	88.2	92.3	I/S
266/28GR24	-9.5724	142.2252	18.00	74.32	7.69	89.2	92.3	I/S
266/29GR25	-9.5678	142.2295	41.32	57.83	0.85	90.2	92.3	I/S
266/30GR26	-9.5674	142.2290	11.73	87.50	0.77	91.2	92.3	I/S
266/31GR27	-9.5670	142.2284	58.77	40.91	0.31	89.7	93.3	I/S
266/32GR28	-9.5670	142.2277	34.76	65.20	0.04	90.2	92.3	I/S
266/33GR29	-9.5687	142.2282	23.72	75.96	0.32	90.2	92.3	I/S
266/35GR31	-9.5712	142.2292	28.76	68.51	2.73	89.2	93.3	I/S
266/36GR32	-9.5692	142.2235	24.62	72.58	2.80	53.7	92.3	I/S
266/37GR33	-9.5672	142.2236	43.60	50.70	5.71	89.2	91.2	67.9
266/38GR34	-9.5708	142.2240	18.62	76.59	4.79	89.2	92.3	72.0
266/39GR35	-9.5724	142.2252	23.98	75.72	0.30	87.2	91.2	I/S
266/40GR36	-9.5718	142.2270	37.18	61.76	1.06	88.2	92.3	I/S
266/41GR37	-9.5707	142.2222	12.69	83.67	3.64	90.2	92.3	71.0
266/42GR38	-9.5712	142.2213	23.94	71.09	4.97	90.2	92.3	68.9
266/43GR39	-9.5716	142.2198	31.14	57.56	11.31	88.2	90.2	67.9
266/44GR40	-9.5719	142.2183	35.05	62.14	2.80	89.2	91.2	I/S
266/45GR41	-9.5754	142.2218	31.36	58.04	10.60	84.1	89.2	69.9
266/46GR42	-9.5741	142.2254	20.56	77.84	1.60	90.2	92.3	69.9
266/47GR43	-9.5753	142.2167	25.60	68.18	6.22	76.0	91.2	I/S
266/48GR44	-9.5751	142.2146	15.93	73.60	10.47	84.1	89.2	71.0
266/49GR45	-9.5740	142.2156	17.96	74.74	7.31	80.1	91.2	73.0
266/51GR47	-9.5675	142.2113	12.70	83.92	3.38	87.2	91.2	72.0
266/52GR48	-9.5670	142.2139	49.85	49.72	0.43	88.2	93.3	I/S
266/53GR49	-9.5687	142.2154	27.46	65.16	7.39	84.1	92.3	71.0
266/54GR50	-9.5710	142.2176	26.77	66.67	6.55	89.2	93.3	71.0
266/55GR51	-9.5707	142.2193	17.41	79.79	2.80	91.2	93.3	I/S
266/56GR52	-9.5711	142.2157	30.23	68.52	1.25	85.2	92.3	I/S
266/57GR53	-9.5678	142.2175	11.06	88.25	0.69	89.2	92.3	I/S
266/67GR58	-9.5758	142.2129	19.79	74.31	5.90	83.1	90.2	72.0
266/68GR59	-9.5771	142.2123	17.90	79.14	2.96	86.2	90.2	I/S
266/69GR60	-9.5760	142.2142	21.09	76.39	2.52	86.2	90.2	I/S
266/70GR61	-9.5789	142.2163	33.31	63.38	3.31	83.1	91.2	74.0
266/71GR62	-9.5789	142.2148	22.65	62.08	15.27	83.1	90.2	71.0
266/72GR63	-9.5786	142.2121	32.88	66.05	1.07	88.2	91.2	I/S
266/73GR64	-9.5767	142.2333	24.53	73.34	2.13	81.1	89.2	I/S
266/74GR65	-9.5758	142.2210	25.58	64.60	9.83	84.1	91.2	69.9
266/75GR66	-9.5764	142.2234	46.34	48.85	4.81	85.2	90.2	72.0

266/76GR67	-9.5773	142.2265	33.73	61.06	5.21	87.2	91.2	69.9
266/77GR68	-9.5779	142.2292	46.11	51.96	1.93	88.2	91.2	I/S
266/78GR69	-9.5784	142.2276	42.35	55.64	2.01	88.2	90.2	I/S
266/79GR70	-9.5787	142.2251	65.64	34.09	0.27	84.1	88.2	I/S

I/S = insufficient sample for analysis.

Table 8.2. Textural characteristics of surface sediment samples collected in Area B.










Sample Id	Latitude	Longitude	%Gravel	%Sand	%Mud	%CaCO <sub>3</sub> (Bulk)	%CaCO <sub>3</sub> (Sand)	%CaCO <sub>3</sub> (Mud)
266/06GR05	-9.5913	142.3579	7.86	92.06	0.07	90.2	84.1	0.0
266/20GR16	-9.5900	142.3516	54.12	45.43	0.45	77.0	91.2	0.0
266/21GR17	-9.5909	142.3498	51.42	47.62	0.96	88.2	90.2	0.0
266/22GR18	-9.5917	142.3503	89.54	9.36	1.10	82.1	89.2	0.0
266/23GR19	-9.5928	142.3511	47.85	47.92	4.23	82.1	90.2	0.0
266/24GR20	-9.5934	142.3515	64.39	35.59	0.01	88.2	91.2	0.0
266/25GR21	-9.5944	142.3524	4.30	95.63	0.07	91.2	91.2	0.0
266/26GR22	-9.5912	142.3543	55.24	44.02	0.74	87.2	90.2	0.0
266/27GR23	-9.5933	142.3584	34.66	65.26	0.08	92.3	92.3	0.0
266/62GR57	-9.5951	142.3563	2.96	97.03	0.01	90.2	92.3	0.0

## 8.8. Appendix H – Core Logs











The core logs are produced from the visual logs of the cores (Figs 8.1-8.5). They contain the physical property data (Bulk Density, P-wave Velocity, Magnetic Susceptibility, Fractional Porosity), texture and composition information, visual log (including digital images and x-radiographs) and comments on specific features.

### Core Log Legend





#### Sedimentary Features



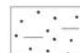


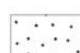
	Shell Hash
	Wood
	Organic Fragments
	Articulated Shell (in-situ)
	Articulated Shell
	Intact Shell Valve(s)
	Laminations
	Burrows
	Unconformity

#### Fossils




	Gastropods
	Corals
	Bryozoans
	Foraminifers
	Bivalves
	Echnoids
	Halimeda
	Worm Tubes
	Scaphopods
	Crustaceans

#### Lithology

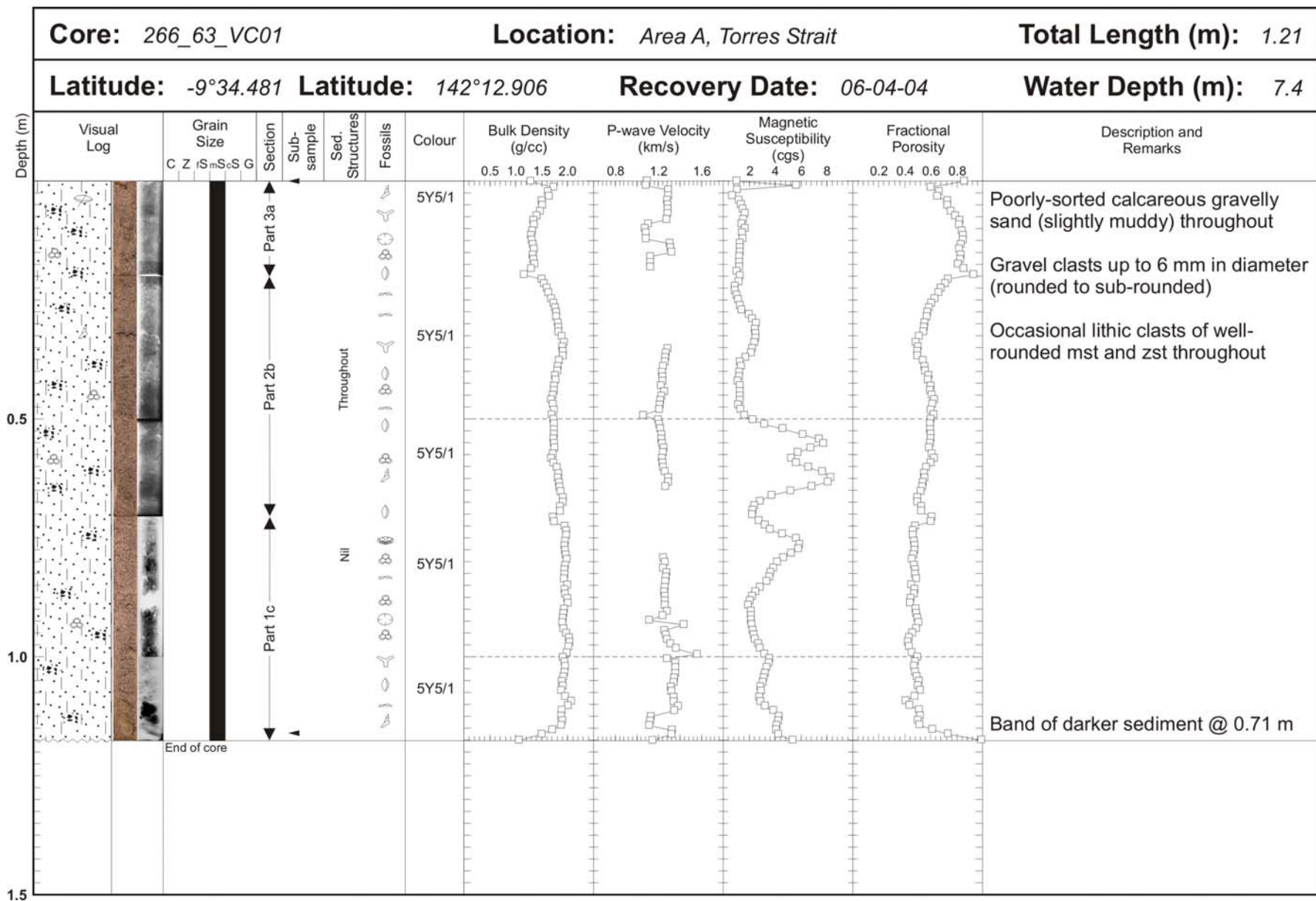
Gravel	
Sandy mud	
Silt	
Clay	

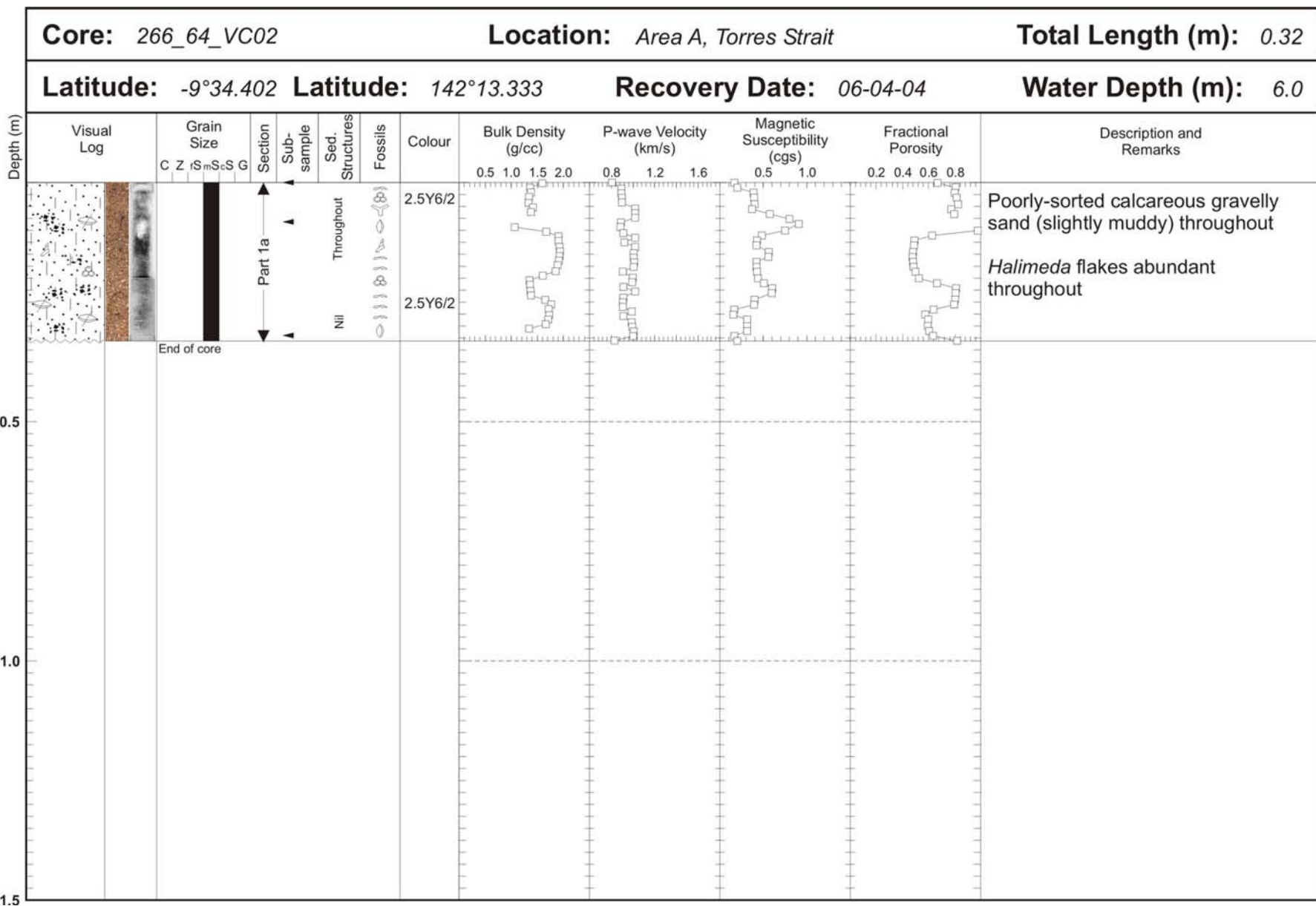
	Fine	Medium	Coarse
Muddy gravelly sand			
Sand			

#### Sub-samples

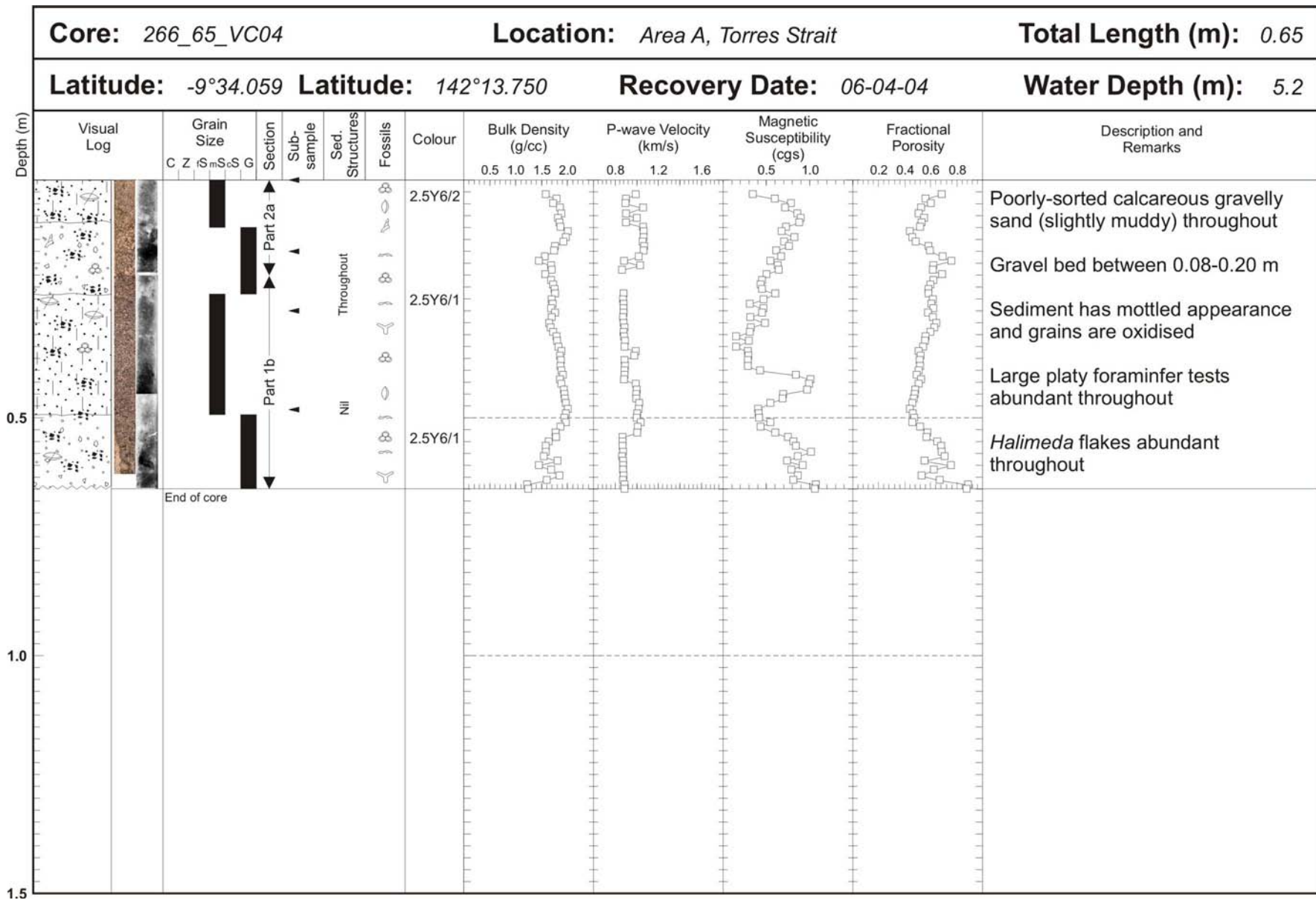
	Grain-size/CaCO <sub>3</sub> /XRF
	C-14 age
	Mineralogy

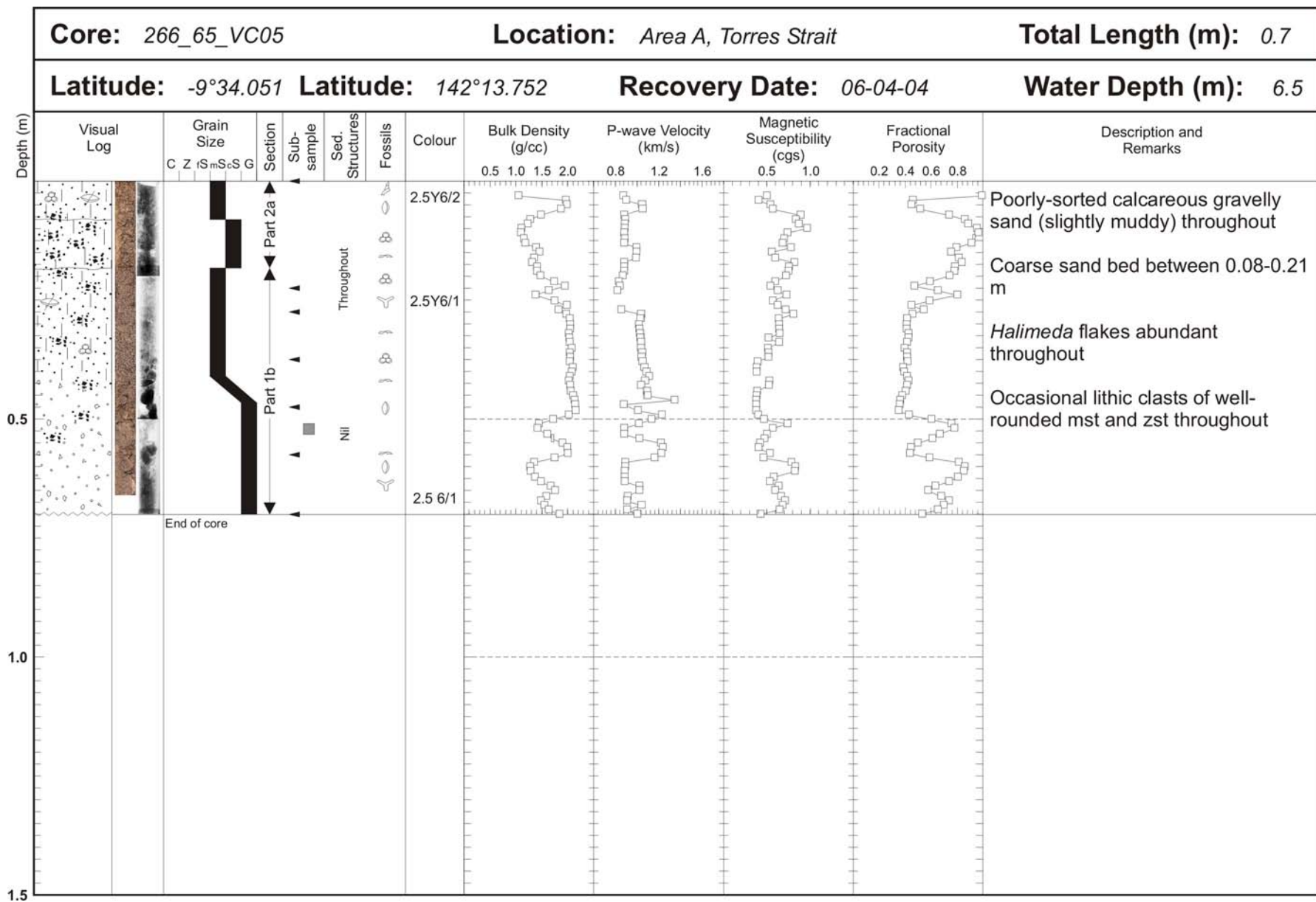














## 8.9. Appendix I – Textural Characteristics of Subsurface Sediments

The tables below show the textural data for the sub-samples collected from the vibrocores. The data are based on sieve analysis and carbonate bomb analysis, and are thus expressed as weight percents. Grain size distributions for all of the subsurface samples expressed as volume percentages measured from the Malvern™ Mastersizer-2000 laser particle analyser can be found on the accompanying data DVD. Grainsize distribution graphs and associated data from the Malvern are contained on the data DVD in jpg format. The filenames follow the convention: 7-digit Lab Number\_GA Survey Number\_Station Number, Operation Type, Operation Number\_Sub-sample Depth Interval (e.g., 1419462\_266\_63VC01\_0-2).

Table 8.3. Textural characteristics of sub-samples collected from the vibrocores.

Core	Depth (m)	%Gravel	%Sand	%Mud	%CaCO <sub>3</sub> (Bulk)	%CaCO <sub>3</sub> (Sand)	%CaCO <sub>3</sub> (Mud)
VC1	0.00-0.02	8.99	73.01	17.99	87.2	93.8	68.9
	1.18-1.20	24.43	59.07	16.50	84.1	89.2	55.7
VC2	0.00-0.02	14.59	83.98	1.43	92.8	95.3	I/S
	0.08-0.10	5.98	92.53	1.48	90.7	93.3	I/S
	0.28-0.30	21.53	75.66	2.81	89.7	94.3	I/S
VC3	0.00-0.02	33.20	65.26	1.54	88.2	93.3	I/S
	0.05-0.07	15.67	82.82	1.51	92.3	92.3	I/S
	0.10-0.12	7.38	90.58	2.04	92.3	93.3	I/S
	0.15-0.17	13.64	83.87	2.49	98.3	94.3	I/S
	0.20-0.22	15.36	81.02	3.63	92.3	93.8	I/S
	0.25-0.27	24.87	72.67	2.46	91.2	93.3	I/S
	0.30-0.32	26.53	71.23	2.24	91.2	94.3	I/S
	0.35-0.37	8.08	90.09	1.83	91.2	93.8	I/S
	0.40-0.42	4.44	93.71	1.86	91.8	93.3	I/S
	0.45-0.47	7.83	90.51	1.65	93.3	94.3	I/S
	0.50-0.52	24.25	73.46	2.28	92.3	95.3	I/S
	0.55-0.57	23.91	72.62	3.47	91.2	93.3	I/S
	0.60-0.62	19.43	73.79	6.78	92.3	95.3	I/S
	0.65-0.67	23.91	62.55	13.54	89.7	95.3	67.9
	0.70-0.72	35.05	56.72	8.23	90.2	95.8	I/S
	0.75-0.77	17.37	75.57	7.06	89.7	96.8	I/S
	0.80-0.82	37.66	59.68	2.66	93.8	95.3	I/S
	0.85-0.87	18.18	76.88	4.94	93.8	96.8	I/S
	0.90-0.92	15.27	80.43	4.30	93.3	97.3	I/S
	0.95-0.97	9.78	86.39	3.82	92.3	97.3	I/S
	1.00-1.02	11.03	85.41	3.56	92.8	96.3	I/S
	1.05-1.07	7.79	84.02	8.18	93.3	96.8	I/S
	1.10-1.12	16.22	79.46	4.32	94.3	97.3	I/S

	1.15-1.17	11.17	82.51	6.32	91.8	98.3	I/S
<hr/>							
VC4	0.00-0.02	20.47	77.29	2.24	93.3	95.8	I/S
	0.15-0.17	66.26	30.92	2.83	95.3	95.8	I/S
	0.28-0.30	21.89	73.59	4.52	92.3	95.3	I/S
	0.48-0.50	43.69	51.16	5.16	92.3	96.8	I/S
<hr/>							
VC5	0.00-0.02	38.42	57.07	4.51	92.3	96.3	I/S
	0.23-0.27	52.96	42.53	4.51	91.2	96.3	I/S
	0.27-0.29	48.05	45.17	6.78	91.2	95.8	I/S
	0.37-0.39	35.90	55.91	8.19	90.7	97.3	I/S
	0.47-0.49	54.20	39.14	6.66	93.8	96.8	I/S
	0.57-0.60	44.44	45.24	10.32	89.7	97.8	I/S
	0.69-0.72	24.46	66.29	9.25	90.2	97.3	I/S
<hr/>							